University of Cape Town

Department of Astronomy

The Very High Energy Gamma Ray Burst GRB190114C as observed by MeerKAT

AST5000W

Author:

Reikantseone Diretse

Dissertation submitted in full fulfilment of the requirements for Master of Science in Astronomy

Supervisors:

Patrick Woudt

(Department of Astronomy, University of Cape Town)

Alexander van der Horst

(Department of Physics, The George Washington University)

2023

Abstract

We present the MeerKAT study of the highly energetic gamma ray burst (GRB), GRB190114C, which was the first GRB to have been recorded at teraelectronvolt (TeV) energies by the MAGIC telescope. We have observed this GRB with MeerKAT from as early as within the first day of the burst event, up to nearly a year at over 350 days. Our 13 epoch light curve is the most sampled radio light curve of this GRB at low frequencies (1.28 GHz) in comparison to published results. We detail the evolution of GRB190114C as a forward shock in a homogeneous medium for about 100 days post-burst, followed by a jet-break likely occurring simultaneously with the passage of the characteristic peak frequency across our observing band. We constrain the host galaxy component, and compare our modelled host value to fluxes extrapolated from pre-burst images of the field. As it is often for GRB observations at low radio frequencies, the evolution of GRB190114C is highly affected by strong interstellar scintillation, which we quantitatively constrain as long lasting refractive scattering. We then use the calculated scintillation parameters to put an upper limit on the radial size of the fireball, and compare this to other GRBs. Beyond the GRB, we take a commensal approach to study its intriguing and expansive background. We survey the field for potential radio transients or variables. We apply the LOFAR Transients Pipeline (TraP) in this pursuit, which has been adapted for MeerKAT data. We discover 11 potential transient or variable candidates. We detail their light curves, images, multi-wavelength counterparts and classifications to reveal their nature. We find that most of the candidates we find are likely active galactic nuclei (AGNs), and their variability in this context is reasonably due to interstellar scintillation as derived for the field.

Acknowledgements

I vividly recall I had just returned from the Australia Telescope Compact Array at Narrabri, when I saw Patrick's ping proposing an MSc project on a newly discovered, very high energy GRB detected at TeV energies. Patrick, thank you for entrusting me with this very enriching project. Thanks for all resources and very inspiring collaborative networks that patiently saw this work to completion. I am thankful for your patience, knowledge, and wisdom. You created a space that allowed me to learn and explore, and this has cemented a very solid foundation for my science journey. There will never be enough words to describe my gratitude for your leadership through all this.

Alexander, thank you for taking me on an epic adventure that is the study of radio afterglows of gamma ray bursts! Thanks for your thorough tutelage on the theoretical frameworks, as well as coupling radio observations with theory. I'm still excitedly bewildered at how much I now know, and how much much more I still don't know. Thanks for creating a space for me to learn, question, understand, get confused, understand, get more confused, and always being there to answer my questions. Thanks for the networks with your PhD students (Deniz at Uni Amsterdam, and Sarah at the GWU), both of whom have had a substantial impact on how I've come to understand my work, be it GRB physics, or the intricacies of transients searches. I am convinced that our mutual appreciation for transients is yet to see us collaborate in future, within and beyond ThunderKAT.

To my parents and my two sisters- Ke lebogela lerato le tshegetso ya lona e e ntetlang go gola ka botlhale. Se ke tshimologo ya leeto le le leele, mme ke lebogela fa ke itse gore le tla tlhola le nsthegeditse, e bile le ntshepile.

Thanks to: Lilia Tremou (NRAO) for the virtual lessons on radio data reductions and imaging, Gemma Anderson (Curtin University) for insightful introductory discussions while I was still in Sydney and providing ATCA data, Ian Heywood (Oxford, Rhodes Uni, SARAO) for impeccable tricks on radio imaging, Antonia Rowlinson (University of Amsterdam) for helping with the TraP pipeline set ups and initial tests, Laura Driessen (ICRAR, CSIRO) for always responding to all my questions about everything and all sundry! Thanks to Deniz Aksulu (Uni Amsterdam) for all the GRB analysis discussions (that paper can finally come out now). Thanks to Lauren Rhodes (Oxford) for all the amazing chats on the physics of GRBs while in Simon's Town. To Alex Andersson (Oxford) for the highly impactful sessions on the analysis of TraP results while you were in Cape Town, and for also being an incredible quiz nights partner! To Sarah Chastain (at The George Washington University)- thanks a ton and ten tons more for all the help with the TraP. To Paul Groot (Radboud Uni, UCT, SAAO)- thanks for saving the day with help on the FORTRAN code for scintillation effects! To Nicky Walker, Jordan, Jeremy and everyone at IDIA. To Saalih, Rushana, Siphelo and everyone at NASSP. To Jacinta Delhaize (UCT) for her mentorship. To Miriam Nyamai (SARAO), Lauren Rhodes (Oxford), Zwido Khangale (UCT)- for reading this work and providing thoroughly constructive feedback. I can only hope to improve over time. To friends and office mates, past and present; Tshia, Melkameshet, Simon, Nathan, Moses, Henco, and Chad. Thanks for the joyous space, research chats, all the coding hacks, and the incredible collegiality. Thanks to Robbie and Tim, for the ice cream and sushi days, and many exciting lessons.

To my friends: Tshiamiso and Mokhine - for the cherished nights of wine and pizza, and enlightening conversations that have directly helped me grow. To Mponeng- for being a dear friend and a partner in all that is good, to Omphile for all the coding hacks, and Mpendulo for all the flair. Thanks to you three for the backyard brunches and dinners. Thanks to Mpolokeng. To Lebogang and Jeanette - for all the virtual calls that have helped me make better life decisions professionally, emotionally, and spiritually. To Zwido and Orapeleng- for always being there to listen and give sound council. To Martin - for thought provoking chats, and having to listen to my solo musicals, very sorry. To everyone via the Astro Socials: (Sumari, Senate, Chad, Krishna, Okkert, Nikki, James, Alex, Nathan, and many others) - Thanks for the amazing times; be it First Thursdays, impromptu Astro chats mid drinks, or the very best quiz and karaoke nights.

Thanks to my therapist- for leading me on a promising journey of healing and rediscovery.

Finally, to my darling Senzo, with whom and through whom I've come to learn a great deal about myself. Thanks for some of the most beautiful memories made throughout this journey.

In loving memory of my dearest, beautiful, spirited, and very young mom, Keamogetse, who unexpectedly passed on two weeks after the submission of this dissertation. Ke tla go lelêla le go go gopola go fitlhêla lerole la naledi ya bofêlo mo popong yotlhe le fêlêla lefeleleng. A kagiso ya Mmopi e go aparêlê, le mowa wa gago o tshelêlê ruri, morwadia Khukhwane Mogawane!!

Plagiarism Declaration

I, Reikantseone Diretse, hereby declare that the work on which this thesis is based is my original work (except where acknowledgements indicate otherwise) and that neither the whole nor any part of it has been, is being, or is to be submitted for another degree in this or any other university. I authorise the University of Cape Town to reproduce for the purpose of research either the whole or any portion of the contents in any manner whatsoever.

Contents

List of Figures

Chapter 1

Introduction

1.1 Radio Transients

The fast paced emergence of a new generation of high sensitivity, high resolution, and powerful telescopes such as the MeerKAT radio telescope has led to radio transients increasingly becoming one of the most extensively studied topics in high energy astrophysics (Jonas & MeerKAT Team, 2016). As radio transients are sources of markedly exaggerated radio emission on timescales as brief as a few milliseconds to as long as a few years, these sources are expected to be associated with some of the most extreme phenomena of bursts, flares, and pulses (Cordes et al., 2004). These transients are exemplified by events such as fast radio bursts (FRBs), gamma ray bursts (GRBs), supernovae explosions, accreting stellar mass black holes, compact binary coalescence events resulting in gravitational waves, and many other temporally variable events observed at radio frequencies (Fender & Bell, 2011; Fender et al., 2015). Radio observations of these explosive and outbursting events are a direct tool for investigating some of the fundamental questions in astrophysics. Some of these fundamentals include aspects such as a better understanding of efficient mechanisms for astrophysical particle acceleration, shocks, electron density in the intervening media, the nuclear equation of state, strong gravitational fields, and even discoveries of new phenomena previously unknown (Cordes et al., 2004). New cutting edge radio telescopes such as MeerKAT and ultimately the Square Kilometer Array will significantly transform our understanding of radio transients and the various environments from which they originate, within our Galaxy and across the universe (Fender et al., 2016).

Radio observations are uniquely suited to study explosive transients at wide fields of view (meaning faster survey speeds), as well as high angular resolution and sensitivity, especially with new powerful imaging telescopes like MeerKAT (Fender et al., 2016). Transient eruptions often involve compression of magnetic fields as sources collapse, and the acceleration of particles (usually relativistic electrons) around these fields, resulting in synchrotron emission. This emission is observed as feedback in terms of relativistic ejecta such as jets, or also observed in isotropic explosions as spherical blast waves that shock particles in the ambient medium to relativistic velocities, and thus also generating synchrotron emission. This emission in the radio frequencies is a direct tool to uniquely estimate the total amount of energy injected in these explosions. Properties of the environments from which these eruptions occur can also be studied.

The radio emission emanating from a transient source interacts with the intervening media, often resulting in scattering and dispersion of the emitted radio waves. These interactions with the intervening medium continuously rotates the waves' polarisation plane as they propagate along our line of sight until we record them. From this polarisation information, we can deduce the properties of the interstellar or intergalactic environments that the waves have interacted with. Naturally, the emission mechanisms or processes for these transients can be inferred from the broadband radio observations. However, there are other radio transient phenomena whose emission mechanisms are still not fully understood from observations, such as pulsars and fast radio bursts. Fast radio burst events may even be more fascinating puzzles to solve as no counterparts (if any) have yet been observed at other regimes of the electromagnetic spectrum. To establish any ideas about these events it is often useful to have ample sample populations from which any

deductions on the intrinsic source properties, emission mechanisms, environments, etc, can be made from any similarities or patterns the samples exhibit.

There is a plethora of transients research that has been done over the decades with significant discoveries that have advanced the field. Some of the initial discoveries of transient radio emission were from within the Solar System, from the Sun and the planets. From planets in particular, Burke & Franklin (1955) reported nine radio detections out of 31 obtained records of radio emission at the location of Jupiter, with their investigation revealing confident radio detections in a form of bursts during low terrestrial interference at night hours. The discovery of pulsars through a meticulous analysis of data records by Jocelyn Bell Burnell at the Mullard Radio Astronomy Observatory described the sources as neutron stars characterised as pulsating sources of unusual radio signals from within the Milky Way galaxy (Hewish et al., 1968). Today, pulsars are arguably one of the most extensively researched radio sources since they are continuously radiating in the radio frequencies as they are highly magnetized fast rotating neutron stars. They are often regarded as lighthouses due to their beamed emission that is only detected when they point in the observer's line of sight. Other previous discoveries of transient radio emission include the observation of superluminal apparent velocities of relativistic jets in extragalactic sources. The observation of two quasars by Cohen et al. (1971) showed that both sources had expansion rates at velocities apparently greater than the speed of light. Similarly, but within the Milky Way, Mirabel & Rodríguez (1994) observed relativistic jets moving at superluminal velocities from a high energy central engine of a stellar mass scale. These superluminal jets were understood to originate from an accreting stellar mass black hole in a binary system, and these systems have now come to be called microquasars since their dynamics are similar to, but are smaller scale compared to quasars observed at cosmic redshifts, e.g GRS 1915+105 (Mirabel & Rodríguez, 1994).

Efforts to study the transient sky at other wavelengths from high energy γ-rays and X-rays, all the way to the radio frequencies, have also been useful in constraining the physical properties of some transients. An example of this is the X-ray discovery of one of the first stellar mass black hole candidates, Cygnus X-1 (Hjellming & Wade, 1971a), as well as the detection and monitoring of its variable point source counterpart at radio frequencies (Hjellming & Wade, 1971a,b; Wade & Hjellming, 1972; Hjellming et al., 1975), and its ultimate confirmation as a black hole (Stark & Connors, 1977). Dedicated transient searches have for a long time been synonymous with X-ray observations.

Similar to stellar mass black hole candidates in the X-rays, gamma ray bursts were also first discovered in the high energy γ-ray bands (Klebesadel et al., 1973), and later at radio frequencies (Frail et al., 1997), resulting in the now well resourced multi-wavelength exploration of the physics of these systems. The discovery of fast radio bursts from archival data sets has also contributed to radio transients studies (Lorimer et al., 2007). The implicit form of synergy brought by the now very relevant real-time multi-wavelength transient studies, as well as searching archival data sets for transients, is pushing boundaries and changing how research has been done over the ages. From a radio perspective, improvements are currently underway to upgrade previous telescopes to optimize their sensitivity and computational power. In the Southern Hemisphere, the dynamic radio sky is also being sampled through survey strategies, e.g through MeerKAT and the Australia Square Kilometer Array Pathfinder (ASKAP) (Johnston et al., 2007).

It is generally accepted that radio transients tend to conform to a dichotomous classification as coherent or incoherent events, with incoherent synchrotron events constituting the significant majority of current samples of transients across the electromagnetic spectrum. The coherent transients are intrinsically of very short timescales, typically a few milliseconds, and are thus usually observed by pulsar mode strategies. They are so short lived as they reach especially high brightness temperatures of up to about $T_B \sim 10^{30}$ K at the maximum (Fender et al., 2016). Incoherent transients are synchrotron events commonly synonymous with explosive kinetic feedback from relativistic jets, supernovae, etc, and are conversely much longer lasting with slow variabilities observable by interferometric imaging from hours, days and up to years. The incoherent events are the most luminous due to their steady emission at a typical brightness temperature of up to $T_B \sim 10^{12}$ K (Fender et al., 2016). Both classes of transients, coherent and incoherent, are extremely

energetic in that they are observable even at cosmological distances. This property thus makes transients invaluable tools to probe the various interstellar and intergalactic environments they originate from.

1.1.1 Coherent Radio Transients

The most common examples of coherent radio transients are pulsars and fast radio bursts. Pulsars are usually detected to have brightness temperatures around $T_B \sim 10^{20}$ K. They are the most recognised coherent events due to dedicated studies of a broad sample of pulsars within the Milky Way and nearby galaxies such as the Magellanic Clouds. The exact emission mechanisms for coherent events like pulsars or FRBs are not yet concretely established, with ongoing broadband research in the field still making efforts towards constraining the neutron star equation of state (Watts et al., 2016, and references therein). The latest addition to coherent radio transients was FRBs. The first FRB was discovered from the analysis of archival pulsars survey data by Lorimer et al. (2007) from the Parkes telescope. The FRB proved to be a singular novel burst of extragalactic origin, with a characteristic high dispersion measure that could not be attributed to any other high energy events in the source direction. Since this discovery, the nature of FRBs still remains mostly unknown, with at least a dozen models posited to explain the phenomena. The proposed model classes are based on various radiation production mechanisms and range from compact binary interactions, collapse of compact objects, supernovae remnants, giant singular or clustered flares from magnetars and many others with each model class having sub-classes pertaining to specific FRB events, e.g doubly degenerate white dwarf mergers from the binary interaction models, see Platts et al. (2019) for full review. Substantial progress at ASKAP and the Canadian Hydrogen Intensity Mapping Experiment (CHIME) has been made, with repeater FRBs being discovered (CHIME/FRB Collaboration et al., 2019) as well as localising host galaxies (Bannister et al., 2019; Marcote et al., 2020). From these recent findings, we now understand that repeating FRBs may originate from different regions of their diverse nearby and far host galaxies, and may as well have very different characteristics or properties due to this.

1.1.2 Incoherent Radio transients

Incoherent transients dominate the current samples of transients across the electromagnetic spectrum primarily because all explosive phenomena are usually associated with synchrotron emission. This is typically from ejecta moving at velocities greater than the local speed of sound, compression of magnetic fields and the associated particle acceleration. The events may also be the most luminous electromagnetically, such as gamma ray bursts, supernovae and even active galactic nuclei (AGNs) with their supermassive black holes and relativistic jets. The evolution of these more luminous events is expected to be slow due to effects of self absorption caused by their intervening media, and also because steady state incoherent emission is limited to a brightness temperature of $T_B \sim 10^{12}$ K. However, the events can also be of relatively low luminosity, such as in stellar flares. As these events dominate transient samples across the electromagnetic spectrum, they are also usually visible in greater detail at other wavelengths such as the X-ray, optical, and gamma rays. Complementary multi-wavelength studies are usually essential as various aspects can be investigated fully. For example, accretion is commonly visible in the X-rays and optical bands, while the relativistic ejecta due to accretion is visible in the radio frequencies, with complementary observations thus providing useful insight on the amount of mass lost due to accretion, and how much of that mass is converted into the energy that powers the jet (Fender et al., 2015, 2016).

1.2 MeerKAT Transients through ThunderKAT and MIGHTEE

1.2.1 ThunderKAT

ThunderKAT is the transients imaging large survey project for MeerKAT. ThunderKAT stands for "The HUNt for Dynamic and Explosive Radio transients with meerKAT" (Fender et al., 2016). The project aims to search for and identify radio transients through their synchrotron emission in the radio bands.

The project started taking observations as early as mid-2018 when MeerKAT was inaugurated and started operations. ThunderKAT has allocated time with MeerKAT, and can also search for new transients in the data of other MeerKAT Large Survey Projects (LSPs). The team has scheduled weekly monitoring observations of known accreting binary systems among many other sources, and also performs quick follow up observations of newly discovered sources of interest. The project surveys and monitors local (within the Milky Way galaxy) radio transients and explores any distinct populations in the galactic neighbourhood. Extragalactic sources of interest for the ThunderKAT team are Type Ia supernovae and short gamma ray bursts that erupt from mergers of compact binaries. In order to become the most expansive radio transients imaging survey project to date, commensal data exploration is also pursued, where ThunderKAT affiliates perform transient searches from approved object specific ThunderKAT observations, as well as observations of other MeerKAT LSPs without changing those projects' original data sets or influencing their observing strategies. MeerKAT's sensitivity to image a broad range of targets with high resolution, even for diverse science cases, is exploited through commensal transient searches in all available or approved data products.

Accretion is arguably the most common astrophysical process in the Universe across various scales and environments, given that it is the basis for the formation of stars, planets around stars, galaxy formation, and feeds AGNs. Specific to relativistic accretion in transient terms, these events are usually tied to the ejection of outflows, and ThunderKAT studies these in detail. Stellar mass black holes and neutron stars in X-ray binaries (XRBs) are the focus of the project to investigate how accretion states influence the power and kinetic outflows from these compact objects via winds and jets. From these studies, features that are unique to the type of compact object at hand, e.g X-ray binary characteristics specific to and/or exclusive to a black hole system due to the existence of an event horizon, can be definitively constrained. Previous studies with quasi-simultaneous radio and X-ray observations have realised strong connection between accretion and outflow in X-ray binary systems (Gallo et al., 2006), with a well defined non-linear power-law correlation curve. By extending to add a mass term for all possible black hole masses (Körding et al., 2006), this correlation can also be explored for accreting supermassive black holes in active galactic nuclei (AGNs). By sampling various stellar mass black hole candidates within the Milky Way with ATCA and *Swift* data, Corbel et al. (2013) populated this "universal" curve, showing a strong relation between accretion rate and jet power. To further understand these systems in quiescence, ThunderKAT intends to populate this curve with MeerKAT observations in concert with space observatories such as *Swift*, and will increase the measurements five-fold, and especially providing a mapping for the neutron star XRBs which are notably radio-quiet in comparison to the black hole systems. Initial efforts on this have been reported with observations of GX339-4 in quiescence to probe the lower-end of the correlation plane (see Figure 1.1; GX339-4 upper limits are shown by green arrows), revealing accretion properties and jet generation when the black hole candidate was in a state of low-accretion rates (Tremou et al., 2020). The study provided upper limits for the radio luminosities in the quiescent state for GX339-4.

Apart from populating the fundamental plane of binary black hole systems with MeerKAT, more research on these systems is pursued. ThunderKAT has investigated disc-jet coupling from MAXI J1535–571 while it was in an outburst between 2017 and 2018 (Russell et al., 2019). The study constrained the quenching of the jet, as well as revealed an apparently superluminal jet-knot when the system was transitioning between accretion states. This contributed to furthering our understanding of physical parameters at play, particularly the evolution of accretion states that X-ray binary systems undergo, namely from hard to soft transitions (see Fender & Belloni, 2012, for a summary on accretion state transitions). Another ThunderKAT study by Bright et al. (2020) resolved superluminal ejecta from another black hole candidate MAXI J1820+070 using MeerKAT data in concert with AMI-LA, VLA, VLBA, and eMERLIN observations. The radio flaring from the binary system as it transitioned from the hard state to the soft state was associated with the jet propagating from the stellar mass black hole, with observations from 100 to 150 days indicating well resolved ejecta that was strongly suggestive of superluminal velocities (Bright et al., 2020).

ThunderKAT also examines the relation between accretion and outflows from accreting non-magnetic white dwarfs in close binaries which constitute a collection of binary systems called Cataclysmic Variables (CVs).

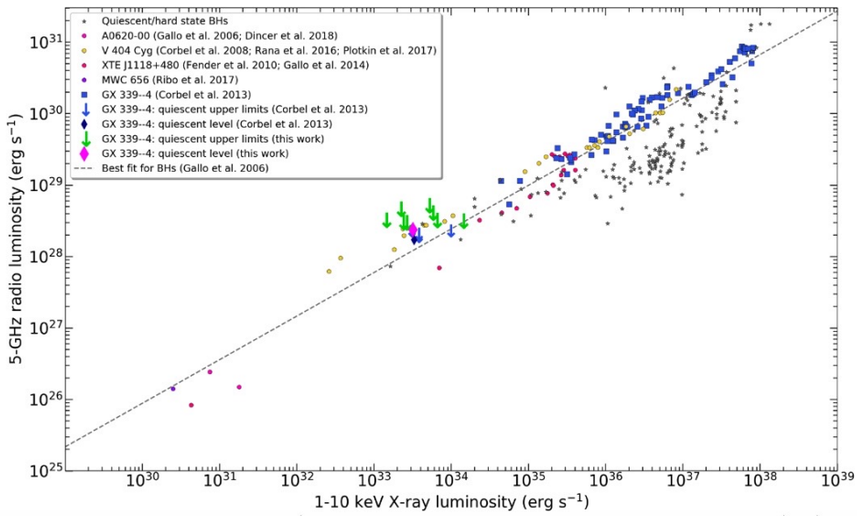

Figure 1.1: The MeerKAT updated "universal" correlation with observations of GX339-4 (green arrows). The lower end of the curve is yet to be filled with additional observations, and this is also in progress for other black hole candidates in the Galaxy. Adapted from (Tremou et al., 2020)

The outbursts in these systems are triggered by disc instabilities just like with X-ray binaries, and they are often associated with dwarf novae (DNe) outbursts. DNe are typically non-magnetic with accretion onto the white dwarf surface via an accretion disc. Since previous CV detections in the radio frequencies were not reproducible due to low telescope sensitivities and thus limited confirmation, these systems have not been well studied in the radio. Notably, Coppejans et al. (2015) yielded a 75% detection rate for four sampled novalike CVs with the JVLA for the first time. This provided compelling evidence that these non-magnetic cataclysmic variable systems produce radio emission. ThunderKAT has already begun observations of these systems in concert with the MeerLICHT telescope. Examples include Khangale et al. (2020), who revealed the UZ For eclipsing polar as a faint radio source with MeerKAT (see Figure 1.2a) in complement to optical observations, as well as Hewitt et al. (2020) who surveyed 11 nearby novalike CVs with MeerKAT, detecting only 4, and reporting a very first radio detection of IM Eri (see Figure 1.2b).

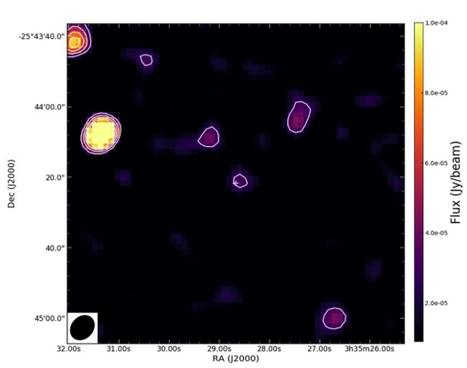

(a) UZ For revealed as a faint radio source. (See small cross at centre of image)

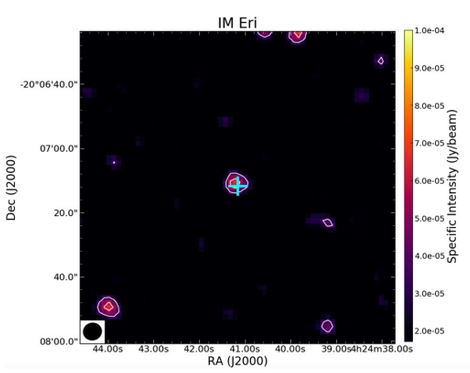

(b) IM Eri first reported radio detection. (See cross at centre of image)

Figure 1.2: MeerKAT detections of two cataclysmic variable systems. See Khangale et al. (2020) for UZ For, and Hewitt et al. (2020) for IM Eri and other MeerKAT surveyed CVs. Figures adapted from Hewitt et al. (2020) and Khangale et al. (2020).

Cosmic explosions, specifically short GRBs resulting from collisions of compact binaries comprising two neutron stars or a neutron star and a black hole, are synonymous with liberating huge amounts of energy (stellar mass rest energies) as gravitational waves (GWs). These waves were predicted by Einstein's theory of general relativity one hundred years ago, and were first observed by the Laser Interferometer Gravitational-Wave Observatory (LIGO) (Abbott et al., 2016). In concert with the GWs, trace amounts

of electromagnetic radiation is expected, particularly in scenarios involving neutron stars and this has been exemplified by GW170817 (Abbott et al., 2017b). ThunderKAT hopes to explore this emission using MeerKAT and the MeerLICHT optical telescope. Other cosmic explosions to be studied by MeerKAT and MeerLICHT are type Ia supernovae, for which identification of progenitor characteristics is still an ongoing problem, amongst many others. Long GRBs are not included in ThunderKAT. However, special case observations of long GRBs with high scientific significance are possible through Director's Discretionary Time (DDT) and Open Time proposals. In fact, the observations presented by this thesis were obtained from such a process.

The first MeerKAT transient, MKT J170456.2–482100, was first discovered from ThunderKAT images of the field containing the canonical black hole candidate GX339-4 (Driessen et al., 2020). Since GX339-4 has been observed weekly since MeerKAT was inaugurated in 2018, the rich data set collected for the field provided an excellent opportunity to search for transients. By using a LOFAR developed transients search pipeline called TraP, Driessen et al. (2020) detected MKT J170456.2–482100 from 33 ThunderKAT observations between April 2018 to June 2019, with about 14 non-detections within that time interval (see Figure 1.3). A total of 48 epochs were available, where the first 2 epochs were during MeerKAT's commissioning phases, and the remaining 46 were weekly, as per the ThunderKAT allotted time. After identification as a radio transient, MKT J170456.2–482100 was confirmed as associated with an optical counterpart TYC 8332-2529-1, a sub-giant star with archival survey data at various wavelengths for at least 18 years. Subsequent photometry of the transient pinned the period of the star to be 21.25 days, with the radio emission posited to originate from probable star spots of the K-type star (Driessen et al., 2020).

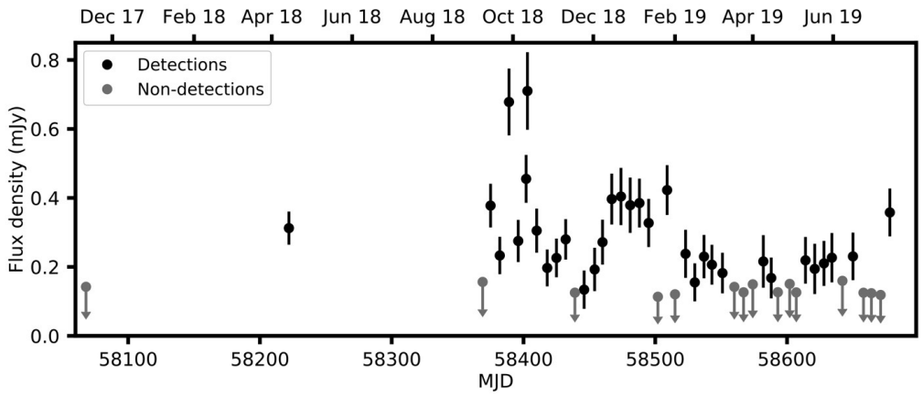

Figure 1.3: The light curve (flux vs date/time) of the first ThunderKAT discovered transient using MeerKAT. The transient showed flux variability up to a maximum of 0.8 mJy, with 15 non-detection limits below 0.2 mJy. The transient is associated with probable star spots from a sub-giant star TYC 8332-2529-1, with a period of about 3 weeks (Driessen et al., 2020).

1.2.2 Commensal ThunderKAT-MIGHTEE

As of 2022, ThunderKAT project has published numerous MeerKAT results across various above mentioned topics, as well as contributing to high impact publications (e.g MAGIC Collaboration et al. 2019b). The discovery of a first MeerKAT transient, MKT J170456.2–482100, from the GX339-4 field by Driessen et al. (2020) has also motivated team members to perform in situ transient searches in all ThunderKAT observed fields. This means all fields that were primarily a focus due to specific transients such as GX339-4, GRB190114C etc, will in extension be searched for other possible transients as well. This is expected to grow as MeerKAT has now started observations for all other LSPs. In particular, one of the MeerKAT LSPs that ThunderKAT will be exploring commensal data use with to search for transients is the MIGHTEE project. MIGHTEE is a "MeerKAT International GHz Tiered Extragalactic Exploration" survey project that has its own mandate to survey the most well documented extragalactic deep fields (Jarvis et al., 2016). From the Southern Hemisphere, MIGHTEE will provide a 20 deg^2 exploration of four extragalactic fields

at a sensitivity of $\sim 1\mu$Jy and resolution of ~ 6 arcsec over 900-1670 MHz frequency range. MIGHTEE will achieve a detailed sample of galaxies out to about $z \sim 0.5$ at the high mass end of the neutral hydrogen (HI) mass function (HIMF), which is an important extragalactic probe for galaxy formation and evolution, as well as other cosmological implications. In addition to neutral hydrogen and the evolution of cosmic magnetic fields in clusters, MIGHTEE will improve the research on star formation history across galaxies in the local universe. The project complements other MeerKAT LSPs with similar research interests. Relevant to ThunderKAT, this project will have a wealth of data for many galaxies and thus giving ThunderKAT an opportunity to make interesting discoveries of any radio transients associated with those galaxies. Considering that MIGHTEE pointings are quite long at several hours per pointing, their data sets may provide opportunities for intra-epoch surveys for short time variables or transients. As an example of commensal data usage, and directly relevant to this work, initial MIGHTEE pointings during the mid-late 2018 include the field within which the host galaxy of the first GRB observed at teraelectronvolt energies, GRB190114C, is located. Probing this MIGHTEE data for the location of this GRB host can help with constraining the initial flux of that host galaxy prior to the energetic eruption of the GRB, and thus giving a clearer indication on the true flux of the GRB.

1.2.3 The IDIA Computational Infrastructure

IDIA is the Inter-University Institute for Data Intensive Astronomy. It is a cloud based computing infrastructure developed by collaboration between universities for data intensive research in astronomy, and is also dubbed Ilifu (isiXhosa and isiZulu for "cloud"), and users login to the remote computer through a secure shell. The cluster has dedicated storage (main /scratch is 300TB) and processing capacity for a number of the MeerKAT large survey and open time projects, including ThunderKAT.

Observations for ThunderKAT started mid-2018 after the official MeerKAT inauguration and the IDIA system has been in operation ever since. The ThunderKAT project is allocated a directory for data storage and its registered affiliates are permitted access to the raw telescope data, copy to their own user directories and run reduction pipelines interactively or by sending jobs to the cluster's slurm head node. Slurm is a free open-access job scheduler for computer clusters. The cluster system is equipped with the majority of mainstream astronomy research software packages in the form of singularity containers which the users can interact with for running their pipelines, or through sending scripted jobs.

1.3 MeerKAT and Radio Interferometry

1.3.1 MeerKAT

Here we finally describe the instrument used, since we have described in detail the relevant radio transient topics covered by ThunderKAT. The MeerKAT radio telescope is an interferometer located outside the small town of Carnarvon in the Northern Cape, South Africa. The telescope consists of 64 antennas of 13.5 m diameter each (Jonas & MeerKAT Team, 2016; Camilo et al., 2018). The array is spread out over a longest baseline of about 8 km, and centered at latitude of $32^\circ 42'$S and $21^\circ 23'$E in longitude. The core of the array consists of 48 antennas with a minimum baseline of 29 m, while the remainder 16 antennas are spread out to the full baseline. The antennas are parabolic with a Gregorian offset subreflector that is also affixed near the receivers, in a configuration rendering a completely usable antenna aperture (see Figure 1.4). This design is also optimised to minimise and deflect ground radiation, resulting in a low system temperature of $T_{sys} \sim 20$ K. MeerKAT has UHF and L-band receivers in a system covering these overlapping bands in a span of 580 MHz to 1670 MHz. The UHF ranges from 580 MHz to 1015 MHz, while the L-band ranges from 900 MHz to 1670 MHz. The default observation settings are usually in the L-band, at a central frequency of 1284 MHz, with full polarisation and a binning time of 8 seconds on the target for the duration of an observation. The binning time can also be 4 seconds or 2 seconds, at a cost of storage requirements. MeerKAT is a wide-field imaging facility with a field of view of approximately 1 deg^2 (Jonas & MeerKAT Team, 2016; Mauch et al., 2020) at 1.4 GHz. The telescope has high aperture efficiency such that the full 13.5 m antenna surface from all 64 dishes is utilised for signal reception, and this coupled with the ground radiation deflection renders a very sensitive telescope. These factors thus

make MeerKAT a very useful instrument for transients research amongst many other science cases. Future expansion for the telescope is planned, with S-band receivers and and additional antennas to be added. The telescope is operated by the South African Radio Astronomical Observatory (SARAO) through the National Research Foundation (NRF).

Figure 1.4: The MeerKAT radio telescope during inauguration in July 2018. Only part of the array is shown in the image, with the Gregorian offset configuration design of the antennas in display. Image sourced from: SARAO MeerKAT Array.

The imaging capabilities of the telescope were demonstrated by imaging the Galactic Centre (see Figure 1.5) when the telescope opened in 2018 for research. The image resolved a number of previously unseen features from the galactic centre, such as supernovae remnants, as well as filamentary structures. Imaging has further been explored by Heywood et al. (2019) who revealed previously unrecorded bubbles around the Milky Way's Galactic Centre located in a bipolar structure, and possibly originating from a highly energetic event around the supermassive black hole's environment. Their result included well resolved filamentary structures in a great level of clarity. Another demonstration of image capabilities was by Mauch et al. (2020) who imaged the DEEP2[1] field to show the good wide-field imaging abilities as well as the dynamic range of the telescope in imaging galaxies.

MeerKAT is South Africa's precursor to the Square Kilometre Array (SKA), a global astronomical effort to build the World's biggest radio interferometer. After full completion of the relevant initial phases of additional antennas and receivers to the array, MeerKAT will constitute the mid-frequency component of the SKA, i.e SKA 1-mid array. The telescope currently runs LSP observations (see Jonas & MeerKAT Team (2016) for full LSPs projects list), as well as accepted Open Time proposals from local scientists and internationally.

1.3.2 Interferometry Summary

MeerKAT, like other radio telescopes, operates under a series of complex mechanical and theoretical formulations that constitutes what is called radio interferometry. This is an advanced technique where instead of just one antenna, an array of spatially-distributed antenna elements functions as a single larger and discretely sampled antenna. This means the "diameter" of the array is compatible to the longest baseline of the array, providing ample resolution since the array can be as wide as plausible, and angular resolution of sources is directly dependent on array size. The array elements each collect radio waves from observed sources, which are then converted into voltages by the receivers. Typically, a correlator will

[1] Deep Extragalactic Evolutionary Probe 2

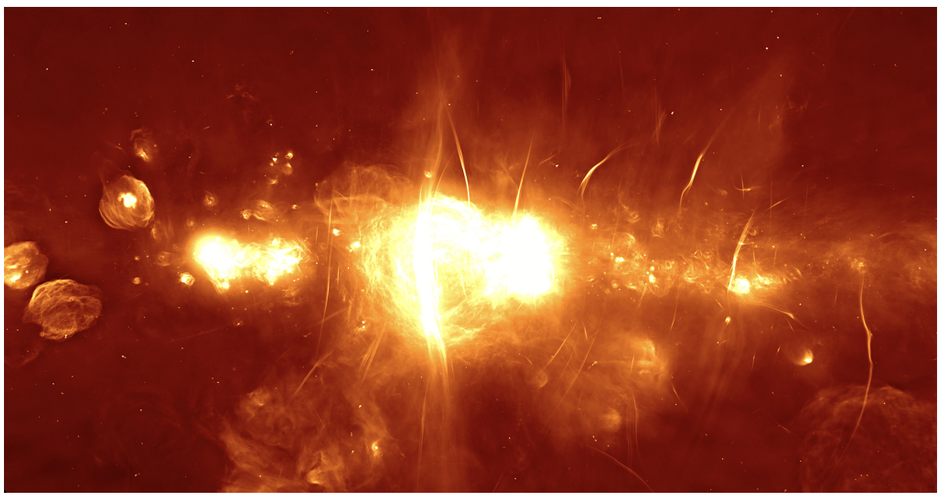

Figure 1.5: MeerKAT's first image of the Galactic Centre. The high resolution of the telescope is demonstrated by the high level of clarity in the resolved features of the Galactic Centre. Filaments can be seen, as well as remnant structures towards the left, and the bright Sagittarius A* region at the center. Adapted from: SARAO-media.

digitize these voltages into quasi-simultaneous phase and amplitude signals that are characteristic of the observed radio sources. Once these signals are recorded and stored for analysis, the relevant calibrations and imaging for scientific reporting follows.

Calibrations play a critical role in the analysis of data in radio interferometry. It is this process that ensures accuracy of all measurements made, as well as the efficiency of the radio telescope in making these measurements. Thorough calibrations provide an excellent opportunity to exploit the full advantage of a telescope such as MeerKAT. Principally, calibrations are done in a series of steps, with ultimate goal being to get true visibilities from the observed target, e.g accurate target position, flux density, polarisation, etc. As such, all possible constraints are taken into account; i.e. from known telescope limitations such as system temperature, receiver performance, pointing errors, atmospheric conditions like water vapour, and effects of the ionosphere etc. All these are usually solved through a series of software-based Fourier transform and deconvolution techniques. Chapter 2 will elaborate on the calibration and imaging processes taken for the MeerKAT observations reported by this thesis. Here I provide a brief perusal on the operations of a typical interferometer using online notes compiled by Oozeer, Bietenholz, and Goedhart[2] , as well as MeerKAT specific tools.

The visibilities (V(u,v)) measured by an interferometer such as MeerKAT are a two dimensional Fourier transform of the sky brightness (I(l,m)), and this may be represented by:

$$V(u,v) = \iint I(l,m) e^{-2\pi i(ul+vm)} dl dm \tag{1.1}$$

where (u,v) are the coordinates in Fourier domain for a small enough field of view sufficient to assume a plane in flat space, and (l,m) are the orthogonal sky coordinates, usually Right Ascension and Declination. An interferometer has a number of baselines dependent on the number of antennas on the telescope, i.e $N(N-1)/2 = 2016$ baselines for a full $N = 64$ antennae observation with MeerKAT. As the interferometer slowly rotates with the earth, the baselines in the array will each sweep out elliptical paths in the (u,v) plane throughout a given observation (see Figure 1.6). For an array such as MeerKAT with that many antennas and hence baselines, this enables excellent sampling coverage of the (u,v) plane, which then translates into better visibility measurements.

[2] github.com/ska-sa/casa_cookbook

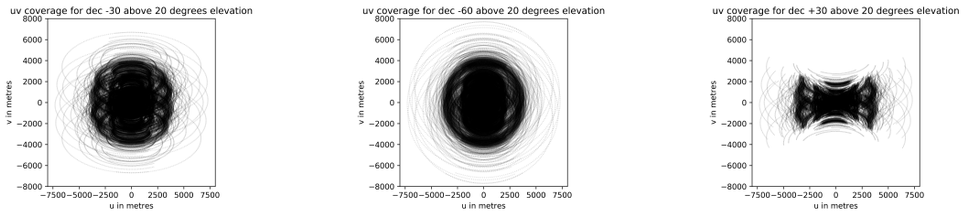

Figure 1.6: MeerKAT full track (u,v) coverage at various declinations above the telescope's 20 degree horizon limit. Images sourced from (SARAO MeerKAT Specifications).

The observed visibilities measured by any arbitrary baseline pairs of the array are not equal to the true visibilities (i.e $V_{obs} \neq V_{true}$) of the sources. They are rather a convolution of the true visibilities with the telescope's behaviour (electronic performance) in making these measurements. This system response is typically called the dirty beam or point spread function (PSF), often manifesting as unwanted side lobes around point sources. Every baseline pair in the array samples in the time and frequency domain over the observation time and bandwidth of the telescope, and the observed visibilities are obtained through some sampling function $S(u, v)$, that tracks the plane. This sampling is not uniform, thus requiring some gridding method where a Fast Fourier Transformation (FFT) is utilised to efficiently construct an image, further degridding results in well sampled visibilities matching the observed sources. The result from these extensive steps is a dirty image, which may be given by:

$$I_{dirty}(l, m) = \iint S(u, v) V_{obs}(u, v) e^{-2\pi i(ul+vm)} du dv \tag{1.2}$$

where $S(u, v)$ is the visibility sampling function, generalised to contain (u, v) coverage, a gridding factor, sky position, frequency coverage and some weighting schemes. In essence this is the point spread function as previously defined, essentially rendering the dirty image as a Fourier Transformation of the PSF with the true/ideal image as:

$$I_{dirty} = PSF \circ I_{true} \tag{1.3}$$

This directly shows that to get a best estimate of the true image, a deconvolution of the PSF is required, usually performed through "CLEAN" tasks. Beyond these steps, other effects corrupting the true visibilities, such as radio frequency interference (RFI), variable pointing errors, electronic malfunctions, noise etc, are mitigated through software based solutions, see Chapter 2.

1.4 Gamma Ray Bursts

Gamma ray bursts (GRBs) are the most luminous cosmic explosions to date in the Universe. These incredibly cataclysmic events are observed in distant galaxies and their bursts are signalled by a flare of highest energy photons in the electromagnetic spectrum, the γ-rays (Klebesadel et al., 1973; Seward & Charles, 2010; Longair, 2011). The enigmatic phenomena of these bursts were discovered in the late 1960s when the Vela satellites launched to monitor for any nuclear weapons testing detected 16 bursts of gamma rays of extrasolar origin. In their analysis, Klebesadel et al. (1973) showed that over the three year operating period, four of the Vela satellites detected bursts of photons in the $0.2 - 1.5$ MeV range with durations of less than 0.1 seconds and up to 30 seconds. The discovery was, however, short of any conclusive evidence on any supernova coincidence with the observed gamma ray bursts as supernovae were a predicted source of such high energy emissions (Colgate, 1968), but that was a feat reserved for almost three decades later.

With more satellites launched (e.g BATSE and others prior), continued observations yielded more results, various theoretical models were posited, interestingly resulting in more models than there were recorded bursts. The challenge at the time was to accurately localise a GRB in order to initiate a multi-wavelength campaign to detect any transient or variable source in the error box of the GRB. The orbiting observatories of the time were limited to this. The field took a major leap forward when the Italian-Dutch satellite, BeppoSAX, accurately localised a burst from GRB970228. An optical counterpart was quickly reported by van Paradijs et al. (1997) after eliminating all possible local objects as sources of the emission, and concluded that the source was a fading optical transient associated with a faint galaxy. Similarly, a soft X-ray afterglow was reported by Costa et al. (1997) within the same location. Further ground-based follow-up with the Westerbok Synthesis Radio Telescope (WSRT) at the time did not report any radio detection from the location of the transient (van Paradijs et al., 1997).

The eruption of GRB970508 in less than three months after GRB970228 provided ample multi-wavelength data. Following an X-ray trigger, Djorgovski et al. (1997) detected an optical counterpart at the location of the transient within five hours postburst, with its flux decaying as a single power-law. Consequent spectroscopy of the optical transient led to the redshift of GRB970508 being constrained to $z \geq 0.835$ (Metzger et al., 1997), confirming them as cosmological. The compelling evidence of these results solved the then very popular distance debate of the origin of GRBs. GRB970508 was also the first radio-detected GRB (Frail et al., 1997). The detection of GRBs at these cosmological distances directly required that the events should be tremendously energetic, in that there should exist a mechanism capable of producing such enormous quantities of radiated energy comparable to solar rest mass energy.

There are two known classes of GRBs; distinguished according to their burst durations as long (≥ 2 s) and short (≤ 2 s) GRBs respectively. These classes were first identified by Kouveliotou et al. (1993) from studying the duration distributions of catalogued GRBs and consequently probing their temporal and spectral properties to reveal this bimodal nature. Long GRBs originate from explosions of massive (≥ 15 $M_\odot$) stars when their cores collapse under their own gravity to form a compact object (a neutron star or black hole) (Woosley, 1993). Long duration GRBs, particularly those observed at relatively low redshifts, have been associated with core collapse supernovae (Type Ib/c) by spectroscopy (Stanek et al., 2003; Hjorth et al., 2003; Woosley & Bloom, 2006), making Wolf-Rayet stars the most suspected progenitor candidate (Granot & van der Horst, 2014; Zhang, 2018). Short duration GRBs in contrast, erupt when compact objects merge. Typically binary neutron stars, or a binary of a neutron star and a black hole coalescing, with both types of merger events resulting in the formation of a more massive compact object (usually a black hole). Short GRBs are often associated with gravitational wave phenomena (Eichler et al., 1989; Kouveliotou et al., 1993; Abbott et al., 2017a), as well as long lasting jets from their afterglow observations (Mooley et al., 2018).

Short GRBs are detected in both star forming and old massive elliptical type galaxies (Berger et al., 2005; Fox et al., 2005), whereas long duration GRBs are almost exclusively found in actively star forming regions

of their host galaxies (Djorgovski et al., 1998; Woosley & Bloom, 2006). The latter are often dwarf and spiral galaxies whose luminosities are typically just a fraction of their total stellar luminosity (Longair, 2011). These dusty galaxies possess sufficient gas and dust to mould incredibly massive stars that live very briefly and eject such huge energies when they explode (Piran, 2005). Detecting these galaxies has been useful to understanding the morphology of the environments from which long GRBs emerge, and in turn exposing possible progenitor characteristics. Atypical outlier hosts exist as well, e.g GRB050219A was shown to have originated from a host galaxy with remarkably low star formation rate to stellar mass ratio compared to all long GRB hosts previously detected (Rossi et al., 2014). The evidence of occasional episodes of massive star formation rates from the observed host led the study to realising that outlier (Rossi et al., 2014).

1.4.1 GRB Physics: A Focus on Long GRBs

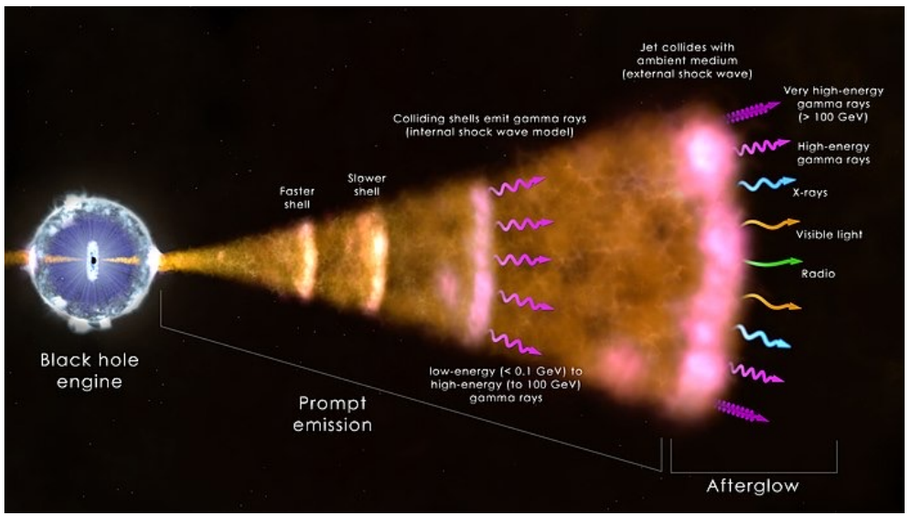

Figure 1.7: Artist impression of a long GRB showing the newly formed central engine from the star's gravitational collapse. The prompt emission as internal shells collide, as well as the multi-wavelength afterglow as the ambient medium is shocked are also indicated. Public domain image from: NASA Goddard Space Flight Center/ICRAR.

Long GRBs have been connected to some classes of supernovae. For a somewhat common supernova of a star that is at least 8 $M_{\odot}$, the star ejects its outer stellar envelope and collapses to form a compact object, usually a neutron star. These supernovae emit neutrinos, and only brighten enough for detection in the optical wavelengths about weeks after the collapse. Their energies are not sufficient to power significant release of gamma rays as observed in long GRBs and this effectively rules them out in favour of more massive stars (Mészáros, 2003). However, for a massive star (between $10 - 15$ $M_{\odot}$ or even above), when its core collapses into a black hole, the black hole instantly experiences a rapid episode of accretion (Woosley, 1993). Due to number of factors, namely; angular momentum conservation, dramatic accretion rates between $0.1 - 1$ $M_{\odot}$ in a matter of seconds, and excessively turbulent magnetic fields, a relativistic jet ruptures through the star's envelope, resulting in radiative shocks in the stellar environment (see Figure 1.7). This jet ploughs through the star and energises the ambient medium, causing the forward and reverse shocks that are then later associated with the afterglow (see Blandford & Ostriker (1978) for stellar particle acceleration review). The timescales of the core collapse and the jet emergence are immensely transient, about a few seconds. Most of the information about the central engine activity is indirectly inferred from afterglow light curves. So the resultant supernova (often type Ib/c), powered by the shocks, emerges from the amalgamation of these initial collapse events (Zhang, 2018).

Examples of supernova connection are in Galama et al. (1998) where a spectroscopically unusual supernova (SN1998bw) in the error box of GRB980425 was detected with supporting radio detections by Kulkarni et al. (1998) also indicating connection. A detection of a supernovae signal from closest proximity with

GRB011121 was reported by Bloom et al. (2002), where the GRB was found to have occurred almost simultaneously with a Type Ic supernova in the region, even though no supporting evidence from other studies was found. From further spectroscopy, several other long GRBs have been associated with Type Ib or Ic supernovae as progenitors, (see Woosley & Bloom 2006, and references therein). These are SNe free of hydrogen (Type Ib) or free of both hydrogen and helium (Type Ic) respectively in their spectral lines (Seward & Charles, 2010; Longair, 2011). Additionally, Smith (2014) provides an extensive review on massive stellar evolution. Of all these supernovae connections, perhaps the most classic one is the spatial and temporal association of GRB030329A with a bright hypernova, SN 2003dh presented by Hjorth et al. (2003). This association was followed by direct spectroscopic confirmation by Stanek et al. (2003) just over a week after the supernova occured, ultimately confirming that long GRBs indeed originate from supernovae.

1.4.2 GRB Physics: The Fireball model

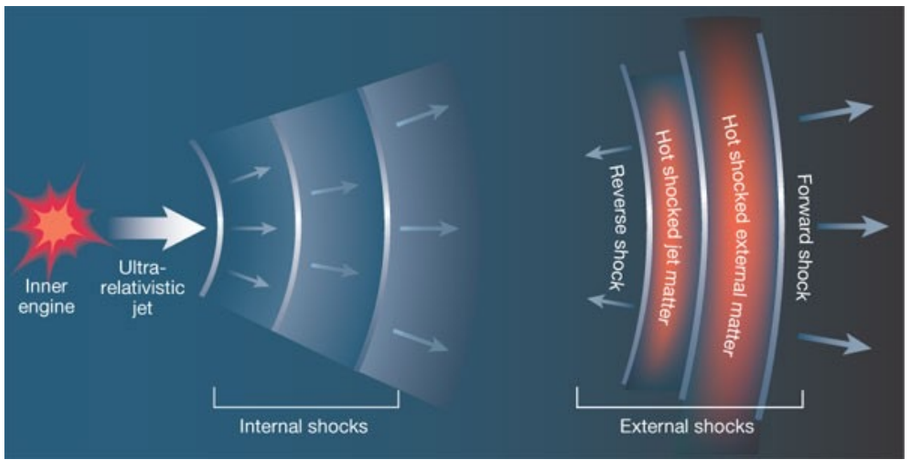

Figure 1.8: A schematic of a long GRB explosion. A newly created inner engine drives an ultra relativistic jet outwards of the star. Internal shocks close to the engine push the stellar material forward as the jet erupts. The external shocks encompass the shocked jet matter, as well as the external matter in the ambient medium. As the jet pierces through in a forward shock, some of the material also pushes back with a reverse shock. Figure adapted from Piran (2003).

The recognised theory for studying GRBs is the "fireball" model. According to the classical fireball model (Cavallo & Rees, 1978), a sudden conversion of a large amount of energy into a burst of concentrated γ-rays requires the formation of a cosmic fireball. The fireball respects a condition that electron-positron ($\gamma + \gamma \rightarrow e^- + e^+$) pair formation will surely persist and inhibit the escape of photons formed in the process until their energy has degraded to below some pair production energy threshold. This essentially points out the high opacities of the regions surrounding the unseen GRB engine. The inhibition is key for establishing limits on luminosities of rapidly varying γ-ray sources (Cavallo & Rees, 1978). The model recognised the existence of an astrophysical mechanism that could create a sudden fireball of photons via energetic processes from or near the surface of a compact object.

Revisions to the fireball theory by Rees & Meszaros (1992, 1994) addressed some of the discrepancies faced by the classical model. From the original fireball model, the collapse of the progenitor followed by expansion of the fireball results in conversion of the internal energy into baryon kinetic energy of the entrapped matter/gas in the fireball. However, the baryon kinetic energy causes the spectrum to be partly thermal as it is not converted into the observed relativistic photon luminosities, making the fireball less energy efficient. The associated timescales for the photon escape from the fireball are also closely tied to the opacities concerned as the flow transitions to optically thin, making them much shorter than observed, and also not clearly explaining recorded events that last much longer (Rees & Meszaros, 1992). This is the so called compactness problem. By considering a relativistic shocked scenario where the fireball has

transitioned to optically thin, relativistic shocks can reconvert the baryon kinetic energies to the observed non-thermal particle and photon luminosities. Both relativistic beaming and relativistic Doppler effect are at play to bypass the emitting region or source size issues of the compactness problem. Since the shocked scenario presents a forward and a reverse shock, forward shocks are commonly understood as long lasting, and thus powering the majority of observed broadband afterglows, whereas reverse shocks are short lived, typically observed within the very first few seconds to at most hours postburst. Since the first multi-wavelength afterglows were observed, improvements on modelling have been made. For example, Sari et al. (1998) and Granot & Sari (2002) provide some of the most comprehensive afterglow modelling equations, and modelling examples (see Wijers & Galama, 1999, for GRB970508) that have been broadly applied to investigate the physical parameters associated with GRB observations across the electromagnetic spectrum.

1.4.3 GRB Physics: Synchrotron Afterglows

GRBs are multi-wavelength phenomena. Temporal and spectral components at different frequency regimes typically estimate some (but not always all) relevant parameters of the total dynamics of a GRB. This means in order to estimate the full calorimetry of a specific burst, a comprehensive broadband approach is often the most convenient. This ranges from high energy γ-ray bands for studying the early time prompt emission, to radio frequencies for investigating the late time synchrotron afterglow. The primary assumption to describe the synchrotron afterglows is that a relativistic shell collides with and shocks a cold and uniform external medium of intrinsic particle density (n). Behind the resultant shock, the particle density becomes $4\gamma n$ and the energy density becomes $4\gamma^2 n m_p c^2$, where γ is the Lorentz factor for the shocked medium, and c is the speed of light (Sari et al., 1998). The accelerated electrons in the shock are accelerated to some power law distribution with some Lorentz factor γ_e, of a minimum of γ_m (Sari et al., 1998; Granot & van der Horst, 2014; Kumar & Zhang, 2015, and references therein for this review). This power-law distribution of the shocked electron population takes the form (Sari et al., 1998):

$$N(\gamma_e)d\gamma_e \propto \gamma_e^{-p} d\gamma_e, \tag{1.4}$$

where $\gamma_\mathrm{e} > \gamma_\mathrm{m}$. This power-law distribution is then integrated with respect to the Lorentz factor (γ_e) of the shocked electrons, with $N(\gamma_e)$ describing the shocked electron population density, and the power-law index (p) as the slope of the distribution. The slope is taken as $p > 2$ to maintain a finite amount of energy of the electrons (Sari et al., 1998). Furthermore, two dimensionless microphysical parameters arise from an assumption that a constant fraction of the shock internal energy is imparted into the electrons and the magnetic field, resulting in the fractions ϵ_e and ϵ_B as the electron energy density and the magnetic energy density of the magnetic field, respectively. The electron energy density ϵ_e is related to the minimum Lorentz factor of the electron distribution γ_m as (Sari et al., 1998):

$$\gamma_m = \epsilon_e \left(\frac{p-2}{p-1}\right) \frac{m_p}{m_e} \gamma, \tag{1.5}$$

where m_p/m_e is the proton-electron mass ratio. This relation is important as γ_m corresponds to the characteristic peak frequency ν_m of the synchrotron spectrum. Likewise, it also follows that the magnetic energy density ϵ_B is related to the magnetic field strength as (Sari et al., 1998):

$$\mathbf{B} = (32\pi m_p \epsilon_B n)^{1/2} \gamma c. \tag{1.6}$$

Naturally, the power radiated by a single shocked electron has a direct dependency on the magnetic field strength, and this can be defined through Larmor's equation in this context as (Sari et al., 1998):

$$P(\gamma_e) = \frac{4}{3} \sigma_T c \gamma^2 \gamma_e^2 \frac{\mathbf{B}^2}{8\pi}, \tag{1.7}$$

where σ_T is the Thomson cross-section for the electron, and with the synchrotron frequencies at which this electron radiates denoted as:

$$\nu(\gamma_e) = \gamma\gamma_e^2 \frac{q_e \mathbf{B}}{2\pi m_e c} \tag{1.8}$$

in the electron's local frame. This radiated power peaks at $P_{\nu,\max}$:

$$P_{\nu,max} = \frac{1}{3}\sigma_T m_e c^2 \frac{\gamma \mathbf{B}}{q_e}, \tag{1.9}$$

which is the ratio of equations 1.7 by 1.8. This peak spectral power is independent of γ_e, It is also noteworthy from equation 1.8 how the synchrotron frequency is related as $\nu(\gamma_e) \propto \gamma_e^2$. As the electrons lose their energy to radiation,i.e cooling (ν_c), a segmented spectrum with the components: a low energy tail ($\nu < \nu_c$ with $P_\nu \propto \nu^{1/3}$), a power-law segment ($P_\nu \propto \nu^{-1/2}$), and an exponential decline or cutoff ($\nu > \nu(\gamma_e)$) is expected. Essentially, the integration of the power-law distribution of the electrons results in the full synchrotron spectrum of the afterglow, segmented by characteristic frequencies ν_c, ν_{sa} and ν_m (see Sari et al. 1998; Granot & Sari 2002; Granot & van der Horst 2014; Kumar & Zhang 2015). These characteristic frequencies are typically associated with some peak flux F_ν of the afterglow, and may be understood as follows:

1. **Cooling frequency** ν_c : this is the frequency of the energetic electrons that lose a significant fraction of their energy in the dynamic timescale due to the effects of synchrotron cooling (Sari et al., 1998; Granot & Sari, 2002). The cooling frequency is usually associated with observations at optical and X-ray frequencies or even higher, and often times during the first few hours of the burst (Sari et al., 1998).
2. **Self-absorption frequency** ν_{sa}: synchrotron self-absorption frequency is the frequency below which the afterglow becomes optically thick to synchrotron emission (Sari et al., 1998; Granot et al., 1999). Low frequency (centimeter wavelengths) observations are typically the most prone to synchrotron self absorption (Katz, 1994). In this sense, low frequency radio light curves of GRBs are expected to peak much later as the fireball becomes optically thin (Wijers & Galama, 1999). Below ν_{sa} the canonical fireball is optically thick to synchrotron self-absorption (Resmi, 2017).
3. **Peak Frequency** ν_m: the peak frequency corresponds to the energy of the electron distribution. At early times, ν_m can be below the infrared and moving down to the radio bands. (Sari et al., 1998).

These frequencies are not fixed in time, and can be variable throughout the evolution of the afterglow as the peak flux F_ν changes (Granot & Sari, 2002). They in fact decrease in time. Together, these frequencies can be arranged in any order to yield a spectrum of the afterglow at various stages.

The spectrum is dependent on the temporal evolution of ν_m and ν_c in that effects of synchrotron cooling are relevant, however, radio observations are usually below ν_c. In this regard there are two cases, namely; fast cooling for which $\nu_m > \nu_c$, and slow cooling for which $\nu_c > \nu_m$, respectively.

The spectra for fast cooling ($\nu_m > \nu_c$) takes the form (Sari et al., 1998; Kumar & Zhang, 2015):

$$F_\nu = F_{\nu,max} \begin{cases} \left(\frac{\nu_{sa}}{\nu_c}\right)^{1/3} \left(\frac{\nu}{\nu_{sa}}\right)^2, & \nu_{sa} > \nu \\ \left(\frac{\nu}{\nu_c}\right)^{1/3}, & \nu_c > \nu \\ \left(\frac{\nu}{\nu_c}\right)^{-1/2}, & \nu_m > \nu > \nu_c \\ \left(\frac{\nu_m}{\nu_c}\right)^{-1/2} \left(\frac{\nu}{\nu_m}\right)^{-p/2}, & \nu > \nu_m \end{cases} \tag{1.10}$$

where the characteristic frequencies are in the order $\nu_{sa} < \nu_c < \nu_m$. In this scenario, the energetic electrons lose a significant fraction of their energy to radiation and thus cool towards γ_c within some dynamic timescale t.

Similarly, the synchrotron spectra for slow cooling ($\nu_c > \nu_m$) is denoted as follows (Sari et al., 1998):

$$F_\nu = F_{\nu,max} \begin{cases} \left(\frac{\nu_{sa}}{\nu_m}\right)^{1/3} \left(\frac{\nu}{\nu_{sa}}\right)^2, & \nu_{sa} > \nu \\ \left(\frac{\nu}{\nu_m}\right)^{1/3}, & \nu_m > \nu \\ \left(\frac{\nu}{\nu_m}\right)^{-(p-1)/2}, & \nu_c > \nu > \nu_m \\ \left(\frac{\nu_c}{\nu_m}\right)^{-(p-1)/2} \left(\frac{\nu}{\nu_c}\right)^{-p/2}, & \nu > \nu_c \end{cases} \tag{1.11}$$

with the characteristic frequencies ordered as $\nu_{sa} < \nu_m < \nu_c$. Despite the ordering of the characteristic frequencies being possible in anyway, for any case these will be driven by the dynamics in which a GRB evolves. The frequencies depend on the micro-phyiscs parameters of the plasma and are all variable in time. The practical known parameters or observables are usually evolution time, observing frequency, obtained flux, and these data are typically modelled through the function below (Granot & Sari, 2002):

$$F_\nu = F_{\nu_b} \left[\left(\frac{\nu}{\nu_b}\right)^{-s\alpha_1} + \left(\frac{\nu}{\nu_b}\right)^{-s\alpha_2} \right]^{-1/s} \tag{1.12}$$

for observations at multiple frequencies. This smoothly broken power-law has two slopes α_1 and α_2, where ν is the observing frequency, F_ν is the observed flux, ν_b is the breaking frequency, and F_{ν_b} is the flux at that breaking frequency. The parameter s is a smoothing factor. The power-law can also equally be written as a function of the observed fluxes against time as shown below:

$$F_\nu(t) = F_\nu(t_b) \left[\left(\frac{t}{t_b}\right)^{-s\alpha_1} + \left(\frac{t}{t_b}\right)^{-s\alpha_2} \right]^{-1/s}. \tag{1.13}$$

It is key to reiterate that the cooling frequency (ν_c) is typically not relevant for timescales at radio frequencies for a majority of GRB afterglows, with the peak frequency and the self absorption being the most common to constrain with centimeter observations. We utilise Equation 1.13 in Chapter 2 to model the MeerKAT observations of GRB190114C, and consider the implications of self absorption and the peak frequency, ν_{sa} and ν_m, on our results.

1.4.4 Interstellar Scintillation Effects on GRB radio afterglows

Interstellar scintillation (ISS) is a phenomenon that occurs when radio waves propagating from a point source experience distortions due to our charged interstellar medium (ISM) that has a variable electron density distribution (Rickett, 1986; Narayan, 1992; Goodman, 1997; Walker, 1998). These inhomogeneities in the ISM cause the observed patterns of irregularities or scatter in flux on an observed light curve of a compact radio source. There are two versions of this phenomenon, namely weak and strong scattering (Walker, 1998). Weak scattering occurs due to small fluctuations in the electron density between the observer and the source, with changes typically occurring within the first Fresnel zone (a prolate ellispoid around the line of sight between observer and target) (Granot & van der Horst, 2014). Strong scattering occurs when variations occur on scales smaller than the first Fresnel zone, resulting in severe modulations in flux. Strong scattering is further separated into two; namely refractive and diffractive scintillation respectively. Refractive scintillation is long-lasting (days to months) and broadband (Rickett, 1986), being observed at various frequencies. Diffractive scintillation or scattering, in contrast, is short term (minutes to hours) and causes modulation in narrow frequency bands.

The theoretical framework shows that ISS is strongly frequency dependent. Modest modulations (weak ISS) are expected at higher radio frequencies, while lower frequencies exhibit strong ISS effects. By taking the standard case assuming that ISS occurs at some thin screen at a distance d_{scr}, we can define the scattering strength ξ, a dimensionless parameter, as given by Walker (1998, 2001):

$$\xi = 7.9 \times 10^3 SM^{0.6} d_{scr}^{0.5} \nu_{obs}^{-0.7}, \tag{1.14}$$

where SM is the scattering measure and ν_{obs} denotes the observing frequency. The transition frequency between weak and strong scattering is then defined as (Goodman, 1997):

$$\nu_{trans} = 10.4(SM_{-3.5})^{6/17} d_{scr}^{5/17} \text{ GHz}, \tag{1.15}$$

where $SM_{-3.5} = (SM/10^{-3.5} m^{-20/3})$ kpc. This equation states that for $\nu_{obs} < \nu_{trans}$ strong scattering persists, and for $\nu_{trans} < \nu_{obs}$, weak scattering persists. There are modulation indices and angular scales associated with ISS, and these are very useful in that they can help constrain the angular size of the source as the GRB afterglow expands over time. This comes as the angular size of the jet starts out collimated and smaller than the angular scintillation scales, and expands over time until it surpasses these scales, after which variations in flux diminish. The angular scales are expressed in terms of the Fresnel angle θ_{F0}:

$$\theta_{F0} = 6.3 \times 10^4 SM^{0.6} \nu_{trans}^{-2.2} \ \mu\text{as} \tag{1.16}$$

1.4.5 Very High Energy GRBs

Very High Energy (VHEs) GRBs are generally defined as GRBs with γ-ray photons in excess of ≥ 100 GeV (Ajello et al., 2019; Rhodes et al., 2020). A detailed analysis of all the GRBs observed by *Fermi*-LAT over a decade, has shown these GRBs to be very rare (Ajello et al., 2019), with only GRB130427A being the closest at 95 GeV (Ackermann et al., 2014). The HESS follow up of GRB100621A, which was also a very bright GRB, resulted in no VHE emission being observed, and thus no constraints on inverse Compton Emission (H. E. S. S. Collaboration et al., 2014). An earlier very bright GRB080319B had detections of optical photons suggesting origin from a synchrotron process, and γ-ray emission likely due to the inverse Compton scattering of those optical photons (Kumar & Panaitescu, 2008). These GRBs could not fully constrain inverse Compton emission. The detection of TeV photons for GRB190114C was the first direct observation of the phenomenon from a GRB (MAGIC Collaboration et al., 2019a). This was then followed by the discovery of an even brighter GRB221009A (Lesage et al., 2023), which had photons up to 18 TeV (Huang et al., 2022). Other GRBs in this class have been characterised by sub-TeV emission with different levels of significance, namely short GRB160821B (Acciari et al., 2021), GRB 180720B (Abdalla et al., 2019), GRB 190829A (H. E. S. S. Collaboration et al., 2021), and GRB 201216C respectively (Fukami et al., 2022). Low frequency radio observations of these VHE GRBs are not plentiful. In fact our MeerKAT observations of GRB190114C, coupled with uGMRT observations reported by (Misra et al., 2021), and MeerKAT observations of GRB190829A by (Rhodes et al., 2020) essentially some of the first for the sample. And from these observations, forward shock emission has been studied, scintillation effects have been used for fireball size constraints, and the host galaxy components have been constrained from the late time monitoring, with late time observations being useful for full calorimetry studies of the VHE GRBs. Low radio frequency observation campaigns of VHE GRBs are also lacking, which misses the chance to better constrain synchrotron self-absorption effects on these events.

1.5 Thesis Overview

The ambit of this thesis is to study the gamma ray burst GRB190114C with MeerKAT, as well as to attempt a commensal transients survey in the GRB field to repurpose the data, since a substantial amount of observations of the field were performed. In Chapter 1, I have summarised the relevant literature and theories pertaining to the project. In Chapter 2, I provide a thorough overview on the discovery of GRB190114C (MAGIC Collaboration et al., 2019a), and our participation in the international broadband effort confirming inverse Compton scattering as the mechanism for the observed teraelectronvolt photons (MAGIC Collaboration et al., 2019b). I then present our MeerKAT monitoring campaign on GRB190114C; the images we created, light curve we observed, its simple modelling, and explain our results and discussing their implications in the context of reviewed literature from Chapter 1. In chapter 3 I present results of a search for transients in the GRB190114C field using the LOFAR transients Pipeline, "TraP". The pipeline has been well tested with MeerKAT data, with Driessen et al. (2020) and Andersson et al. (2022) having discovered the first and second radio transients by the telescope, respectively. The pipeline has been made available in the local infrastructure at the IDIA research cloud facility since late 2021, and I use it here,

affectionately called “ThunderTraP”, in the search for transients and variables. In chapter 4 I summarise the met and unmet ambits of this thesis, as well as outline the implications of all results obtained. I then draw conclusions and look at future prospects for this work.

Chapter 2

GRB190114C

2.1 Discovery

On 14 January 2019 at T_0 20:57:03.19 UT (universal time), the Neil Gehrels *Swift* mission (Gehrels et al., 2004) with its onboard Burst Alert Telescope (BAT) in concert with the Gamma Ray Burst Monitor (GBM) onboard the *Fermi* satellite (Meegan et al., 2009), observed GRB190114C and rapidly localised the optical counterpart. The initial *Swift* light curves showed a very bright multi-peaked source that lasted for approximately 25 seconds, with a trigger sent to ground based telescopes with the location of the transient as per usual *Swift* protocol. The total duration, T_{90}, of the GRB was recorded as 116 s and 362 s by *Fermi* (Hamburg et al., 2019) and *Swift*-BAT Gropp et al. (2019) respectively, which is the time interval within which 90% of the photons have been counted. During this time, the initial isotropic equivalent energy of the GRB measured by *Fermi*-GBM in the $1 - 10^4$ keV range was $E_{iso} \approx 3 \times 10^{53}$ erg. At about 50 s post burst (i.e at $T_0 + 50$ s), the Major Atmospheric Gamma Imaging Cherenkov Telescopes (MAGIC) (Aleksić et al., 2016a,b) followed the Swift trigger and slewed to the GRB sky location. The real time analysis of the observation by MAGIC showed excess γ-ray emission with $> 20\sigma$ significance at > 300 GeV within the first 20 minutes of observing (Mirzoyan et al., 2019). In their real time analysis, Mirzoyan et al. (2019) detailed the emission of up to 1 TeV (teraelectronvolt) from the gamma ray burst, and the results were consequently reported in MAGIC Collaboration et al. (2019a).

GRB190114C had a highest recorded apparent isotropic equivalent luminosity of $L_{iso} \approx 3 \times 10^{49}$ erg s^{-1} at 0.3-1 TeV energies, with an isotropic equivalent energy of $E_{(0.3-1TeV)} \approx 4 \times 10^{51}$ erg (MAGIC Collaboration et al., 2019a). This made it the brightest known GRB at such energies. Essential corrections to MAGIC data were made to account for the diffuse extragalactic background light (EBL) from intergalactic space which causes significant absorption, particularly to γ-ray spectra at cosmological distances. This effect is also seen in Infrared, optical and UV wavelengths. The MAGIC light curve was fitted with a simple power-law, which constrained the TeV band energy to $E_{(0.3-1TeV)} \approx 2 \times 10^{52}$ erg. This energy was then set as a benchmark lower limit to the TeV band output, since it was the first time it was observed for a GRB. This newly introduced TeV light curve further showed similar properties of power-law decay in comparison to keV and GeV light curves, with no recorded breaks or cutoffs, but a monotonic decay (see red points in Figure 2.1). Further analysis suggested that the TeV emission is associated with the afterglow emission rather than the initial prompt emission. If associated with the prompt emission, irregular variabilities in the light curves would have been expected and these are not seen in the light curves (MAGIC Collaboration et al., 2019a).

Further investigation on the nature of the emission, with an assessment of plausible mechanisms, synchrotron emission by ultrahigh energy protons was hypothesised. This mechanism was eliminated due to the intrinsic low radiative efficiency of this hadronic process. However, since the radiated power and temporal behaviour observed suggested association with the afterglow, Inverse Compton up-scattering of

ambient low-energy photons to high energies by electrons in the external shock was a physically compelling mechanism for interpreting the data (MAGIC Collaboration et al., 2019a). Essentially, the evident similarities in the light curves support the interpretation of the TeV emission as associated with the afterglow, see Figure 2.1. Since Inverse Compton radiation had previously been suggested by GRB theories but had never been convincingly detected before, this was the first direct evidence of the phenomenon from a GRB. This new addition of a possibly common emission component of GRB afterglows beyond synchrotron radiation was a significant milestone in the study of gamma ray bursts.

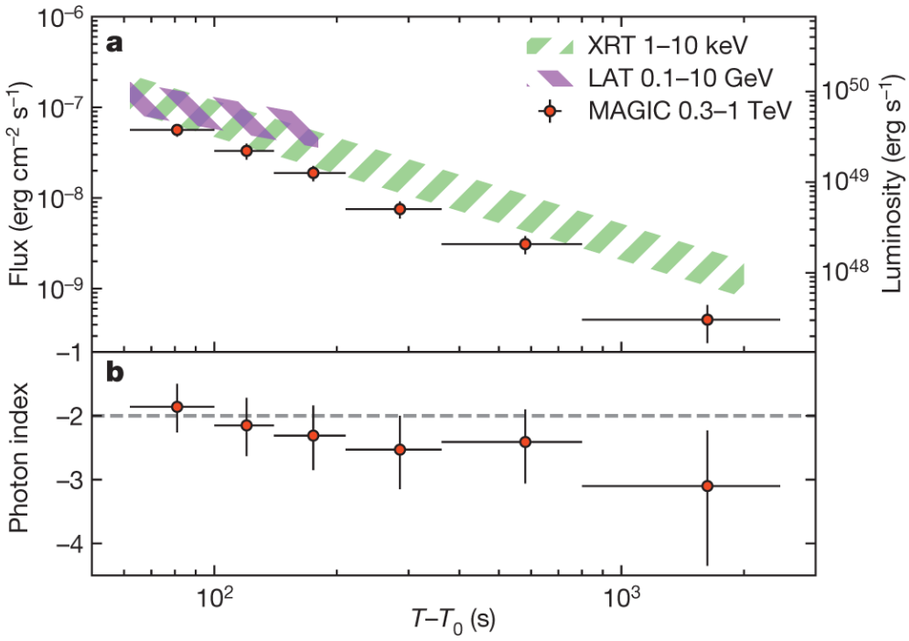

Figure 2.1: The TeV lightcurve for GRB190114C. The MAGIC data in red crosses for the 0.3-1 TeV energy range, as well as data from the *Fermi* Large Area Telescope (LAT) at GeV, and *Swift* X-ray Telescope (XRT) at keV energies, in purple and green bands respectively. After extragalactic background light (EBL) corrections, the fluxes and luminosities on the vertical axes are plotted against time on the horizontal axis. The bottom curve reveals the temporal evolution of the photon index fitted with a simple power-law. Adapted from the MAGIC Collaboration et al. (2019a).

2.2 MAGIC broadband Follow up

In supportive augmentation of the initial analysis and the hypothesis of Inverse Compton scattering, MAGIC Collaboration et al. (2019a) was followed up by an international collaboration (which we participated in) with data contributions for the multiwavelength study of GRB190114C (MAGIC Collaboration et al., 2019b). This made GRB190114C a GRB event with the most expansive coverage across the electromagnetic spectrum, spannning 17 magnitude orders in energy from as low as 5×10^{-6} eV to an astonishing 10^{12} eV. This result is shown in Figure 2.2 and explained in following paragraphs. The Hubble Space Telescope (HST) located and identified the host galaxy as a spiral with the GRB located close to the galactic nucleus. The detection of strong calcium, hydrogen, and potassium absorption lines in the spectrum of the afterglow led to the redshift $z = 0.4245 \pm 0.0005$ being confidently established (Selsing et al., 2019; Castro-Tirado et al., 2019), placing the GRB at a cosmic look-back time of about 4.5 Gyrs.

Using 6 space observatories and 15 ground based telescopes, including our early MeerKAT radio observations, one of the most extensive early temporal evolution of a gamma ray burst over the electromagnetic spectrum was recorded MAGIC Collaboration et al. (2019b). This spectral coverage is arguably only rivaled by a few other well studied bursts like GRB030329, GRB 080319B, and GRB130427A. From the high energy spectral regimes, the multi-peaked onset light curves of GRB190114C showed a complex evolution for a duration of 25 s with the flux ultimately decaying smoothly by a simple power-law thereafter. The

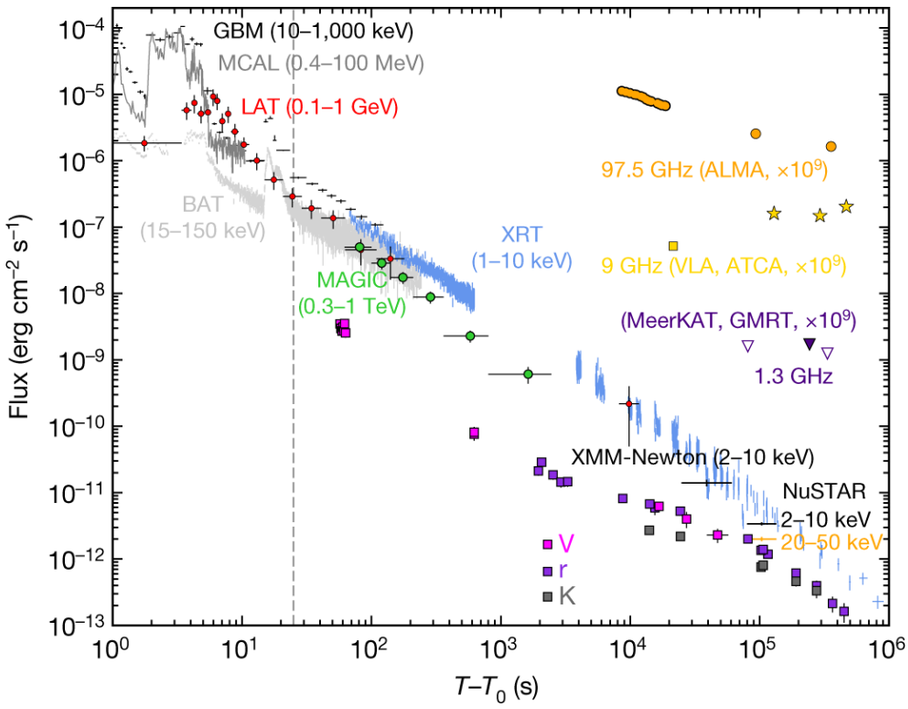

Figure 2.2: MAGIC's GRB190114C broadband light curves, from γ-rays to radio frequencies. The 0.3-1 TeV curve is in green circles. The early time (before $\sim$ 10 s) multi-peaked X-ray curves (grey and red) are followed by a relatively smooth decay, with the end of the prompt phase marked by the dashed vertical line. The optical bands (in filters V, r and K) have been corrected for local and GRB host galaxy extinction. The radio curves are scaled by 10^9 for definition (MeerKAT (open) and uGMRT (closed) in purple triangles, ATCA in yellow stars, ALMA in orange circles, and VLA in a yellow square). Adapted from the MAGIC Collaboration et al. (2019b).

afterglow was estimated to have started within at least 10 s postburst, thus indicative of an initial bulk Lorentz factor of a few hundreds (here $\gamma \sim 300 - 700$).

Detections with *Swift*-XRT (1-10 keV) and MAGIC (0.3-1 TeV) within a minute of the BAT trigger also showed power law temporal decays. In particular, emission in the 0.3-1 TeV band was observable with MAGIC for as long as 40 minutes, significantly longer than the duration of the initial prompt phase (MAGIC Collaboration et al., 2019b). The near infrared (NIR) to optical light curves showed complex behaviour suggestive of a reverse shock dominating the emission. The observed fast decay additionally narrowed down the characteristic peak frequency (ν_m) as crossing the optical band around that time. A similar trend of decay was also observed in the millimetre regime, with the emission dominated by the reverse shock up to 5 hours post burst (Laskar et al., 2019).

At the long wavelength end of the electromagnetic spectrum, first radio detections of GRB190114C were reported by numerous facilities such as the Atacama Large Millimeter Array (ALMA) confirming a linearly polarised reverse shock (Laskar et al., 2019), the Australia Telescope Compact Array (ATCA), the upgraded Giant Metrewave Radio Telescope (uGMRT), and the Karl G. Jansky Very Large Array (VLA). MeerKAT also observed GRB190114C as early as 0.94 days post burst (Tremou et al., 2019). These observations collectively constrained the self-absorption frequency to be between the radio and optical at about 10^4 s, evolving from high frequencies and ultimately low frequencies. MeerKAT (1.28 GHz) observations, coupled with the uGMRT at 1.26 GHz supported this view, indicating that $\nu_{\rm sa} \sim 1$ GHz at 10^5 s (MAGIC Collaboration et al., 2019b). This result meant that the flux of the GRB190114C was synchrotron self absorbed at radio frequencies during the first radio observations reported (≤ 5 days postburst). Furthermore, trends of a constant radio flux in time supported a wind shaped external medium for GRB190114C, as expected for slow cooling between the self-absorption (ν_{sa}) and peak frequencies (ν_m).

2.3 MeerKAT observations of GRB190114C

The afterglow of GRB190114C was studied at radio frequencies by various radio telescopes around the world at early times ≤ 1 day. These included ALMA, the ATCA, VLA, uGMRT and MeerKAT. The early time flux levels of the MeerKAT and uGMRT observations contributed towards constraining the synchrotron self absorption frequency to around 1 GHz at around 3 days after the burst (MAGIC Collaboration et al., 2019b). In this section I present the MeerKAT monitoring campaign of GRB190114C, and report the results and analysis of our radio observations. I provide images of the field and the GRB, a detailed description of the observed light curve and modelling, as well as the physical meaning of our results, while also comparing to currently available literature on GRB19114C.

2.3.1 Rapid Response and Monitoring

In light of GRB190114C proving to be enigmatic from early post trigger observations, especially with the MAGIC team reporting TeV photons from the explosion (Mirzoyan et al., 2019), early MeerKAT observations were acquired through the Director's Discretionary Time (DDT). MeerKAT slewed for the first observation of GRB190114C within 0.94 days post-burst on 15 January 2019 (Tremou et al., 2019), with 3 additional follow up epochs until about 7 days after the burst event. Following the GRB evolution during the initial observations, further DDT observations were obtained, followed by Open Time data (OT), proposal ID SCI-20190418-PW-01, at later times, see Table 2.1. The full MeerKAT monitoring campaign of this GRB is reported in this thesis. All the observations were coordinated by the operators team and staff at SARAO.

2.3.2 MeerKAT Observations

The observations of GRB190114C were consistently conducted with over 61 MeerKAT antennas accessible throughout the monitoring campaign. Observations were all in the L-band at a central frequency of 1284 MHz (1.28 GHz). The epochs are each split into 4096 channels with an 856 MHz span in bandwidth. The observing strategy for each epoch was to observe the bandpass and flux calibrator (primary), J0408-6545, at the start and end of each epoch for 10 minutes each scan. And then the telescope alternated 10 minutes on the target, GRB190114C, and a 60 second scan on the phase and amplitude calibrator (secondary), J0240-2309, for the duration of each observation. The time resolution for the observations was a MeerKAT default sampling time stamp of 8 seconds per scan.

The observing strategy was maintained for the first 11 epochs. Adjustments were made for the last 2 epochs for deeper observations of the target (i.e duration of 3.9 and 5.9 hours for the closing 2 observations respectively). This strategy adjustment came after the afterglow had peaked in the observing frequency (1.28 GHz), and with late time fluxes dropping to just below 100 μJy. This suggested that the late time emission was likely dominated by the host galaxy. The epochs were an average of 2.7 hours total observing time each for the duration of the monitoring campaign spanning approximately 352 days. An aggregate of 13 successfully run observations was achieved without any reported systematic issues. These observations provide the only extensive low frequency radio sampling of GRB190114C at 1.28GHz. A summary of the observing strategy is supplied by the observation log, see Table 2.1. Nearly half of the observations were obtained within the first 25 days, with the remainder scheduled at least one month apart.

Observation Dates	Start-End Times (UTC)	Time on target (s)	Antennas used	Proposal
2019 Jan 15	18:14:54.8 - 20:44:35.0	8380	63	DDT
2019 Jan 18	16:31:25.3 - 19:04:49.4	8564	63	DDT
2019 Jan 20	20:38:38.6 - 23:14:10.6	8724	63	DDT
2019 Jan 22	15:49:59.3 - 18:28:27.3	8780	63	DDT
2019 Feb 01	14:07:59.9 - 16:16:28.6	7101	61	DDT
2019 Feb 08	12:39:41.3 - 14:43:22.1	6813	60	DDT
2019 Feb 20	18:07:56.0 - 20:12:56.9	6853	61	DDT
2019 Mar 08	10:31:55.9 - 12:33:28.8	6685	58	DDT
2019 May 04	08:02:46.0 - 10:09:14.8	6949	61	OT
2019 Jun 02	10:54:09.5 - 13:00:38.3	6933	60	OT
2019 Aug 07	04:01:48.5 - 06:02:25.5	6581	62	OT
2019 Oct 29	18:16:39.9 - 22:10:53.9	12583	60	OT
2020 Jan 01	15:52:49.4 - 21:47:16.4	19852	60	OT

Table 2.1: The MeerKAT observation schedule and strategy log for the GRB190114C campaign. This indicates the dates and times of the observations, times on target, as well as the number of antennas used in each observation. The campaign obtained data through DDT and OT proposals.

2.4 Methods: Data Reductions and Analysis

2.4.1 Reduction Pipeline

The data from the MeerKAT telescope are typically stored in SARAO storage facilities. For analysis, data are retrieved from SARAO through an online tool used to "push to IDIA". The online tool allows data transfer between SARAO and the Ilifu cloud computing facility (IDIA) for data reductions, imaging, and analysis. For the GRB190114C campaign, each of the observation measurement sets were at least 250 gigabytes in disk storage size, with 2 late observations being 1.2 terabytes each. These data, totalling just over 5 terabytes, were copied to a user working directory, since creating symbolic links to the raw data is advised against to avoid errors.

The data reduction is performed by executing a set of instructions in a pipeline. This is a series of python scripts detailing various reduction tasks using relevant software packages for each stage of the reduction. To begin, we eliminate radio frequency interference (RFI) effects using AOFlagger, followed by calibrations through standard CASA commands, and imaging is finally performed using WSClean. The target fluxes are then calculated through PyBDSF in order to plot the MeerKAT light curve of the GRB afterglow. The steps are outlined in the following subsections.

2.4.2 Flagging Radio Frequency Interference (RFI)

We utilise AOFlagger to remove bad data from the measurement sets. This is an automated RFI mitigation software package that was developed and used at LOFAR (Offringa et al., 2012) by the Netherlands Institute for Radio Astronomy (ASTRON). The morphological algorithm is designed to detect and flag all corrupted data channels from a radio observation measurement set. This software package is available within the Ilifu framework, and was employed on all the raw data sets to flag all corrupted channels. This is essential as RFI can make calibrations more challenging, or have negative effects on the quality of final images. We performed the flagging by executing a flag.py script. The script opens the measurement set and runs the algorithm to search for corruptions in time or frequency planes. When these are detected, the channels are flagged accordingly.

2.4.3 Averaging

After flagging the measurement sets, the visibilities are duplicated and averaged in time and frequency by a factor of 8. This is especially useful for handling the large volumes of the data sets. In the average.py script, we exploit the mstransform parameter in CASA, VERSION 4.7.1-REL (R39339), specifying the datacolumn, and setting the chanaverage and timeaverage to true. Likewise, the chanbin is set to '8', and the timebin is 8 seconds respectively, consistent with the time resolution of the observations. The realmodelcol and usewtspectrum are set to 'true', while hanning is set 'false' to avoid writing the output to the disk storage multiple times. This averaging helps manage the large data volumes as mstransform applies all the transformations on the fly without writing to the disk memory. The channel and time averaging takes flags and weights into account and the resultant output is stored as a WEIGHT_SPECTRUM, denoted by extension _wtspec.ms. After averaging, the original measurement set can be securely removed from the working directory to clear out some disk storage, while the average output will be used for further analysis.

2.4.4 Calibrations

Calibrations are performed using standard commands in CASA VERSION 4.7.1-REL (R39339). Task setjy is used for calibrator models to compare the observed visibilities with well tested models for the calibrators. After applying a model for the bandpass and flux calibrator (primary), initial phase only, as well as antenna based delay corrections are performed using task gaincal. We then solve for bandpass corrections on the primary using task bandpass. We further reapply setjy with a model for the phase and amplitude calibrator (secondary), and solve for complex gains using task gaincal, all while bandpass and delay solutions are applied on the fly. We use gaincal to solve for complex gains on the primary. Since the flux of the primary is known, this flux is used to scale the gain corrections on the secondary and target fields using task fluxscale. We use applycal to apply all the calibration solutions on the target field. Finally task flagdata is implemented with autoflag modes rflag and tfcrop to implement statistical corrections (i.e rms calculations for visibilities) and flag any outliers in the time-frequency plane.

2.4.5 Imaging with WSclean

After calibrations, the visibilities are imaged using WSCLEAN (Offringa et al., 2014). This is a wide-field imaging package that has been developed for and tested at the Murchison Widefield Array (MWA) in Western Australia. The package utilises a w-stacking algorithm which grids the visibilities as layers and implements various deconvolution procedures to create a mosaic of the true sky image of the target. We loaded the calibrated data and applied the Briggs weighting scheme (Briggs, 1995), setting the robust parameter to -0.7. We used gain=0.1, mgain=0.85, and set niter to 30 000 iterations to obtain the widefield (8192×8192 pixels) images at 1.5 arcsec scale. All images are in the L-band, in full polarisation, i.e Stokes I.

2.4.6 Flux Calculations with PyBDSF

To determine the fluxes of the target, we interactively use the Python Blob Detection and Source Finder (PYBDSF VERSION 1.8.14), which was also developed by ASTRON for LOFAR (Mohan & Rafferty, 2015). The software decomposes radio images into multiple Gaussians at the pixel location of each source, calculates source parameters, and outputs results in table formats. To perform this, we loaded each image and set advanced_options = true to exploit the full package advantages. We set a detection threshold thresh_pix = 5.0 for confident 5σ level source detections, and used thresh_isl = 3.0 as the 3σ analysis threshold for flux measurements. We applied a trim_box at the region of the GRB in order to avoid calculating fluxes for all sources in the field, which would be time intensive. The calculations are then ran by process_image, with an option to view outputs via show_fit. We then wrote the output to .csv format catalog tables detailing source RA, Dec, flux, uncertainty in flux, image rms and other such parameters. To the flux uncertainties, we add in quadrature, a 10% systematic flux uncertainty intrinsic to MeerKAT (see MAGIC Collaboration et al. 2019b,Mauch et al. 2020 and Rhodes et al. 2020).

2.5 Results: GRB190114C as seen by MeerKAT

Here we present the MeerKAT results of the GRB190014C field. From MeerKAT imaging, we note that this is an incredibly source rich field, with numerous background radio galaxies, and other potential transient sources.

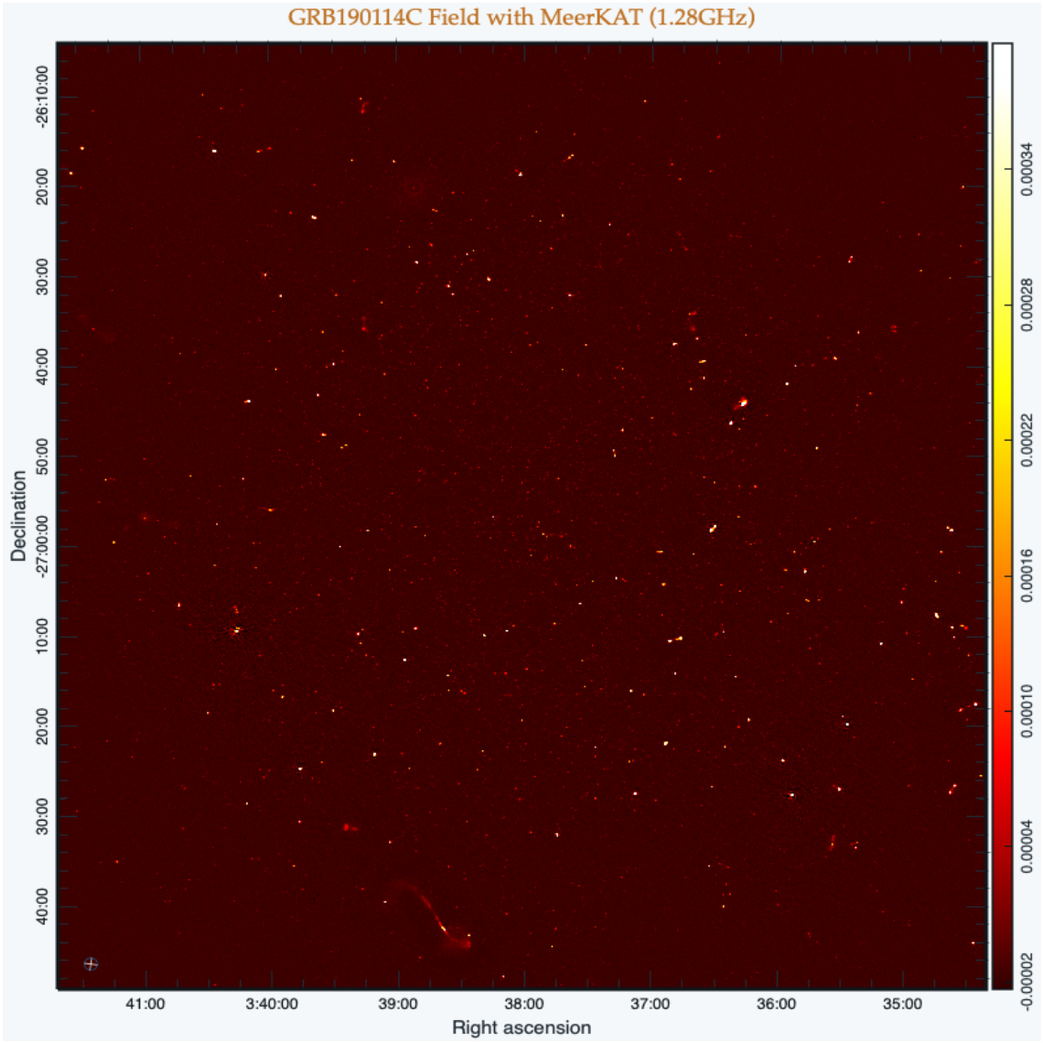

Figure 2.3: The MeerKAT field image of GRB190114C field. The image is a concatenated stack of all the available 13 observations of the field. The image restoring beam is 5.29" × 4.42" and a position angle of -8.09 degrees. North is up, east is to the left. The beam is indicated at the bottom left of the image and spans 10 × 10 pixels.

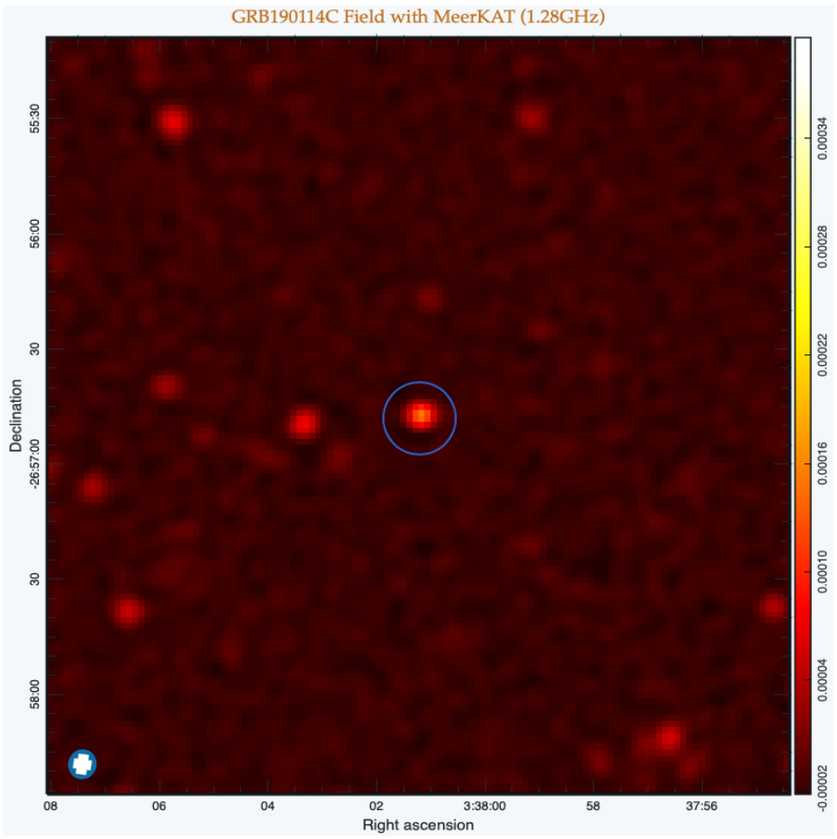

Figure 2.4: A zoomed in image of the GRB190114C field, with the GRB encircled at the centre. The image is a concatenated stack of all the available 13 observations of the field. The beam on the bottom left corner is 10×10 pixels across.

2.5.1 MeerKAT Fluxes

Here we present the table of results for MeerKAT observations of GRB190114C (see Table 2.2). Our dedicated monitoring campaign started within just less than a day post-burst, and spans almost 1 year. Our observations were at a duration of over 2 hours each epoch, including calibrators. Table 2.2 shows the observed fluxes and their errors. Our quoted errors include a 10% systematic flux uncertainty added in quadrature (see MAGIC Collaboration et al. 2019b and Rhodes et al. 2020). This addition is done to correct an intrinsic flux calibration error by MeerKAT. The measured rms values for our images are nearly all at the same order of magnitude, asserting our image quality and consistency at each epoch.

Days postburst $(T - T_0)$	Integration time (Δ_T) hr	Fluxes (μJy)	RMS (μJy)
0.94	2.5	119 ± 16	12
3.87	2.6	92 ± 14	11
6.04	2.9	146 ± 19	12
7.84	2.6	464 ± 48	10
17.76	2.1	170 ± 24	18
24.70	2.1	160 ± 19	11
36.93	2.1	284 ± 31	13
52.61	2.0	183 ± 26	18
109.51	2.1	224 ± 25	11
138.63	2.1	172 ± 20	12
204.34	2.0	93 ± 18	15
287.97	3.9	97 ± 14	7
351.91	5.9	105 ± 15	7

Table 2.2: The MeerKAT observation results for the GRB190114C campaign at 1.28 GHz. The table indicates the number of days post burst $(T - T_0)$, duration of each observation (taken at midpoint), recorded fluxes, flux errors, and the background noise (RMS).

2.5.2 MeerKAT Light Curve of GRB190114C

The MeerKAT light curve of this TeV GRB shows the evolution of the burst from as early as just less than a day to just under a year at approximately 352 days (see Figure 2.5). The light curve indicates complex behaviour of significant scatter, as seen by flux fluctuations throughout our monitoring campaign. This behaviour is common in low frequency observations of GRBs, and can be alluded to interstellar scintillation effects. Despite this, perceptible trends of a rise and a decay can be seen on the light curve, generally signalling a two slope power-law evolution.

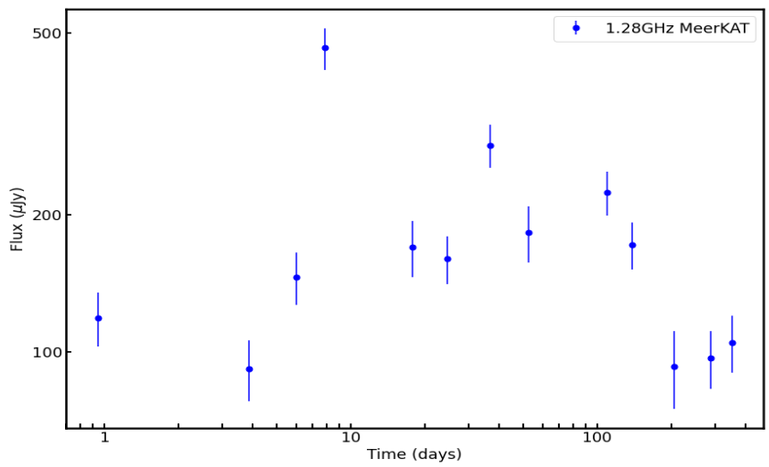

Figure 2.5: The light curve of GRB190114C as observed by MeerKAT at 1.28 GHz. The error bars include an intrinsic MeerKAT flux calibration uncertainty of 10% added in quadrature.

2.5.3 MeerKAT Light Curve Modelling

The MeerKAT light curve as seen in (Figure 2.5) indicates quite a shallow rise in flux, coupled with some fluctuations that occur during this rising period. The variation is especially pronounced close to 10 days, and continues for the first 50 days. A clearly sharp turn over occurs around 100 days post-burst, with a steep decay dominating thereafter. The flux drops to just below 100 μJy at 200 days, with a level-off at the last epoch. Applying a similar approach to Rhodes et al. (2020), we model the MeerKAT light curve with a smoothly broken power law in time. This power law takes the form:

$$F_\nu(t) = F_\nu(t_b)\left[\left(\frac{t}{t_b}\right)^{-5\alpha_1} + \left(\frac{t}{t_b}\right)^{-5\alpha_2}\right]^{-1/5} + G \tag{2.1}$$

which is essentially Equation 1.13 restated, with the addition of a constant parameter G. We use this parameter to constrain the flux contribution of the host galaxy to the observed afterglow emission. So in the context of our plotted light curve, Figure 2.5, the power law demonstrates that the observed MeerKAT light curve rises with some slope α_1. It breaks or turns over at some time t_b, with the turnover or break marked by some flux $F_\nu(t_b)$, which is not necessarily the maximum observed flux. This is followed by a decay of a slope α_2. We use a fixed factor $s = 5$, to control the smoothness of our curve fitting.

In PYTHON, we utilise a Markov Chain Monte Carlo (MCMC) sampler, namely EMCEE (Foreman-Mackey et al., 2013), to perform the model fitting. This enables us to determine our free parameters; $F_\nu(t_b)$,t_b, α_1, α_2, and G respectively. We set priors in this form; $(0.0 < F_\nu(t_b) < 500)$, $(0.0 < \alpha_1 < 2.0)$, $(-6.0 < \alpha_2 < 0.0)$, $(0.0 < t_{break} < 400.0)$, $(0.0 < G < 500)$. We used 300 independent walkers with 5 000 steps each to explore the full parameter space, and burned in the first 2000 steps. Our iterations result in 900 000 flat samples. We apply χ^2 analysis to find the maximum likelihood of the best fit, which we quote at the 50th percentile of the sample population. Our fit is shown in Figure 2.6.

In Figure 2.7, we indicate our MCMC results for our calculated fit parameters. Our posterior distribution indicates the sampling results in calculating each one of these free parameters from the given prior settings. We quote our parameter estimates at the median of the posterior, with the uncertainties being at the quantiles 16% and 84% respectively. The slope α_2 appears to be inherently too steep from our marginalised distribution in Figure 2.7. We find that relaxing the prior settings for this parameter results in higher reduced χ^2 values and gives poor fits to the data within physical reason. In fact, the simplest $\alpha_2 < 0$ prior gives the worst fit to the light curve, rendering our obtained value the most credible estimate for this slope. We do take some due caution in interpreting this part of the results. A summary of these estimates is given below in Table 2.3:

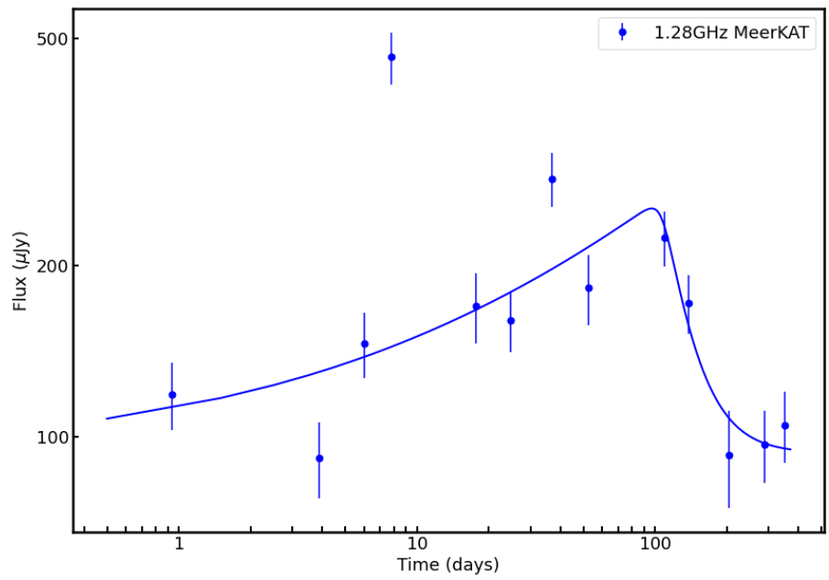

Figure 2.6: MeerKAT light curve for GRB190114C fitted with a smoothly broken power law. The fit indicates a consistent rise, and a sharp decay at turn over before stabilising at the end. We use these two slope trends to constrain the physical evolution of the GRB.

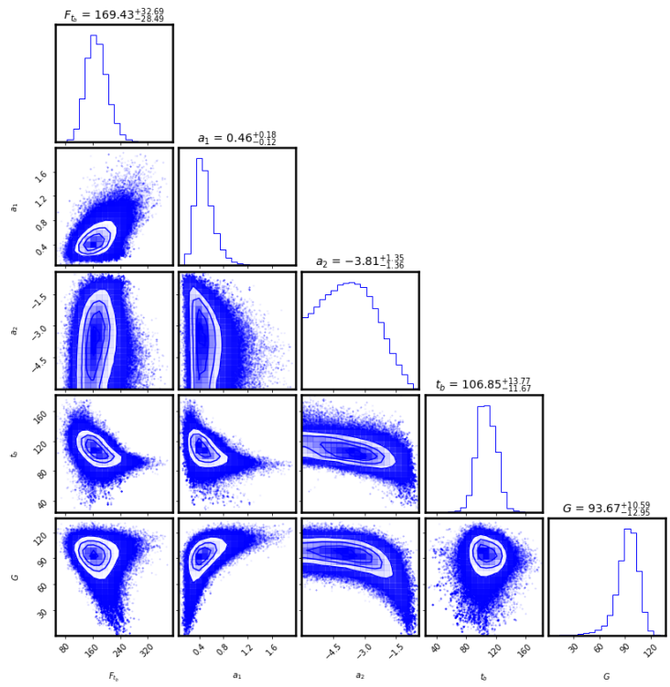

Figure 2.7: The MCMC corner plot indicating the posterior probability distributions of our fit parameters.

$F_\nu(t_b)$ (μJy)	α_1	α_2	t_{break} (days)	G (μJy)
170^{+33}_{-29}	$0.5^{+0.2}_{-0.1}$	-3.8 ± 1.4	107^{+14}_{-12}	94^{+11}_{-13}

Table 2.3: The best fitting parameters for the MeerKAT light curve.

2.5.4 MeerKAT Light Curve Interpretation

Broadband light curves of GRBs are generally well explained by the fireball model. In this model, the core collapse of a massive progenitor generates a relativistic outflow that interacts with the circumburst medium (Rees & Meszaros, 1992; Sari et al., 1998; Granot & Sari, 2002). This results in a pair of shocks; one moving into the ambient medium (forward shock), and one moving back into the ejecta (reverse shock). These shocks render an amplification of magnetic fields, accelerating charged particles to the synchrotron emission that is variable in time. The reverse shock is usually short lived, observed in the first few seconds to hours in the ultra violet to optical wavelengths. The forward shock is long-lasting and broadband, often generating the majority of observed GRB afterglows, see van der Horst (2007) and Granot & van der Horst (2014) for additional review. We apply this fireball model to interpret the trends observed in the MeerKAT light curve of GRB190114C at 1.28 GHz.

The observed pick up in flux observed during the first ~ 100 days postburst corresponds with the self absorption frequency being below the observing frequency, with the order $\nu_{\rm sa} < \nu < \nu_{\rm m} < \nu_{\rm c}$. In this ordering, the light curve is theoretically expected to rise as the peak frequency $\nu_{\rm m}$ approaches lower frequencies (Granot & Sari, 2002). In this context, our fitted slope of $\alpha_1 = 0.5^{+0.2}_{-0.1}$ is consistent with an optically thick forward shock propagating into a homogeneous external medium (medium density $k = 0$), where the rise follows $F \propto t^{\frac{1}{2}}$ (Granot & Sari, 2002). Since we are providing low frequency observations which are commonly at the level of synchrotron self absorption frequency, ν_{sa}, we definitively rule out the possibility of ν_{sa} being the reason for the rising trend of our light curve. If ν_{sa} was at play, a significantly steeper rise of $F \propto t^{\frac{5}{4}}$ or $F \propto t^{\frac{7}{4}}$, would be expected for a forward shock in both a homogeneous (medium density $k = 0$) or a wind environment (medium density $k = 2$) respectively (Granot & Sari, 2002).

The passage of either or both the peak frequency and the self absorption frequency through the observing band is marked by the turn over or break in the light curve with the order $\nu_{\rm sa} < \nu_{\rm m} < \nu < \nu_{\rm c}$, followed by a decline in flux (Granot & Sari, 2002; van der Horst et al., 2005). This passage is seen at $t_{break} = 107^{+14}_{-12}$ days. We interpret this passage as the peak frequency ($\nu_{\rm m}$) crossing the MeerKAT observing band at this late time, but also as a possibles jet break due to the dramatically steep decay component that follows the break. This decay component of the light curve has an estimated slope of $\alpha_2 = -3.8 \pm 1.4$. Even with significant uncertainty, this slope proves to be too steep to originate from a classical spherical fireball. In this sense the rapid decline clearly follows t^{-p} (Sari et al., 1999).

The decay slope further explored

In order to understand the evolution of the decay component, the relationships between the observed slopes and p, the spectral index of the injected electron energy distribution, are usually considered. This parameter directly depends on the microphysical parameters $\epsilon_{\rm e}$ and $\epsilon_{\rm B}$ and the bulk Lorentz factor (γ) as described in Chapter 1. From direct measurables, we can place limits on this spectral index by scaling the slopes of the light curves. For GRBs, the value can be constrained to $1 < p \leq 3$, (Kumar & Zhang, 2015), with typical values of around $p \sim 2.5$ being relatively common (Wijers & Galama, 1999; Sari et al., 1999; Starling et al., 2008).

So in the context of a homogeneous medium ($k = 0$), the decay slope is expected to follow the scaling of $\frac{3(1-p)}{4}$ (Granot & Sari, 2002), such that $\alpha_2 = \frac{3(1-p)}{4}$. It is also worth noting that GRB decay slopes often follow the order close to or around unity, further supporting that our measured slope is steeper than usual for a spherical fireball. Thus given our value for $\alpha_2 = -3.81^{+1.35}_{-1.36}$, we find that $p = 6.1 \pm 2.7$. Applying the uncertainties (at 1σ), at best this implies that $p \sim 3.4$. If we consider an interpretation in terms of the afterglow emission interacting with a massive circumstellar wind ($k = 2$) where the decay slope scales as $\frac{(1-3p)}{4}$, we get $p = 5.4 \pm 2.7$, which implies $p \sim 2.7$ within uncertainty. Both of these scenarios give plausible values for the electron energy inject index within their large uncertainties, which still reinforce that our measured slope does not conform to a relativistic spherical fireball.

Invoking the evolution featuring a jet break, i.e t^{-p} (Sari et al., 1999; Mooley et al., 2018), such that $p = -\alpha_2$ is the strongest argument we can give. For a laterally expanding jet, this gives $p = 3.81^{-1.36}_{+1.35}$,

which suggests $p \sim 2.46$. We further suggest a jet break occurring during this time as coincident with the passage of the peak frequency across the observing band (see Granot (2007) for extensive review on jet breaks, and Wang et al. (2018) for examples). We do not provide any further calculations of the jet angular structure and dynamics, since that requires numerous theoretical assumptions beyond the scope of this project. We further elect not to draw any strong conclusions on the value of the spectral index of the injected electron energy distribution, p, estimated from our observations. Despite our estimates being reasonable within uncertainties, we concede that the uncertainty margins for the decay slope are quite significant, thus requiring caution with any interpretation. We submit that even though similar or even higher values have been measured or projected (Groot et al., 1998; Sari et al., 1999), MeerKAT observations of GRB190114C alone do not provide the most confident constraint on the electron distribution for this GRB at late times (see Mooley et al. (2018) as an elected example). An alternative would be to apply other modelling efforts, and perhaps with combined broadband data apart from our simplistic smoothly broken power law.

The late time emergence of the host galaxy component could also be the reason why the observed decay slope proves challenging to estimate accurately from these observations, since all estimates tend to favour large values beyond physical reason theoretically. We further point to combining all available broadband data to determine the full energetics of GRB190114C. Joining all existing γ-ray to radio data is probably a better approach to estimate all the relevant physical parameters for this first TeV burst. However, the extensive modelling that that requires is beyond the ambit of this dissertation, which aims to investigate the evolution of GRB190114C with MeerKAT at 1.28 GHz.

2.5.5 Host Galaxy Contribution

Before the eruption of GRB190114C in 14 January 2019, one of the MeerKAT LSP projects, MIGHTEE (Jarvis et al., 2016), had observed the direction of the field months prior (Tremou et al., 2019). We privately understand (through separate communication with Ian Heywood who processed the data at SARAO) that their observations taken on 12 April 2018 have been imaged and shown that the pre-burst flux density for the host was at the level of 74±15 μJy/beam at 1065.3 MHz. By assuming a synchrotron source of a spectral index $\alpha = -0.7$, the flux was extrapolated to correspond to 66±13 μJy/beam at MeerKAT's 1284 MHz central observing frequency. The observations were only imaged at the lower half of the observing band as the GRB host was not at the phase centre, and thus on the flank of the primary beam, adding uncertainty to the calculated flux. This is a typical consequence of under-estimating fluxes for sources away from the center of the primary beam. We accept this extrapolated value as consistent with our modelled host constraint of $G = 94^{+11}_{-13}$ μJy/beam within uncertainty. Given that we didn't have to do any pointing or primary beam corrections for our modelled value, we favour this one over the extrapolated host flux from the MIGHTEE observations. Furthermore, our modelled value is consistent with fluxes observed at the end of the MeerKAT monitoring campaign. By this we posit that the last 3 observations were essentially dominated by the host galaxy component. This ultimately means we observed the afterglow of GRB190114C from its rise in the lower radio frequencies, up until it quenched and moved across our observing band as the host started to dominate the emission. We point to observations and analysis with HST, VLT, and ALMA by de Ugarte Postigo et al. (2020) for additional details regarding the spectroscopy and photometry of the host of GRB190114C. They show evidence that the event occurred near the galactic nucleus of a host that is part of a close interacting pair of galaxies.

2.6 Results: Interstellar Scintillation Parameters

We noted clear modulations in flux throughout the MeerKAT light curve and interpret this as persistent interstellar scintillation. Interstellar scintillation (ISS), which has been described in extensive detail by Rickett (1986); Narayan (1992); Goodman (1997); Walker (1998) is a phenomenon that occurs when radio waves propagating from a point source experience distortions due to our charged interstellar medium (ISM) that has a variable electron density distribution. These inhomogeneities in the ISM cause the observed patterns of irregularities or scatter in flux on an observed light curve of a compact radio source. There are two versions of this phenomenon, namely weak and strong scattering (Walker, 1998). Weak scattering occurs due to small fluctuations in the electron density between the observer and the source, with changes typically occurring within the first Fresnel zone (a prolate ellispoid around the line of sight between observer and target) (Granot & van der Horst, 2014). Strong scattering occurs when variations occur on scales smaller than the first Fresnel zone, resulting in severe modulations in flux. Strong scattering is further separated into two; namely refractive and diffractive scintillation respectively. Refractive scintillation is long-lasting (days to months) and broadband (Rickett, 1986), being observed at various frequencies. Diffractive scintillation or scattering, in contrast, is short term (minutes to hours) and causes modulation in narrow frequency bands.

The theoretical framework shows that ISS is strongly frequency dependent. Modest modulations (weak ISS) are expected at higher radio frequencies, while lower frequencies exhibit strong ISS effects. By taking the standard case assuming that ISS occurs at some thin screen at a distance d_{scr}, we can define the scattering strength ξ, a dimensionless parameter, as given by Walker (1998, 2001):

$$\xi = 7.9 \times 10^3 SM^{0.6} d_{scr}^{0.5} \nu_{obs}^{-0.7}, \tag{2.2}$$

where SM is the scattering measure and ν_{obs} denotes the observing frequency. The transition frequency between weak and strong scattering is then defined as (Goodman, 1997):

$$\nu_{trans} = 10.4 (SM_{-3.5})^{6/17} d_{scr}^{5/17} \text{ GHz}, \tag{2.3}$$

where $SM_{-3.5} = (SM/10^{-3.5} m^{-20/3})$ kpc. This equation states that for $\nu_{obs} < \nu_{trans}$ strong scattering persists, and for $\nu_{trans} < \nu_{obs}$, weak scattering persists. There are modulation indices and angular scales associated with ISS, and these are very useful in that they can help constrain the angular size of the source as its afterglow expands over time. This comes as the angular size of the jet starts out smaller than the angular scintillation scales, and expands over time until it surpasses these scales, after which variations in flux diminish. The angular scales are expressed in terms of the Fresnel angle θ_{F0}:

$$\theta_{F0} = 6.3 \times 10^4 SM^{0.6} \nu_{trans}^{-2.2} \ \mu\text{as} \tag{2.4}$$

For our analysis, we estimate the ν_{trans} and SM through a dedicated FORTRAN model code for the free electron distribution in the Milky Way Galaxy, the NE2001 model (Cordes & Lazio, 2002). The parameters depend on the sky location of the target, so we feed the model the galactic coordinates of GRB190114C as follows; $l = 222.47°$ and $b = -53.08°$, respectively. We apply a distance of $d_{scr} = 100$ kpc, just edging our galactic halo. The distance is converted to a dispersion measure DM by the code, from which consequently the scintillation parameters are calculated. The model yields $\nu_{trans} = 8.14$ GHz, and $SM = 0.1790 \times 10^{-3}$ kpc. We clearly see from this result that our observing frequency, $\nu_{obs} = 1.28$ GHz, is less than the measured transition frequency, $\nu_{trans} = 8.14$ GHz. This means we are in the strong scattering regime, so either refractive, or diffractive scintillation is at play.

2.6.1 Refractive Scattering

By inspection, the observed fluctuations in flux for GRB190114C are long-lasting as seen from the MeerKAT light curve, also seen in the uGMRT data around the same times Misra et al. (2021), see Figure 2.12. We interpret this as refractive scintillation dominating the emission. To test this argument, we determine the

above mentioned angular scales and modulation indices for our results using equations defined by Walker (1998) and further outlined in a review by Granot & van der Horst (2014). We calculate the scales as follows:

The duration of refractive scattering t_{refr}:

$$t_{refr} = 2\left(\frac{\nu_{trans}}{\nu_{obs}}\right)^{11/5} \tag{2.5}$$

gives $t_{refr} = 116.29$ hours. This translates to 4.8 days. The refractive modulation index:

$$m_{refr} = \left(\frac{\nu_{obs}}{\nu_{trans}}\right)^{17/30} \tag{2.6}$$

is $m_{refr} = 0.3511$, which translates to 35.1% in flux modulations. Taking the modulation index and the duration, we conclude that refractive scattering occurs in the order of 4 to 5 days, within which the flux modulations vary at a rate of about 35%. This effect is especially severe at 7.84 days post burst, i.e 22 January 2019. We show this effect in our fitted light curve (see dashed lines in Figure 2.8) for comparison with the observed fluxes:

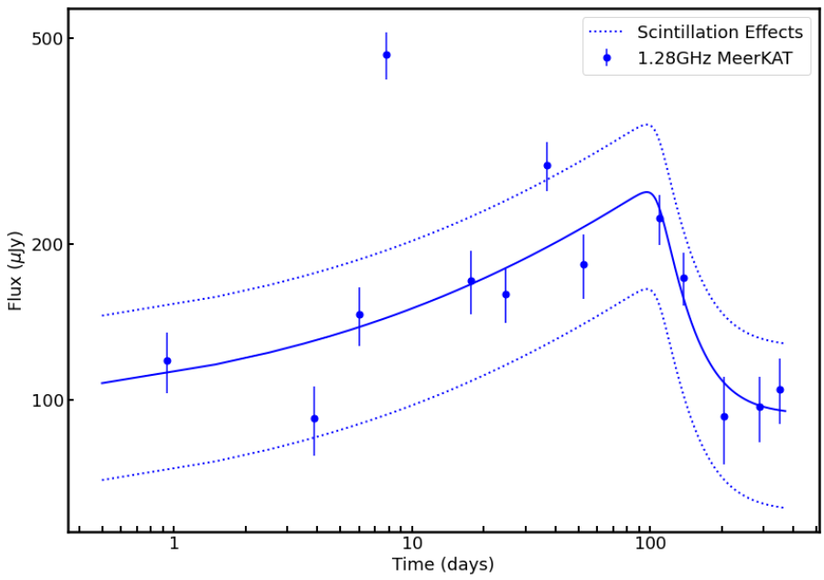

Figure 2.8: The fitted MeerKAT light curve, with the dashed lines detailing the scintillation effects. The flux modulation is at a rate of 35% at nearly 5 day scales.

Refractive angle and source size estimation

For the Fresnel angle:

$$\theta_{F0} = 6.3 \times 10^4 SM^{0.6} \nu_{trans}^{-2.2}\ \mu\text{as} \tag{2.7}$$

we get $\theta_{F0} = 3.529\ \mu$as. We use this to calculate the refractive angle:

$$\theta_{refr} = \theta_{F0}\left(\frac{\nu_{trans}}{\nu_{obs}}\right)^{11/5} \tag{2.8}$$

which yields:

$$\theta_{refr} = 205.215\ \mu\text{as} \tag{2.9}$$

We can use this refractive angle to constrain the source size (θ_s) during the refractive scintillation. We use the online cosmology calculator to estimate the source scale (Wright, 2006). By assuming a flat cosmology of $H_0 = 69.6$, $\Omega_M = 0.286$, $\Omega_{vac} = 0.714$, and our given redshift $z = 0.4245$ (Selsing et al., 2019; Castro-Tirado et al., 2019), we estimate the source scale to be 5.623 kpc/arcsec. The product of this source scale and the measured $\theta_{refr} = 205.215$ μas results in a physical size corresponding to $\theta_s = 3.6 \times 10^{18}$ cm.

We find that our calculated source size for GRB190114C is 2 magnitude orders larger than the source size of 4.0×10^{16} cm calculated for GRB130427A also using refractive effects (van der Horst et al., 2014). We further compare with various source size estimates for the evolution of GRB030329 achieved through VLBI observations since the GRB was close (z=0.1685) enough to resolve in the radio. Initial GRB030329 source sizes were calculated to be 6.17×10^{17}cm (0.2 pc) and 1.54×10^{18} cm (0.5 pc) at 25 and 83 days post burst respectively (Taylor et al., 2004; Granot et al., 2005). Further observations at 806 days showed GRB030329 to have expanded to 3.05×10^{18}cm (0.99 pc) (Pihlström et al., 2007). All these comparison values are below our estimated size for GRB190114C, which is also at a higher redshift than GRB030329. This suggests that the explosion reached high expansion rates compared to the well resolved GRB030329, further adding to the many interesting characteristics of this GRB.

Other previous GRBs for which source sizes have been calculated from scintillation parameters include GRB970508. For this GRB, the diffractive scintillation effects calculated by Frail et al. (1997) concluded on a source size of not more than 10^{17} cm. This is a single order of magnitude smaller than for GRB190114C as calculated by this work. Similarly, Chandra et al. (2008) obtained the upper limits for the fireball radius of GRB070125 to be about 2.4×10^{17} cm. The ATCA observations of GRB 210702A, showing a radio flare, and scintillation effects in the weak regime, resulted in a source size estimation of $\leq 6 \times 10^{16}$ cm (Anderson et al., 2023).

2.6.2 Diffractive Scattering

Diffractive scattering generally occurs at angular scales that are smaller than that of refractive scattering, which limits its effects to a narrow frequency band and over a short period of time. To this effect, intra-day flux modulations within individual observations are often seen for some GRBs at radio frequencies. If diffractive scattering affects our MeerKAT observations, we expect to see significant short time-scale variability within individual observations.

To test for diffractive scattering, we decisively split our 2.6 hour long observation of day 7.84 into 10 epochs. We selected this day as its full observation resulted in the highest flux spike compared to the cumulative 351 day light curve. We split this day's observation into ten epochs of 10 minutes each, with each epoch representing the individual scans of the GRB. We imaged these ten 10 minute epochs, extracted the GRB fluxes, and plotted a short time-scale variability light curve for the GRB during this observation run as shown in Figure 2.9. By inspection of this light curve, we see a rise and a plateau in flux. We do not see significant fluctuations in flux that are expected throughout the observation, with 9 out of the 10 epochs being well within 1σ. Furthermore, our calculation, $t_{diff} = 2\left(\frac{\nu_{obs}}{\nu_{trans}}\right) = 0.218$ hours, shows that if diffractive scattering is affecting our observations, it should occur at a timescale of at least 13 minutes. Since we do not record evidence of this at plotted 10 minute intervals (see Figure 2.9), we render diffractive scintillation negligible for the entirety of the observation. This suggests that the observed stable fluxes are likely characteristic of the GRB itself, and unaffected by diffractive scattering.

To test our conclusion, we calculated fluxes for 6 selected background sources at a similar flux level to the GRB to check for any behaviour of uncorrelated fluctuations. These fluxes are calculated from the same ten 10 minute epochs as shown in Figure 2.10. From plotting light curves for these sources we find that the background is generally dormant, with sources only slightly variable within their mean standard deviation (see Figure 2.10, grey shaded regions). The six light curves show uncorrelated variations within their mean fluxes, with source 1 being entirely invariable or flat throughout the observation (see top left Figure 2.10).

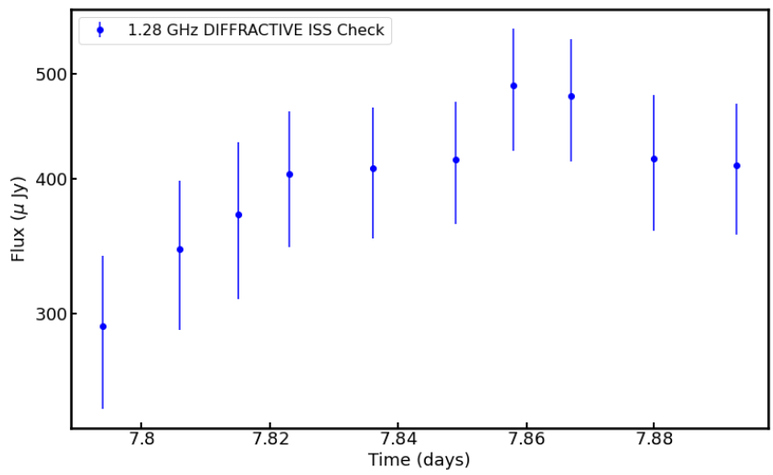

Figure 2.9: GRB light curve for day 7.84. We split the full 2.6 hour observation into 10 epoch scans of the GRB, imaged each scan and calculated the fluxes. The light curve shows a rise and a plateau in flux, without significant uncorrelated fluctuations throughout the observation.

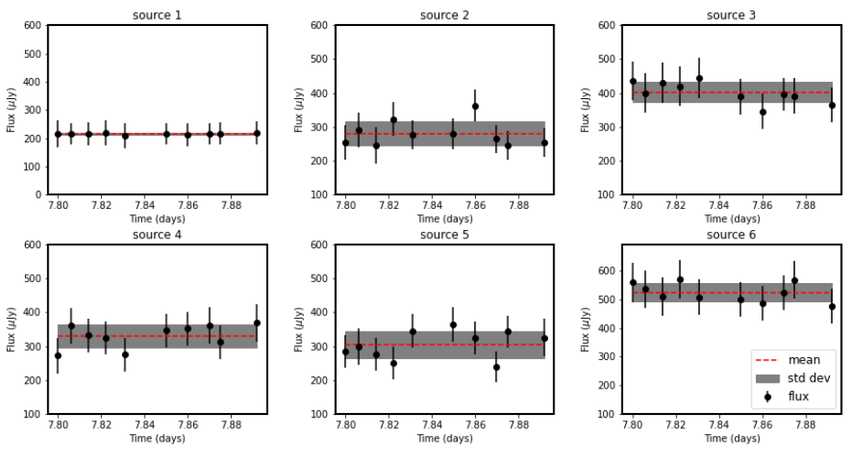

Figure 2.10: Flux modulation check for 6 selected background sources during the day 7.84 observation. Blacks indicate fluxes, red dashes show mean flux, and grey shaded regions indicate the 1σ deviation from mean observed flux per source.

2.7 Results: Radio Broadband Light curves of GRB190114C

In this section we combine the MeerKAT light curve data with the available broadband radio data. We start with a comprehensive L-band light curve using the 1.28 GHz MeerKAT data and the uGMRT 1.26 GHz data that was presented in Misra et al. (2021). We model this combined light curve using the same previous smoothly broken temporal power law with two slopes for a comprehensive L-band analysis. We then plot the full centimeter radio light curve encompassing MeerKAT, uGMRT, and ATCA data and discuss the behavioral trends.

2.7.1 MeerKAT-uGMRT light curve of GRB190114C

Detailed modelling of GRB190114C by Misra et al. (2021) with uGMRT data suggested that the microphysical parameters were variable in time, contrary to a common modelling assumption of fixing them in time. Similar results have previously been shown for GRB130427A (van der Horst et al., 2014). Here we combine the reported 1.26 GHz data with our 1.28 GHz data and model these as described. We neglect

the addition of a frequency term to the modelling, since there is essentially a narrow band difference of ~ 24 MHz between the two observing frequencies. The MeerKAT light curve is the most extensive of the two with 13 epochs spanning over 350 days, and uGMRT with 4 observations spanning almost 70 days. Combining the two light curves offers a best sampled L-band light curve of GRB190114C with 17 epochs.

Our modelling is summarised as follows; we utilise the MCMC fitting method described previously but with the priors $(0.0 < F_\nu(t_b) < 500)$, $(0.0 < \alpha_1 < 2.0)$, $(-3.0 < \alpha_2 < 0.0)$, $(20 < t_{break} < 140)$, and $(0.0 < G < 500)$. These priors indicate our fitting constraints for the 5 free parameters. We used 500 walkers with each taking 1000 steps. We burned-in the first 200 steps, resulting in 400 000 samples. The posterior distribution of the sample results is shown in Figure 2.11. The reported parameter estimates are quoted at the 50^{th} percentile, with the uncertainties at the 16^{th} and 84^{th} percentile, respectively. These are summarised in Table 2.4. The combined fitted light curve is then shown in Figure 2.12 and then interpreted accordingly.

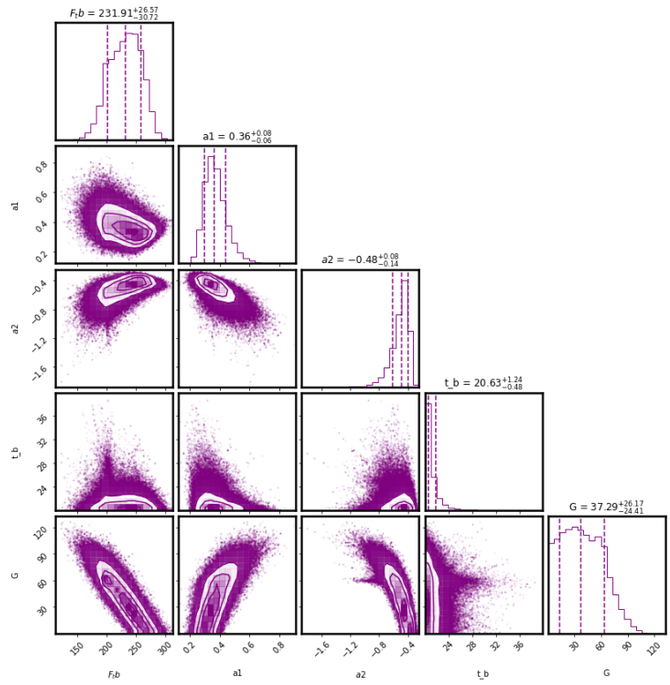

Figure 2.11: Sampling results from the EMCEE code for the MeerKAT-uGMRT fitting parameters.

$F_\nu(t_b)$	α_1	α_2	t_{break}	G
232^{+27}_{-31}	$0.4^{+0.1}_{-0.1}$	$0.5^{+0.1}_{-0.1}$	$21^{+1}_{-0.5}$	37^{+26}_{-24}

Table 2.4: Summary table for the MeerKAT-uGMRT fitting parameters.

The combined MeerKAT-uGMRT light curve (see Figure 2.12) is indicative of an early peak, with both the rise and decay being shallow. With this evidence, we interpret the light curve in the context of a forward shock propagating in a homogeneous medium, since our estimated rising slope of $\alpha_1 = 0.4 \pm 0.1$ is consistent with the theoretical formulation of $\text{F} \propto \text{t}^{\frac{1}{2}}$ (Granot & Sari, 2002). We also interpret this early break as the peak frequency moving through our observing band with the order $\nu_{\text{sa}} < \nu_{\text{m}} < \nu < \nu_{\text{c}}$ (Granot & Sari, 2002).

The decay component of the combined light curve is also shallow, even too shallow to invoke a jet break. We estimated a slope of $\alpha_1 = 0.5 \pm 0.1$ for this decay. Using this slope with the scaling of $\frac{3(1-p)}{4}$ in a homogeneous medium results in $p = 1.6 \pm 0.1$. We understand that $p < 2$ is indicative of hard electron energy distributions in particle acceleration, which can produce both synchrotron and Compton radiation effects (Eichler & Waxman, 2005; Resmi & Bhattacharya, 2008). In the context of GRB190114C, this

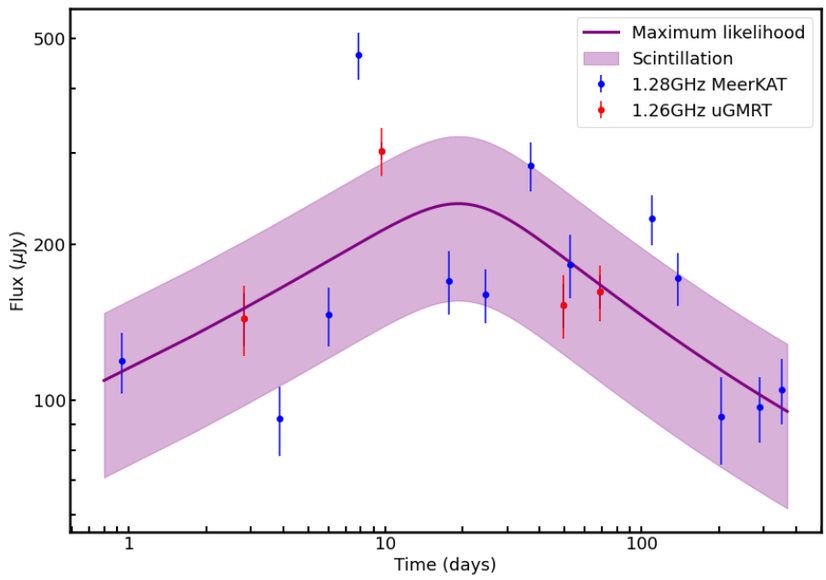

Figure 2.12: The combined MeerKAT-uGMRT L-band light curve of GRB190114C. MeerKAT data (blue dots) spans over 350 days, while uGMRT (red dots) spans close to 70 days. The data is fitted with a smoothly broken power law (purple line), and the shaded region indicates the 35% scintillation effects affecting these observing frequencies.

estimate may cast some light to how its observed TeV emission may have been produced. Incidentally, similar indices for this GRB have been separately calculated from extensive broadband modelling using a combination of MeerKAT, uGMRT and X-ray data from Swift in the context of both a homogeneous and wind medium (Aksulu et al. in preparation). This agreement in separate analysis gives additional confidence to the modelling and the estimates made.

From the combined modelling, the only parameter that appears to be not best sampled as shown in the posterior distribution (see Figure 2.11) is the breaking time t_{break}. we argue that this is likely caused by the fact that there is very significant scatter in the combined light curve, especially around the break. This then made it difficult to constrain the value better, despite the peak being clearly early from inspection of the combined light curve. The host galaxy contribution estimated from this, within uncertainties, is consistent with pre-burst MeerKAT data as presented.

2.7.2 ATCA observations and reductions

The Australia Telescope Compact Array (ATCA) first observed GRB190114C on 16 January 2019, almost 2 days postburst. As in the case with MeerKAT, early ATCA observations are also reported in (MAGIC Collaboration et al., 2019b), as well as other radio detections and contributing significantly to the early time broadband radio light curve of the GRB.

For this project, we coordinated MeerKAT and ATCA monitoring campaign schedules in order to acquire quasi-simultaneous radio broadband observations of the GRB. MeerKAT offered high sensitivity L-band observations at 1.28 GHz as shown in previous sections, while ATCA observed at higher frequencies. With its simultaneous multi-receiver observation strategy, ATCA observed the GRB at 5.5 GHz, 9 GHz, 17 GHz, 19 GHz, 43 GHz, and 45 GHz respectively. The observations were in continuum imaging mode and the receivers (4 cm, 15 mm, and 7 mm) each accorded 2 simultaneous 2 GHz bandwidth bands centred at stated the frequencies.

The ATCA data was reduced by ATCA staff, mainly Dr Gemma Anderson, who is a ThunderKAT col-

laborator based at ICRAR. She performed the data reduction following standard packages for ATCA. For all ATCA observations the phase calibrator was the ATCA catalogued calibrator 0237-233 (with R.A. 02:40:08.17, Dec. -23:09:15.7) to correct for time dependent effects. The flux calibrator was PKS B1934-638. The standard techniques for MIRIAD (Sault et al., 1995) and CASA (McMullin et al., 2007) were applied for the reductions. In particular, the fluxes were quantified in the image plane by force-fitting Gaussians at the GRB location, and inspecting for consistency with the visibility plane values. All reported figures are at 1σ Gaussian and rms errors. The results were originally shared with us for our quasi-simultaneous campaign, and were later also reported in (Misra et al., 2021).

2.7.3 Broadband Centimetre Light Curves of GRB190114C

Here we present the comprehensive centimeter light curves of GRB190114C obtained from our monitoring campain, reported uGMRT results, as well as our coordination with ATCA. The multi-frequency light curves show various trends in behaviour spanning 1-45 GHz. This expansive frequency range makes possible to study the full radio calorimetry of the GRB afterglow. We point the reader to the extensive modelling that has already been performed using uGMRT and ATCA data (Misra et al., 2021). For the sake of this project, we just assess and comment on the trends observed in the combined light curves.

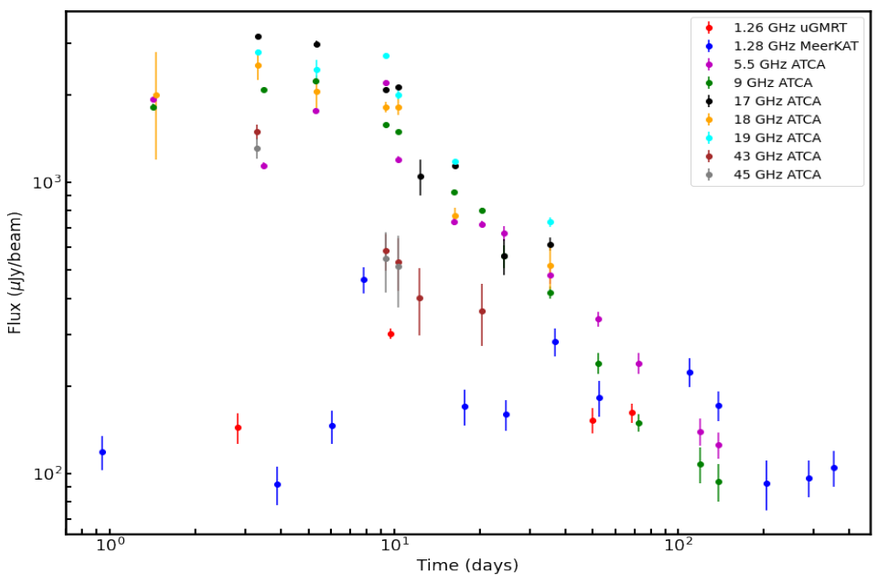

Figure 2.13: The multi-frequency light curves of GRB190114C using MeerKAT data, as well as data reported by Misra et al. (2021) for uGMRT and ATCA. The light curves span 1-45 GHz.

At the lowest frequencies, the combined MeerKAT (blue) and uGMRT (red) light curves indicate the GRB afterglow to be evolving quite slowly for the first 3-4 days. The sudden rise in flux is then characterised by scintillation effects, which seem to establish a pattern of fluctuations in the two light curves until the end of the uGMRT campaign close to 70 days. The GRB remained radio visible to MeerKAT for far longer up to 350 days, making the 1.28 GHz the highest sampled in time of all these radio light curves. The second most sampled (close to 140 days) light curves at 5.5 GHz (purple) and 9 GHz (green) also start off slow. While the 9 GHz is slowly rising in the first 10 days, the 5.5 GHz indicates scattering behaviour which has been attributed to scintillation (Misra et al., 2021). At around 10 days, the light curves also show a spike in flux behaviour similar to the lowest frequencies. In fact, this behaviour is observed in all these radio light curves from about 3 days postburst to just over 10 days. From the scintillation section (Section 2.6), we showed that the MeerKAT light curve had strong scintillation of up to 35% flux fluctuations, and that this behaviour was refractive scattering, which is both long lasting and broadband. With the 50% flux variations reported for both the 5-9 GHz frequencies, we find some comfort in concluding that the broadband flux fluctuations around this period are likely purely due to strong interstellar scintillation.

The higher frequencies (17-45 GHz) are consistent with a shallow start, and dramatic decays around the same time as when the low frequencies spike up in flux. This trend is unexpected as higher frequency light curves of GRB afterglows generally follow a shallow decay, even with jet break effects or any host galaxy contributions. Detailed modelling by Misra et al. (2021) even suggested that this behaviour could not be explained by the standard fireball model.

2.8 Discussion

In this Chapter we have explored the MeerKAT monitoring campaign of GRB190114C, which was the first GRB to have been observed at TeV energies by the MAGIC telescopes. We described our observing strategy, as well as explained the necessary steps we took to reduce and image the data, and presented the resulting most sampled radio light curve of this GRB at 1.28 GHz. We fitted this light curve with a smoothly broken power law with two slopes and a break, and included an offset term to constrain the host galaxy component. We found that the evolution of GRB190114C at low frequencies followed a mostly shallow long rise, peaking at over 100 days, followed by a dramatic decay. We interpreted the data in the context of a forward shock permeating in a homogeneous ambient medium, given the shallow behaviour consistent with $F \propto t^{\frac{1}{2}}$. We interpreted the break as resulting from the passage of the peak frequency crossing the observing band, while crossing simultaneously with a jet break. While we explored a number of other ways to physically explain the decay component and still remained conservative in our conclusion, steep decay components of GRB radio afterglows at low frequencies are often characteristic of jet break behaviour. We compared our host galaxy component to pre-burst images that were obtained by MeerKAT months prior to the burst, and found consistency when considering the uncertainties in the values. We interpreted our modelled value as the most likely host flux since it is not affected by primary beam calibration errors. MeerKAT data was strongly affected by interstellar scintillation effects and we quantified these effects using a FORTRAN code that effectively described the electron distribution in our Galaxy to help constrain the relevant scintillation parameters. We found that the flux fluctuations were at 35%, at a timescale of 5 days. We then used the scintillation parameters to get upper limits on the source size, and found relative comparison with previous explosion sizes estimated for other GRBs in literature.

We then combined the MeerKAT data with the literature data from uGMRT and modelled a comprehensive L-band light curve. The light curve was indicative of both a shallow rise and decay, with an early peak characterised by significant scatter around the break. We also interpreted this result as the GRB evolving in a homogeneous medium due to the shallow rising slope. We interpreted the break as resulting from the peak frequency crossing the observing frequency during the first 20 days. The decay component was also shallow, and resulted in an electron injection energy index that was suggestive of a hard electron distribution. Since that effect is indicative of high electron energies and makes possible both synchrotron and compton radiation effects, we concluded it could contribute towards shedding light to how the TeV emission may have possibly originated. We also found that separate broadband analysis found similar values, giving our estimate some additional confidence. We finally combined the available MeerKAT, uGMRT, and ATCA data and analysed the observed trends in the comprehensive multi-frequency light curves. We found that the broadband light curves show similarities in behaviour around 7-10 days, and this needs to be extensively modelled in detail in later works.

Chapter 3

MeerKAT Commensal Transients Survey in the GRB190114C field

3.1 Introduction

Radio transients come in two ways, coherent and incoherent. Coherent transients are characterised by fast variability, thus they are typically investigated through extensive time series analysis from their beam formed data. Incoherent transients in contrast, are slow in variability, and are surveyed by comparative analysis of images of the same field from epoch to epoch (Fender & Bell, 2011; Fender et al., 2016). In this chapter we survey for potential image plane transients in the MeerKAT field images of GRB190114C obtained from the extensive monitoring campaign from Chapter 2. The nearly one year long campaign garnered high quality data sets, making possible an opportunity to search the field for slow image plane transients in the field of the very high energy GRB.

For a long time, transient surveys have been limited to high frequencies at optical and X-ray bands due to intrinsic wide fields of view (FoV) for observatories at these bands, enabling them to scan large portions of the sky in relatively short periods. Observations with radio telescopes would then be gathered to complement the primary optical or X-ray detections. This is especially true for the initial discoveries of gamma ray bursts, X-ray binaries, and many other transient phenomena. However, recent developments in radio interferometry have re-positioned radio telescopes into cutting edge instruments of large fields of view, excellent computing power, and essentially the capacity to survey for, and serendipitously discover radio transients. The MeerKAT telescope in this regard joins a suite of other Square Kilometre Array pathfinders in the pursuit of image plane transients.

There are dedicated image plane radio transient surveys at multiple observatories globally. Most notably, the Very Large Array Sky Survey (VLASS; Lacy et al. 2020), the Amsterdam-ASTRON Radio Transients Facility & Analysis Centre (Kuiack et al., 2019), the Murchison Widefield Array (MWA; Tingay et al. 2012), as well as the ASKAP Survey for Variables and Slow Transients (ASKAP VAST; Murphy et al. 2013), and likewise, ThunderKAT with MeerKAT in the Karoo area in South Africa (Fender et al., 2016). From these dedicated searches, a significantly small number of transients has been discovered so far compared to expectations. Only one transient candidate without clear counterparts at other wavelengths was discovered at LOFAR, which helped constrain transient surface density and transient rates at MHz frequencies (Carbone et al., 2016; Stewart et al., 2016). Similarly, Varghese et al. (2019) also discovered a transient without any definite counterparts. While no candidates were detected with the VLA from nearly 3000 pointings at daily cadence of about two months (Polisensky et al., 2016), efforts at the MWA have been able to find just one transient source, while also placing limits on transient surface density for low frequencies (147.5 MHz) at a 3 year timescale (Murphy et al., 2017).

Given the small population of image-plane discovered radio transients so far, the majority of this sample have mostly been associated with a number of aspects such as; imaging or rare artefacts (Bower et al.,

2007; Frail et al., 2012), generally intrinsic AGN activity or variability (Levinson et al., 2002; Bannister et al., 2011; Mooley et al., 2016; Russell et al., 2019), interstellar scintillation effects, radio flaring or other stellar activity of some form (Bannister et al., 2011; Varghese et al., 2019; Driessen et al., 2022a). Recent efforts at GHz frequencies are now revealing a larger population of transients.

The first two radio transients discovered with MeerKAT (1.28 GHz), both with optical counterparts, have been associated with stellar activity. The first, MKT J170456.2482100, was associated with a K-type sub-giant star system (Driessen et al., 2020), while the second was indicative of radio flaring of an M-Dwarf (Andersson et al., 2022). Incidentally, other image-plane discovered radio transients have been without any multi-wavelength counterparts, with the latest example being the highly polarised galactic center transient, ASKAP J173608.2–321635, discovered by Wang et al. (2021) with the ASKAP. Further surveys with MeerKAT continue to find variable AGNs, with variability attributed to scintillation effects (see Driessen et al. (2022b); Rowlinson et al. (2022) and Chastain et al (submitted)).

The aim here is to perform a blind survey for transients or highly variable sources on timescales of days, weeks to months, or approximately consistent with the duration of the MeerKAT observing campaign for GRB190114C. For this undertaking, and similar to Driessen et al. (2020), Andersson et al. (2022), Rowlinson et al. (2022), Driessen et al. (2022b), and Chastain et al (submitted), we utilise the LOFAR transients pipeline (TraP[1]; Swinbank et al. 2015), to search for and identify transient activity from the observations. The original pipeline, in summary, is outlined in the following sections, as well as how it was methodically applied to our MeerKAT observations.

3.2 The LOFAR Transtients Pipeline (TraP)

The TraP pipeline ingests all the images, performs relevant quality control measures to avoid imaging artefacts, calibration errors etc and rejects any images not meeting a strict quality criteria. It then identifies individual sources in the images, while keeping a database record of each source detected in each of the images. It then performs a variability assessment, analogous to comparing the images to check for source positions, user defined thresholds, and performs stringent measures to avoid false positives, all the while drafting a catalogue of all detected sources. These sources are given unique identifiers, with their positions, light curves, variability metrics and other statistics and metadata as outputs to a web front interface for further analysis.

3.2.1 Input Image Data

The first step in running the TraP pipeline is an input of images from which the search for transients and variable sources will be performed. The images are typically three dimensional, with two spatial dimensions and one frequency dimension. The images naturally need to conform to standard radio astronomy image standards (e.g image should be a .fits file etc). TraP has been designed to function independently of which telescope the data originates from, as long as the images conform to radio imaging standards as described in Swinbank et al. (2015). A record of these images is logged and kept in a database where they are sorted into data sets for single jobs.

3.2.2 Quality Control

After the images are loaded onto the TraP, a rigorous series of quality control measures is initiated to deal with any imaging or calibration errors that may possibly lead to false positive detections in the following steps of the pipeline. The quality control algorithm inspects the noise levels in the images. Images where the background noise profile is significantly below or above pre-determined minimum and maximum rms values may be rejected from the process. This is indicative of calibration errors in the images, or even the observation itself. This is then followed by an assessment of how the restoring beam was sampled in the images. Incorrect sampling will result in high noise levels, and thus detection of artefacts and spurious sources. Likewise, the restoring beam shape is also assessed, which is telescope dependent, and directly influences the final images being used for TraP. Finally, quality control investigates proximity of the image

[1] LOFAR Transients Pipeline (TraP)

field to bright sources. TraP rejects images where the pointing directions or the target field is in close proximity with extremely radio bright sources. The threshold for the angular separation for this is user defined. Thus in essence quality control executes three tests; check image noise levels, assess restoring and primary beam sampling, and field proximity to bright background sources.

3.2.3 Source Detection and Measurement

The pipeline algorithm performs source detection through a series of iterative processes. Initially, the images are divided into grids to understand the background noise characteristics. Dimensions of the grid are taken such that they are larger than extended sources seen in the image, but also small enough such that any background variation may be traced (Swinbank et al., 2015). The background and rms in each individual grid are then estimated through iterative clipping close to the median to reject source pixels. It is assumed that independent pixels without sources follow a normal distribution, while the ones with source contamination do not. Thus pixels falling at some factor ("n") of the standard deviation of the distribution are rejected. The rejection factor is chosen such that half of the normally distributed pixels are rejected. After the iterative clipping, the background of a crowded field will be defined as equal to the median, or otherwise as a subtraction of a factored mean from the median.

The modelled background profile is subtracted from the original input images. The noise profile is multiplied by some constant factor to define the threshold for source finding. This factor is user defined. Sources are then identified if the background subtraction from the input image is larger than the detection threshold. The detection of sources in this process is significantly thorough, and ensures that pixels falsely identified as sources are as few as possible. Following this is then a process of deblending, where contiguous source islands are checked to see if they contain individual or multiple sources. Beyond this, the individual source parameters such as position and flux may then be estimated from the pixel islands, and then finally fitted with elliptical Gaussians for uncertainty estimations and corrections before being fed to the database as final parameters.

3.2.4 Source Association

From the previous steps, each source detected in a series of images is given a unique individual identifier. A running catalogue is formulated and all detected sources are entered. This catalogue encompasses the source position (RA and Dec), fluxes, variability metrics, and all associated uncertainties in each of these parameters. All these measurements ultimately culminate in the light curve of the source. The association procedure then searches for counterparts in the running catalogue, and heavily relies on source position in the sky, specifically the de Ruiter radius, which is defined as a dimensionless comparison between any two possibly associated sources. Sources identified as truly associated will have their positional differences being likely due to just measurement errors. Various association types are possible, such as; no association, one to one, many to one, one to many, and many to many (Swinbank et al., 2015). These distinguish how running catalogue sources may be associated. 'No associations' are for sources that cannot be unambiguously matched or associated with any extracted source in the running catalogue. 'One to one' are for when a single measurement can be associated with one source. 'Many to one', and 'one to many' are reverses of each other in that either many running catalogue sources satisfy association criterion with one source, or in the converse, where one source suffices association with many running catalogue sources. Finally, 'many to many' are for multiple running catalogue sources that may be associated with multiple extracted sources, with every combination yielding a light curve, and adding significant complexity to the output database. This is mitigated by reducing 'many to many' associations into 'one to many' or 'many to one', using only source pairs with the least de Ruiter separation. Sources that are not detected in the images, but are expected to be detected by the source finding procedure in the field since they are above the detection threshold, are recorded as null-detections. A record of sources in the field is kept, which includes sources in the running catalog of known sources, and sources that were not associated with any sources in the running catalog. With the latest and previously improved versions of the TraP, forced fitting is attempted at locations where sources are expected in the field but are undetected in the images.

3.2.5 Source Properties

For ease of analysis and tracking, already known sources in the field may have their positions recorded on a custom monitoring list. These are, for example, the main target of the field from which transients are being searched. Typically, sources in the monitoring list should be detected by the pipeline, and in any case they are not, forced fits flux estimations are made at the provided positions. Monitoring lists can also be created for the re-analysis of potential candidates, or a recalculation of their properties. The properties of each source are taken as an aggregate of all the detections of the individual source from each image, where the measurements are combined to get the best approximation of the true source properties. The estimations are in the form of an arithmetic and weighted mean in each source property, such as the source RA and Dec, peak flux density and integrated flux density at any given frequency band.

3.2.6 Data Products

The final steps of the pipeline are the final outputs. From these, transient events are identified, as well as variable sources. Sources that cannot be associated with any previously catalogued source are recorded and denoted as new detections. Even when regarded as new detections, it is possible that previous observations of the source position may not have been deep enough to detect these new sources, and TraP can distinguish these by a sensitivity check on all the images. TraP can keep track and can compare the flux density and sensitivity of all ingested images, and can accurately discern from the sensitivity at each source position if the new detection could have been previously detected. Variable sources are identified through the significance of their variability metrics. The parameters are η and V, denoting the coefficient of variation in flux, variability significance, and the probability of variability respectively. TraP calculates all of these metrics for each and every source detected. We shall define and elaborate further on these parameters in later sections as applied for our survey, and to bring their essence into context.

3.3 Method: Running the "ThunderTraP"

For the purpose of this chapter, and the scope of this thesis, we implement an epoch to epoch approach for this survey using our MeerKAT images of the GRB190114C field. While a more extensive approach of making short time images could offer even better results for fast transients in the image plane (say 8 seconds at lowest for fast transients), that approach is resource intensive in terms of computing, and is a potential future endeavour with the full available data for the field. Initial test runs of the TraP pipeline showed that our images were immediately rejected by the pipeline's quality control measures. This was a result of the images being over-sampled at 30 000 sampling iterations at pixel sizes of 1.5 arcsec across. Alternatively, since the first 11 epochs spanning 204 days were available, and all of them reduced and imaged in the manner outlined in MAGIC Collaboration et al. (2019b) with direction-dependent calibrations, we used only those images instead to carry out the transients survey.

3.3.1 Pipeline set-up and execution

A PostgreSQL database for IDIA has been created for transients research. Users have access through a username and password for the database, and an individual web interface for viewing results. This arrangement is often called the "ThunderTraP". We began the survey process by creating a working directory with all the relevant TraP scripts for setting up. We edited the environment variables in the trapenvvar.bash script, which allows access to the database, and then initialised the project for which the survey will be done. This created a project directory with additional pipeline scripts. In these scripts, the pipeline.cfg was checked to ensure that copy_images = False to avoid copying images to the disc, which may lead to storage related errors. We then edited the images_to_process.py script to specify the locations and names of all the chosen field images. In the job_params.cfg script, we maintained the default TraP parameters. These are a default detection_threshold = 8σ, with an analysis_threshold = 3σ, where σ is the background noise level. We set the extraction_radius_pix =4060 as the search radius to coincide with just less than half the image size. This helps avoid searching image edges for transients, which are often prone to artefacts and false positives since sources far from the primary beam center generally have their fluxes

underestimated. We utilised a deblend_nthresh =10 to separate individual sources that may be in very close proximity to other sources, and set beam_widths_limit =1.0 to restrict the spacial source association. We finally maintained new_source_sigma_margin = 3 to only retrieve candidates at a 3σ confidence level. After all this set-up, we started submitting or running jobs and tracking outputs. Our TraP runs were successful, with our last executed job (still using the default TraP parameters set above) yielding 1648 running catalogs, and 537 new sources. From these results, we started a light curve and variability analysis.

3.3.2 TraP Outputs and Variability Analysis: η vs V

TraP calculates fluxes for each and every individual source detected and outputs a light curve. With every light curve, each source's variability metrics are also calculated in the form of statistics η and V (Swinbank et al., 2015). Here, η is defined as the reduced χ^2 value when compared to a stable source, where higher η values indicate significant variation from a constant flux density, and lower η values show that the source flux is stable. Sources with constant fluxes typically have $\eta \approx 1$. The other variability metric, V, is a flux density coefficient of variation, or "modulation index", and is a ratio of the sample standard deviation in the flux density to the mean flux density. Sources with high V will be characterised by larger variations in flux densities in their light curves. Sources with a combination of both high η and V values are likely to be identified as potential variable or transient candidates. The relation between these two parameters can be plotted in an η vs V plot to inspect for potential outliers to be identified as either transient or variable candidates from the full population of field sources detected by the TraP.

From our TraP runs, our variability analysis showed outliers in both η and V at a 1σ level as shown by the black dashed lines in Figure 3.1. Visual inspection of these sources in the images as well as their light curves, indicated that these were were in fact spurious artefacts and extended sources read out as new sources. From the η and V plot (Figure 3.1), even GRB190114C, the field target transient used as a monitor, is shown as relatively ordinary in variability compared to these sources. This presented a problem in the identification of potential candidates, resulting in the need to refine the results and use some source filtering alternatives, and define a selection criteria for the best potential candidates. For this purpose, we employ a "deduplication" procedure, and this is explained in great detail in the next section.

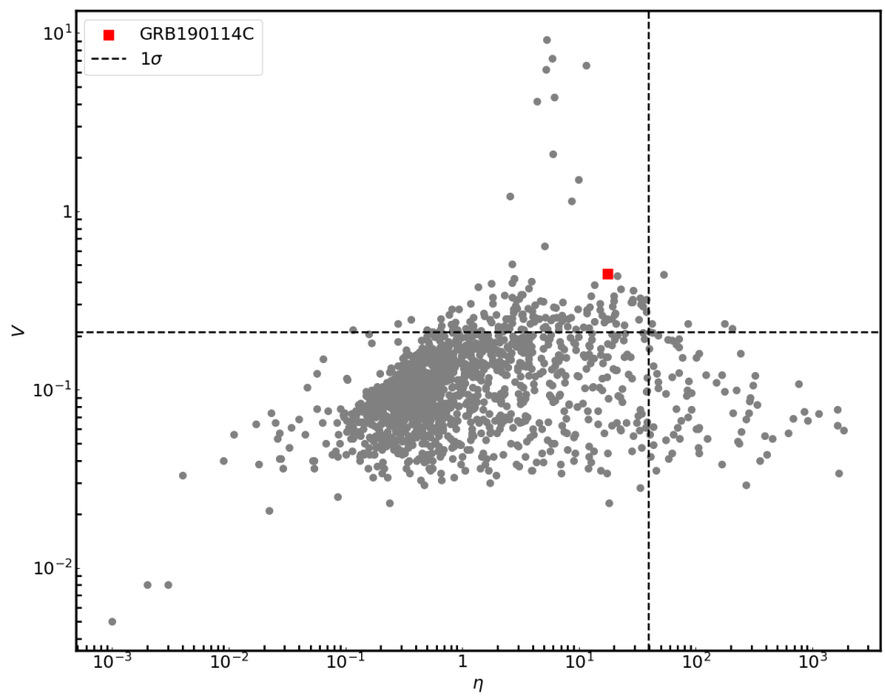

Figure 3.1: The variability parameter analysis of all the detected sources in the field. The black dashed lines indicate a 1σ level in both both η and V. The main target of the field, GRB190114C, is shown in red.

3.3.3 Deduplication and Candidate Selection

We perform a deduplication procedure to filter out very bright artefact sources from the TraP results in order to have a refined sample of sources to search for transients. We created a virtual environment and installed all relevant dependencies to run the code by Chastain et al (submitted), which is achieved by executing a FindOutliers.py[2] script. The script performs the following arguments (most of them in parallel):

- Access the web interface where the TraP result tables are stored. Permission is required.
- Inputs the dataset ID for a user specified TraP job. After this, all the TraP results, running catalogues etc will be ingested for analysis.
- Stores all the individual source IDs, calculates the minimum and maximum RMS profiles across all the images as well as the top and bottom values in η and V, and sets up angular separations for each source from the image center. These are then used to filter out sources accordingly.
- Executes a –deduplicate command to remove or reject sources that are "n" beamwidths from a bright source. The default set-up is –beamwidths = 5.
- Writes out an exclusions file for all the eliminated sources. In our case 73 sources were rejected.
- Writes out a variability parameters table in the form of a .csv file
- Creates animations of all the interesting sources.

After performing the deduplication procedure, we then manually inspected all the individual output animations of the top 40 interesting sources, where 20 are sources with highest η values, and the other 20 are those with highest V values. We tabulate these sources as indicated in Table 3.1. From this, we perform some manual vetting; with a set criteria to identify each source as either; point source, extended, spurious source, and if it is a potential candidate. From this criteria, every source that is not a stable point source

[2] github.com/dentalfloss1/sharedscripts/FindOutliers.py

is immediately rejected. From the 40 sources, 17 were rejected, leaving a sample of 23 sources. We then rerun the TraP pipeline with these sources set as monitors to get a refined indication of their variability parameters, as well as their full light curves. We set a rejection criteria of the form: if $\eta < 1$, not transient, if $1 < \eta < 2$, maybe transient, if $\eta > 2$, transient. From this, we reject all sources with $\eta < 1$ since η is a reduced χ^2 value for each source. This results in a sample of 12 potential transient candidates, but we exclude GRB190114C for a final sample of 11 candidates.

Source ID	RA & Dec (deg)	Point?	Extended?	Spurious?	η	V	η_{monitor}	V_{monitor}	Peak Flux (μJy)	Transient Variable?
SRC25966		No	Yes	Yes	845.23	0.075				
SRC25979		No	Yes	Yes	1686.58	0.034				
SRC25993		No	Yes	Yes	0.91	0.067				
SRC26016		Yes	Yes	Yes	618.96	0.057				
SRC26056		No	Yes	Yes	268.83	0.029				
SRC26088*	54.874, -26.665	Yes	No	No	309.45	0.11	320.61	0.14	3300 ± 13	Yes
SRC26115		Yes	No	Yes	356.52	0.040				
SRC26138		Yes	No	Yes	1138	0.073				
SRC26175		Yes	No	Yes	913.66	0.067				
SRC26261*	54.640, -26.535	Yes	No	No	763.24	0.11	618.09	0.099	5900 ± 12	Yes
SRC26340*	54.542, -26.636	Yes	No	No	5.06	0.64	4.28	0.63	136 ± 9	Yes
SRC26347*	54.538, -27.010	Yes	No	No	12.73	0.34	12.68	0.34	370 ± 11	Yes
SRC26381*	54.505, -26.946	Yes	No	No	21.23	0.43	14.77	0.42	318 ± 10	Yes
SRC26468		Yes	No	Yes	455.84	0.053				
SRC26606*	54.249, -26.764	Yes	No	No	37.66	0.27	22.43	0.29	539 ± 11	Yes
SRC26630		No	Yes	Yes	404.15	0.043				
SRC26637*	54.203, -27.238	Yes	No	No	336.55	0.082	332.66	0.095	4100 ± 11	Yes
SRC26678	54.151, -27.079	Yes	No	No	2.28	0.34	1.65	0.37	102 ± 10	Maybe
SRC26747		No	Yes	Yes	1643.37	0.063				
SRC26782		Yes	No	Yes	687.85	0.069				
SRC26793		Yes	No	Yes	1856.21	0.059				
SRC26838		Yes	No	Yes	271.03	0.068				
SRC26843		Yes	No	Yes	1640.08	0.077				
SRC26925		Yes	No	Yes	287.74	0.086				
SRC26977*	55.483, -26.597	Yes	No	No	3.19	0.34	2.56	0.33	144 ± 10	Yes
SRC27019*	54.588, -26.893	Yes	No	No	3.06	0.32	2.68	0.32	150 ± 11	Yes
SRC27022	54.556, -26.510	Yes	No	No	1.17	0.30	0.50	0.24	84 ± 11	No
SRC27025	54.495, -26.711	Yes	No	No	1.78	0.39	0.71	0.28	106 ± 13	No
SRC27078*	53.770, -27.693	Yes	No	No	2.73	0.28	2.65	0.31	158 ± 11	Yes
SRC27165*	53.735, -27.185	Yes	No	No	3.72	0.37	3.01	0.32	167 ± 10	Yes
SRC27197	54.891, -26.901	Yes	No	No	2.68	0.51	1.60	0.40	106 ± 10	Maybe
SRC27243*	54.324, -27.491	Yes	No	No	4.94	0.31	4.55	0.39	190 ± 10	Yes
SRC27279	54.619, -27.609	Yes	No	No	2.66	0.40	1.64	0.39	121 ± 12	Maybe
SRC27283	54.044, -27.542	Yes	No	No	1.36	0.38	0.99	0.34	108 ± 13	No
SRC27305		Yes	Yes	Yes	292.98	0.089				
SRC27329	54.863, -27.674	Yes	No	No	0.81	0.28	0.40	0.21	77 ± 10	No
SRC27349	55.482, -27.331	Yes	No	No	2.69	0.33	1.41	0.32	112 ± 12	Maybe
SRC27350	55.134, -26.448	Yes	No	No	3.30	0.34	0.51	0.16	110 ± 12	No
SRC27378	55.526, -27.027	Yes	No	No	3.90	0.40	1.42	0.30	102 ± 10	Maybe
SRC27386	54.469, -27.054	Yes	No	No	2.77	0.42	0.34	0.19	81 ± 10	No

Table 3.1: TraP top 40 results candidate list after the deduplication procedure. These are 20 sources with highest η values, and 20 with highest V values. From here, 17 candidates are rejected by visual inspection of their animations, resulting in 23 potential sources (whose peak fluxes are quoted). The final candidates are denoted with an asterisk ($*$) next to their Source IDs, and are discussed in the following sections. We note the field target GRB190114C (SRC26381) also correctly denoted as a candidate.

3.4 Results

In this section, we present the final candidates and their associated variability analysis. We provide the full light curves, and further demonstrate the candidate variability with the images consistent with the light curve evolution. We search for multi-wavelength counterparts for each candidate using the available source catalogues from multiple ground and space observatories. We then assess the nature of each candidate by classification using a diagnostic radio-optical parameter space of known transients and variable sources.

3.4.1 Candidate η vs V parameters

The variability parameters for our candidates after deduplication are shown in Figure 3.2. The grey markers indicate all the detected background sources, while the transient and variable candidates are shown in different colours. The dashed vertical and horizontal lines indicate a 1σ statistic in both η and V, respectively, fitted with a log-normal probability distribution function. All the candidates have $\eta \geq 2$ values.

The field target, GRB190114C (SRC26381 in Table 3.1), is depicted with a red square, and has the third highest V value in the field and $\eta > 10$. This makes it clearly consistent with being a variable source, and helps to reassure the validity of our analysis. Candidate sources SRC26977, SRC27019, SRC27078, and SRC27165 have the lowest η values, making them intrinsically lower flux density level sources peaking below 200 μJy (see peak fluxes on Table 3.1), with high ratios between their maximum and minimum fluxes, and hence large V values as evident from Figure 3.2. Similarly, SRC26340, the faintest candidate, as well as similarly faint SRC27243, also exhibit this nature.

Candidates SRC26347 and SRC26606 have $\eta > 10$, at similar flux levels to GRB190114C, and are both brighter than the faintest candidates. The remaining candidates, SRC26088, SCR26637, and SRC26261, are the brightest in the sample and they collectively have the highest η values, at $\eta > 100$ each. In contrast to the faint sources, these sources are characterised by lower V values, and thus small ratios between their maximum and minimum flux densities. These candidates also have small uncertainties in their fluxes.

The distribution of potential candidates on the η vs V space is a subject of investigation as a method of identifying transients, see Rowlinson et al. (2019) for a discussion. Interesting candidates are often expected to be on the "top right" quadrant of the η vs V plot above some σ threshold in both parameters (Rowlinson et al., 2022). With that notion, only GRB190114C, and SRC26606 would be viable candidates in this list, but we see clearly variable and possibly transient behaviour from the candidates in this list as discussed in the following sections.

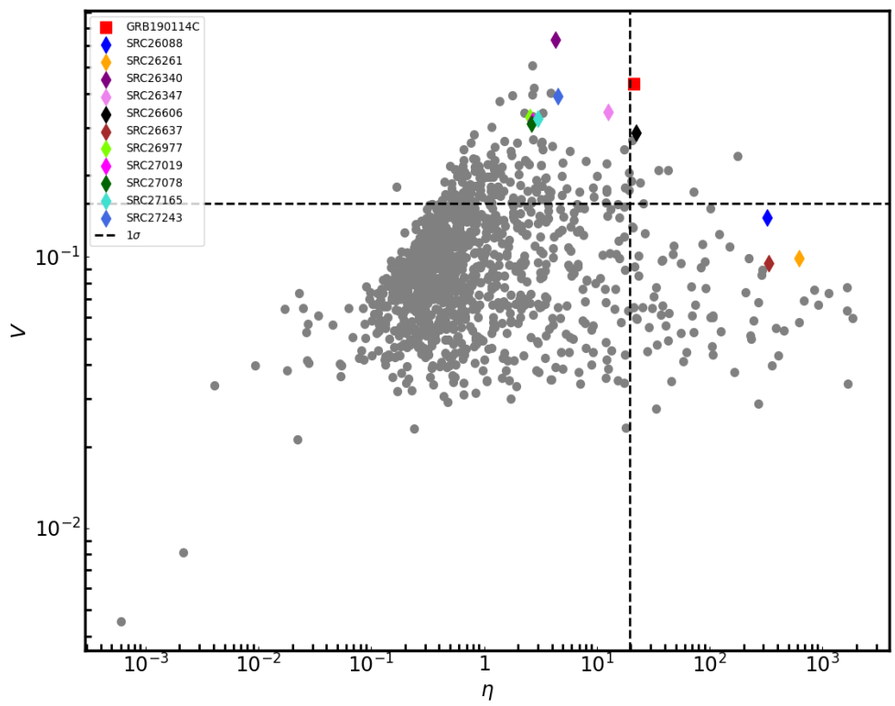

Figure 3.2: The variability metrics for the 11 candidates found after deduplication and further manual vetting. The main field target, GRB190114C is well established as a variable source (see red square). The grey markers indicate sources detected in the field. The dashed lines indicate 1σ levels in both parameters. All the candidates have $\eta \geq 2$.

3.4.2 Candidate Light curves

Here we present the light curves of the candidates identified from the survey (see Figure 3.3). These full light curves detail the fluxes and statistical uncertainties as calculated by the TraP. This being said, it is important to note that a systematic uncertainty from the telescope itself is not included (i.e recall a 10% systematic flux uncertainty added in quadrature to the MeerKAT light curves of GRB190114C in Chapter 2). Adding the systematic uncertainty has a direct influence on the calculations of the variability metrics, η and V, particularly the values of η, since it is dependent on the flux uncertainties. Should the systematic uncertainty be added, we expect the values of η to be lowered, with the highest values being the most significantly reduced. For the scope of this thesis, we do not take this approach in this work, and leave it for a later time should this chapter be converted into a journal article.

In Figure 3.3, we display the candidate light curves as calculated by the TraP pipeline and provide descriptions of the light curves. We use some part of the code[3] from Andersson et al. (2022) to create postage stamps that are 60 arcsec across for each candidate. We organise these stamps in chronological order following observation dates, and therefore each candidate's light curve evolution. These stamps are presented in the attached Appendix A. Together with the postage stamps, we also present the deepest catalogue optical snapshots of the candidate positions with the Dark Energy Survey[4] (DR2) (Abbott et al., 2021), shown on the same scale of 60 arcsec across. We generated animations for our candidates and the link to these is also supplied in the appendix.

Each light curve demonstrates clear variability in flux throughout the observations (see Figure 3.3). A visual inspection of all the light curves indicates generally uncorrelated behaviour from source to source,

[3] github.com/AnderssonAstro/MKT-J174641.0-321404-Paper-figs
[4] The Dark Energy survey

indicating satisfactory image quality, and a well behaved field. The candidate light curves are sampled in a quasi-logarithmic manner following the monitoring campaign strategy used for GRB190114C, since GRBs evolve as power-law functions of time. This strategy enables us to probe many timescales for variability, ranging from days, weeks, to months. The deep sampling of more than 2 hours per observation, of the field at these timescales avails an opportunity to uncover transient or variable behaviour, especially with MeerKAT sensitivity.

From the light curves (see Figure 3.3), SRC26088, SRC26261, and SRC26637 are the brightest candidates in the sample with lowest flux densities that are at least >2000 μJy. The light curves of these bright candidates show very small uncertainties in their fluxes, suggesting high intrinsic radio brightness. SRC26261 is the brightest candidate in the sample, with a light curve characterised by early rapid rises and declines in flux, almost like slow flickering, and being consistently above 5000 μJy during this time. The light curve then ultimately plateaus during the last three observations, even though still brighter than all other candidates in the list. Second Brightest is SRC26637, which has a light curve showing a rise in flux, with some fluctuations, and a late decline. SRC26088 is third brightest, also with significant early flux fluctuations within the first 10 days. The light curve reaches lowest flux around 50 days, and then continues to brighten, with a plateau beyond 150 days.

The faintest source in the sample is SRC26340, which has a highest flux of 136 ± 9 μJy, and has lowest fluxes that are just above the image noise. In fact, visually inspecting the postage stamps of the source in Figure A.3 shows that SRC26340 starts out bright, appearing and then disappearing several times throughout the observations. Other faint candidates showing this type of behaviour are SRC26977 (Figure A.7), SRC27019 (Figure A.8), SRC27078 (Figure A.9), and SRC27165 (Figure A.10), all of which show significant rises and declines in flux, and these are visually noticeable.

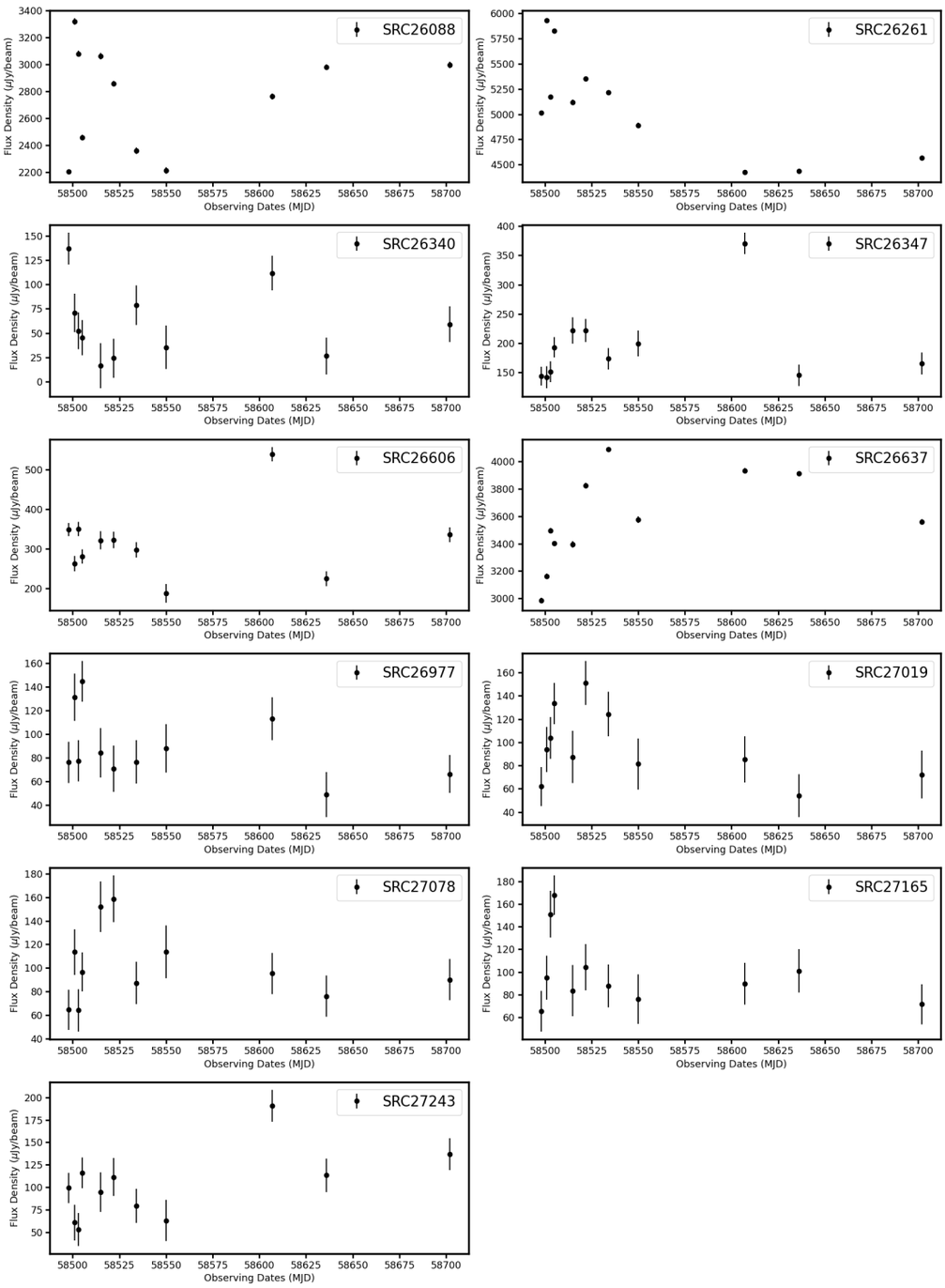

Figure 3.3: MeerKAT light curves of the 11 candidates obtained. Several of the light curves show sources being very bright at >2000 μJy, coupled with very small uncertainties in their fluxes. The fainter candidates appear to be at similar flux levels to the GRB studied in Chapter 2.

3.4.3 Counterpart Searching

After obtaining a final sample of potential candidate transients or variables, we employed a robust counterpart searching approach to cross-match our sources with the available archival broadband datasets. We queried catalogues in the optical, radio, X-ray, and infrared bands, see Table 3.2. In particular, we primarily used data from Pan-STARRS (DR2) (Flewelling et al., 2020), the NVSS 1.4 GHz (Condon et al., 1998), the VLASS 2-4 GHz (Gordon et al., 2021), *Swift* LXPS (Evans et al., 2023) and *WISE* (Wright et al., 2010), and supplemented these with other catalogues for further investigation, especially if initial searches show potentially interesting results. We looked at the Dark Energy Survey (DES DR2) optical catalogue for g,r, and i magnitudes of the associated counterparts (Abbott et al., 2021). This is the deepest optical catalogue for this part of the sky, see Table 3.3.

Tables 3.2 and 3.3 are cross referenced in this section and the next, for the classification of the counterparts. The NVSS (1.4 GHz) and VLASS (2-4 GHz) have resolutions of 45 arcsec and 2.5 acsec respectively. The NVSS catalogue has a detection limit of 2300 μJy for faint point sources, while VLASS has sensitivity of 120 μJy. We searched the catalogues with our candidate locations with a 1 arcsec search radius, and the results are shown in Table 3.2. We find that some of the catalogs cover our wide field, but have no detections, or others do not entirely cover the full field, or with nearest sources at several arcsecs or arcmins away. We provide some brief descriptions of the counterpart detections for each source.

Source ID	RA & Dec (h:m:s) Deg (°)	MeerKAT (μJy/Beam)	Pan-STARRS Peak Flux (μJy/Beam)	NVSS Catalog (μJy/Beam)	VLASS v2.17 at 1.4GHz (μJy/Beam)	LSXPS: *SWIFT* 2-4 GHz	*WISE* (INFRARED)
SRC26088	03:39:29.8, -26:39:52.2 (54.874°, -26.665°) ± (11.190", 10.000")	3300±13	PSO J054.8742-26.6644 89±1.5	(C0344M28) (ID 7600054874156303 7) (3.6 arcsec)	VLASS1QLCIR 3400±500 5308±122	3σ limit J033929.80-263951.2 (3 counts)	J033929.80-263951.7 1.8×10^{-2} s^{-1}
SRC26261	03:38:33.7, -26:32:06.3 (54.640°, -26.535°) ± (11.177", 10.000")	5900±12	PSO J054.6402-26.5350 No flux at location	(C0344M28) (ID 7615054640198825 9) (1.2 arcsec)	VLASS1QLCIR 6700±500 4125±120	3σ limit J033833.69-263205.4 (1 count)	No sources found 1.3×10^{-2} s^{-1}
SRC26340	03:38:10.1, -26:38:11.2 (54.542°, -26.636°) ± (11.191", 10.004")	136±9	No records found	Source Not Found	No Object Found	3σ limit (0 counts)	J033810.00-263812.1 0.11 s^{-1}
SRC26347	03:38:9.1, -27:00:35.1 (54.538°, -27.010°) ± (11.228", 10.003")	370±11	PSO J054.5380-27.0096 28 ±1	Source Not Found (ID 7558054537920874 2)	No Object Found	LSXPSJ033809.1-270033 (0.3—10 keV band)	J033809.10-270034.5 $3.8(+0.6, -0.5) \times 10^{-14}$) erg cm^{-2} s^{-1}
SRC26606	03:36:59.9, -26:45:49.6 (54.249°, -26.764°) ± (11.201, 10.001)	539±11	PSO J054.2496-26.7637	Source Not Found 40±1	No Object Found	Position Not Covered	J033659.94-264548.5
SRC26637	03:36:48.8, -27:14:15.2 (54.203°, -27.238°) ± (11.247, 10.000)	4100±11	No records found	Source Not Found	VLASS1QLCIR 4134±123	Position Not Covered J033648.82-271414.1	J033648.82-271414.6
SRC26977	03:41:55.9, -26:35: 49.2 (55.483°, -26.597°) ± (11.198, 10.013)	144±10	PSO J055.4829-26.5971 124±3	Source Not Found (ID 7608055482907380 0)	No Object Found	Position Not Covered	J034155.90-263549.5
SRC27019	03:38:21.0, -26:53:34.2 (54.588°, -26.893°) ± (11.233, 10.018)	150±11	No records found	Source Not Found	No Object Found	3σ limit (counts ?)	J033821.12-265334.2 2.6×10^{-4} s^{-1}
SRC27078	03:35:4.8, -27:41:34.8 (53.770°, -27.693°) ± (11.313, 10.017)	158± 11	PSO J053.7699-27.6930 27±1	Source Not Found (ID 7476053769890867 3)	VLASS1QLCIR 1399±131	Position Not Covered J033504.77-274134.2	J033504.79-274134.8
SRC27165	03:34:56.4, -27:11:05.8 (53.735°, -27.185°) ± (11.263, 10.019)	167±10	PSO J053.7351-27.1848	Source Not Found 588±6	No Object Found	Position Not Covered	J033456.41-271105.3
SRC27243	03:37:17.7, -27:29:29.4 (53.735°, -27.185°) ± (11.263, 10.019)	190±10	No records found	Source Not Found	No Object Found	Position Not Covered	No sources found

Table 3.2: Counterpart searching results for our final transient or variable candidate list. We queried optical, radio, X-ray and infrared catalogues with a 1 arcsec search radius to find possible counterparts. In case when a counterpart was found, we recorded the IDs and fluxes, or quoted the catalogue comment at source locations if otherwise.

SRC26088

We find several multi-wavelength counterparts for SRC26088 within a 1 arcsec radius of the MeerKAT position. The source coincides with a Pan-STARRS object PSO J054.8742-26.6644 in the optical bands. Further queries indicate that SRC26088 is also associated with a Gaia[5](DR3) source ID 5081643264101145984, which has a g-band mean magnitude of 19.99. This Gaia source has a proper motion (i.e angular velocity across the sky) of $\mu = (0.191 \pm 0.25, 0.0862 \pm 0.38)$mas yr^{-1} in RA and Dec, respectively. This suggests that the source may be too far in distance, and barely moving relative to the background, hence the significant uncertainties in the estimation of its proper motion. Deepest available photometry with the Dark Energy Survey (DES DR2) indicates that the candidate has been observed in the g,r,i bands by telescope, see row 1 of Table 3.3. We also find consistency between the Gaia and DES g-band magnitudes. The

[5]gaia archive/European Space Agency

nearest source detected with the NVSS (at 1.4 GHz) in the C0344M28 field, is 3.6 arcsec away from the MeerKAT position, but yields a flux density that is, within uncertainty, consistent our MeerKAT peak flux at 1.28 GHz. Our MeerKAT flux estimates have an uncertainty that is an order of magnitude smaller, likely due to the MeerKAT systematic uncertainty not being added. However, we cannot definitively associate SRC26088 with the NVSS source due to the noted disparity in their astrometry, so we rule it out as a radio counterpart. From the *Swift* LSXPS catalogue, we find that the position of the candidate was observed between 06-18 June 2019 without a detection, but a total band 3σ upper limit (see first row of Table 3.2).

SRC26261

This is the brightest MeerKAT candidate with a peak flux of 5900 ± 12 μJy. The source coincides with PSO J054.6402-26.5350 on Pan-STARRS, however no flux measurements are supplied in the catalogue. The image of the source with the DES (DR2) g,r,i bands show a faint point source in a fairly populated field across 1 arcmin, see bottom right of Figure A.2. The associated DES magnitudes are listed in Table 3.3, consistent with a faint optical source. In the radio bands, we find an NVSS source 1.2 arcsec from the MeerKAT position in the C0344M28 field. The NVSS flux density is consistent with our MeerKAT flux, with the MeerKAT measurement having a significantly smaller uncertainty (recall no systematic uncertainty added). Within positional uncertainty, we can associate the two radio sources. We also find a VLASS association with source VLASS1QLCIR J033833.69-263205.4 in the S-band (2-4 GHz) at 0.9 arcsec from the MeerKAT position. We do not find an Infrared counterpart for this source. We obtain a 3σ upper limit in the X-rays.

SRC26340

This is the faintest candidate source with a MeerKAT peak flux of 136 ± 9 μJy. We do not detect any radio counterparts for this candidate, since it lies at odds with the sensitivity and detection limits of both the NVSS (2300 μJy) and VLASS (120 μJy) catalogues. We do not find a Pan-STARRS association for the source. Deeper photometry of the source with DES(DR2) suggests a fainter counterpart at g=25.67 mag, see row 3 of Table 3.3, and bottom right of Figure A.3 for the optical image (60 arcsec across). We also find that the source coincides with a *WISE* object J033810.00-263812.1 in the infrared. We also obtain a 3σ upper limit in the X-rays with the *Swift* LSXPS.

SRC26347

This source is associated with an optical source PSO J054.5380-27.0096 in the Pan-STARRS (DR2) catalogue. It is also coincident with a Gaia (DR3) source ID 5081536890646601216, which has a proper motion of $\mu = (-1.075 \pm 0.54, 1.839 \pm 0.78)$mas yr^{-1} in RA and Dec. Within the Gaia catalogue, the source is flagged as variable, with a g-band mean magnitude of 20.56 mag, and a BP-RP colour of 0.76. The DES (DR2) photometry suggests a marginally fainter g-band magnitude, but both Gaia and DES (DR2) are consistent with a faint source in the g-band. We find a 3σ upper limit in the X-rays at the MeerKAT position, with the nearest *Swift* source, LSXPS J033809.1-270033, being at 1.99 arcsec away from our position. We rule this out as an X-ray counterpart for SRC26347.

SRC26606

Candidate SRC26606 is associated with source PSO J054.2496-26.7637, which has an optical flux of 40 ± 1 μJy, and source J033659.94-264548.5 with *WISE* in the infrared, see Table 3.2. SRC26606 is not detected within the Gaia catalogue, but the DES (DR2) photometry shows a faint source across the g,r,i bands, see row 5 of Table 3.3, and bottom right of Figure A.5 depicting a reddened point source. There are no detections with NVSS and VLASS at the MeerKAT position, considering their sensitivity limits, and this position is not covered with the *Swift* LSXPS.

SRC26637

This is one of the brightest candidates with MeerKAT (1.28 GHz) at a peak flux of 4100 ± 11 μJy. Quite surprisingly, we do not find any detection of this source from the NVSS catalogue at 1.4 GHz, even though

the position has been observed, and the candidate lies well above the NVSS detection limit (2300 μJy). We find an association with VLASS1QLCIR J033648.82-271414.1 on the VLASS (2-4 GHz) catalogue at 1.08 arcsec from the MeerKAT location, where it has a flux of 4134 ± 123 μJy. This flux level is consistent with the MeerKAT peak flux even though at different frequencies, and with MeerKAT having smaller uncertainties. We do not see any potential optical counterparts to SRC26637 after searching with Pan-STARRS (DR2) and Gaia(DR3). Additional optical searches with SkyMapper[6] also yield no results (Onken et al., 2019). However, DES (DR2) photometry suggests a significantly fainter source than ASAS-SN, with a g-band magnitude of 25.25±0.35 mag, see Table 3.3 for the other band magnitudes. The DES (DR2) g,r,i image of the source, bottom right of Figure A.6 does attest to a faint source in these optical bands.

SRC26977

The position of SRC26977 coincides with the Pan-STARRS source PSO J055.4829-26.5971, with an optical flux of 124 ± 3 μJy. We additionally find association with a Gaia (DR3) source ID 5081655603543991296, which is flagged as "variable". The Gaia source has a proper motion of $\mu = (0.233 \pm 0.19, -0.169 \pm 0.33)$ masyr^{-1} in the direction of the RA and Dec respectively, suggesting a potentially distant source. The source also has a Gaia g-band magnitude of 19.86 mag, which is in agreement with a slightly fainter DES (DR2) g-band magnitude of 20.175±0.004 mag, see Table 3.3. The DES g,r,i bands image of SRC26977 is presented in Figure A.7 (bottom right).

SRC27019

This is a relatively faint candidate with MeerKAT, peaking at 150 ± 11 μJy. We get an infrared counterpart association with source J033821.12-265334.2 from *WISE*, and a 3σ upper limit with *Swift* LSXPS. We get no association with any source on Pan-STARRS (DR2) or even Gaia (DR3). Comparison with DES (DR2) shows a significantly fainter source with a g-band magnitude of 26.02±0.66, which is barely visible in the image, see bottom right of Figure A.8.

SRC27078

Candidate SRC27078 is one of the fainter sources in this list. We find association with PSO J053.7699-27.6930 on the Pan-STARRS (DR2) catalogue. Searching the SIMBAD Database[7] reveals that there is a confirmed AGN at 1.1 arcsec of the MeerKAT position of SRC27078. This AGN is denoted J033504.75-274135.9 (Component number S662) in Norris et al. (2006) and has a flux density of 100 μJy between 0.75-1.5 GHz (no flux uncertainty supplied). Without a given uncertainty, this flux appears underestimated compared to the level with our MeerKAT peak flux, see Table 3.2. In the next section, we shall utilise the DES (DR2) deep photometry of SRC27078 from Table 3.3 and the MeerKAT peak flux, to assess if our classification of SRC277078 is consistent with being an AGN as evinced by Norris et al. (2006). See Figure A.9 bottom right for a DES g,r,i band image at the location of SRC27078, depicted as a reddened blob.

SRC27165

This candidate has the brightest optical counterpart in the sample from Pan-STARRS (DR2). It is coincident with PSO J053.7351-27.1848 in the catalogue, which has an optical flux of 588 ± 6 μJy. SRC27165 is also coincident with a Gaia (DR3) source ID 5081566027706999424. No proper motion or variability flag is supplied with Gaia for this source, but a g-band magnitude of 20.94 mag is provided. The Gaia magnitude is slightly fainter than the deeper and brighter DES (DR2) g-band magnitude of 18.743±0.004 mag. The DES association indeed shows a bright source at the MeerkAT position of SRC27165, see bottom right of Figure A.10. We also find association with an infrared counterpart J033456.41-271105.3 with *WISE*. There are no detections in the radio frequencies with NVSS and VLASS, even though the fields are in fact covered by both catalogues. *Swift* LSXPS does not cover the source position.

[6] SkyMapper's Southern Sky Survey

[7] SIMBAD Database- For astronomical source identifications and data catalogues

SRC27243

This faint MeerKAT candidate has no associated counterparts (within 1 arcsec) in several of the optical catalog surveys we queried, i.e Pan-STARRS (DR2), Gaia (DR3), and SkyMapper. There is no associated counterpart with the DES (DR2) catalogue with the position showing no source at the MeerKAT position (see bottom right of Figure A.11), but an r-band magnitude limit of ~ 25 mag is supplied. We shall use this limit in the next section to test for the classification of SRC27243. We also find that NVSS, VLASS and *WISE* cover the field but there are no detections, whereas *Swift* LSXPS does not cover the position.

Source ID	RA2000	DEC2000	gmag	rmag	imag
SRC26088	03:39:29.80	-26:39:51.78	19.899 ± 0.004	19.999 ± 0.005	19.904 ± 0.008
SRC26261	03:38:33.69	-26:32:05.98	23.518 ± 0.097	22.808 ± 0.066	22.206 ± 0.068
SRC26340	03:38:10.13	-26:38:10.28	25.67 ± 0.48	24.84 ± 0.29	23.96 ± 0.24
SRC26347	03:38:09.11	-27:00:34.64	21.171 ± 0.011	20.741 ± 0.010	20.432 ± 0.014
SRC26606	03:36:59.91	-26:45:49.36	22.953 ± 0.081	21.061 ± 0.019	20.335 ± 0.019
SRC26637	03:36:48.82	-27:14:14.85	25.25 ± 0.35	24.19 ± 0.17	23.76 ± 0.22
SRC26977	03:41:55.89	-26:35:49.48	20.175 ± 0.004	19.756 ± 0.004	19.645 ± 0.006
SRC27019	03:38:21.10	-26:53:33.84	26.02 ± 0.66	24.89 ± 0.31	24.04 ± 0.26
SRC27078	03:35:04.77	-27:41:34.90	23.155 ± 0.071	22.007 ± 0.032	21.080 ± 0.026
SRC27165	03:34:56.43	-27:11:05.27	18.743 ± 0.004	17.408 ± 0.002	16.954 ± 0.002
SRC27243				>25	

Table 3.3: The deepest photometric magnitudes available for our candidate positions with the Dark Energy Survey (DES DR2) (Abbott et al., 2021). We find no counterpart for SRC27243 from this survey.

3.4.4 Candidate Classification

To understand the nature of our candidate sources, a method to unravelling their properties is essential. To this end, we apply a diagnostic tool developed by Stewart et al. (2018). They investigate the relationship in the radio and optical flux densities of several classes of known radio transients and variable sources using extensive sets of available data. These transients and variables range from Galactic sources such as stellar events and X-ray binaries, or extragalactic events such as GRBs, Quasars and most supernovae. The authors mainly used a sample of brightest radio fluxes from 1-10 GHz for the population classes, and fluxes in the v,r bands in the optical.

For our candidates we use the F_o *vs* F_r[8] diagnostic plot of the radio-optical parameter space from Stewart et al. (2018) to compare our candidates to populations of other known variable or transient sources. We

[8] https://github.com/4pisky/radio-optical-transients-plot

couple the MeerKAT peak radio fluxes of the candidates (from Table 3.2) with the r-band magnitudes obtained for the sources from the DES (DR2) catalogue as shown in Table 3.3, and consistent with the approach taken in Stewart et al. (2018). The r-band magnitudes from the DES (DR2) are in the optical AB magnitude system.

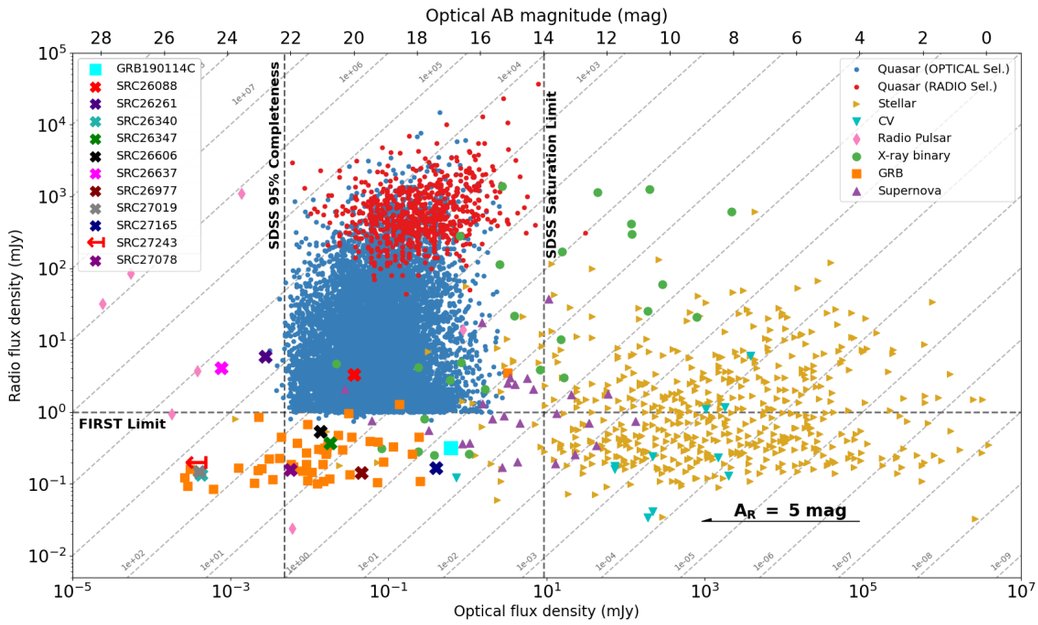

Figure 3.4: The radio vs optical flux plot for different types of transient or variable classes. We utilise this to classify our candidates (top left legend) by inspecting their placements on the parameter space. GRB190114C is used as a reference, and is correctly located as a very bright GRB. Adapted from Stewart et al. (2018).

From the radio-optical parameter space, i.e Figure 3.4, the dotted horizontal line indicates the detection threshold of 1 mJy for the FIRST[9] survey used for the sample population. The vertical lines indicate the 95% SDSS[10] completeness limit, as well as a saturation limit of 14 mag. The grey diagonal lines indicate constant ratios between the radio and optical fluxes, and correspond to changing distance. The arrow on the bottom right accounts for possible extinction effects in the optical magnitudes.

For our known transient in the field, GRB190114C, we pair the highest MeerKAT flux with the brightest available optical magnitude in the r-band. The MeerKAT flux calculated by the TraP pipeline is 318±10 μJy. The brightest available optical magnitude is from the Nordic Optical Telescope (NOT), which calculated an r-band magnitude of 16.93±0.02 mag, and the accepted redshift z=0.425 for GRB190114C, at 24 minutes post trigger (MAGIC Collaboration et al., 2019b). This flux and magnitude pairing results in the placement of GRB190114C in the GRB track of the radio-optical parameter space, with it being one of the few optically bright GRBs in this limited sample. It is essential to note that the main limitation of this pairing is that the used flux measurements are not quasi-simultaneously observed since the GRB is brightest in the radio bands much later than in the optical bands. Similarly, we discuss the placement of each candidate on the tracks of the radio-optical space.

SRC26088

From the classification, candidate SRC26088 falls within the Quasars track of the transient parameter space, see red "x". It lies consistent with a population of active galactic nuclei (AGNs) detected within the SDSS limits. Even based on the constant ratios in optical and radio fluxes where SRC26088 is positioned (see between diagonal grey dotted lines), we can conclude that it is very likely to be a quasar given the large population of quasars in this region.

[9] The Faint Images of the Radio Sky at Twenty-Centimeters with the VLA
[10] The Sloan Digital Sky Survey

SRC26261

This candidate lies just beyond the SDSS 95% completeness limit, where still some AGNs have been detected in the optical bands. Looking at the radio-optical flux ratios, SRC26261 is still best explained as an AGN that is fainter than those sampled by the SDSS. Within this track, a very small sample of radio pulsars has been observed. So we conclude that SRC26261 is likely an AGN.

SRC26340

This candidate, the faintest in our sample, lies well below the FIRST detection limit. It also lies beyond the SDSS completeness limit. This comes as the source is very faint in both the radio and optical bands. The candidate lies within the GRB track where also, a very significant population of AGNs, some X-ray binaries and stellar events have been shown to exist with the given radio-optical flux ratios. Deeper photometry could improve or solidify the classification as a fainter AGN beyond SDSS limits. Additionally, an X-ray versus radio relation for candidate SRC26340 could help ascertain or rule out an X-ray binary classification, but we did not find any X-ray detection of the source, only a single limit. We conclusively posit that the candidate could be part of a population of AGNs optically fainter than the SDSS limits. Other sources in this range from our candidates list are SRC27019, and the very faint magnitude limit on SRC27243.

SRC26347

The candidate lies in the parameter space where a GRB population has been observed, see the green "x". Sources in this range are also very much consistent with a significant sample of AGNs, a small sample of supernovae, X-ray binaries, and stellar sources. Within this area, and also within the same radio-optical flux ratio, several other candidates are found, such as SRC26606, SRC27078, as well as GRB190114C (see cyan square). This being said, it is very much likely that SRC26347 is an AGN below the FIRST limit, just like SRC27078 is a confirmed AGN placed in this region (see later for SRC27078).

SRC26606

We find that SRC26606 lies consistent with GRBs, much like SRC26347 and SRC27078. A significant population of optically detected AGNs are seen in this track, as well as poorly sampled populations of several stellar sources, X-ray binaries and supernovae. We conclude that SRC26606 is likely an AGN.

SRC26637

This is the only candidate we find that is just within the radio pulsars track of the radio-optical space. The candidate lies in the area where only AGNs and radio pulsars share a constant flux density ratio (see diagonal dotted line limits between 0.01mJy and 0.1mJy). The candidate appears very bright in the radio, but barely detected in the optical bands as shown in the bottom right corner of Figure A.6. The pulsars track remains poorly sampled with the majority being fainter than the SDSS limits. Further investigation into SRC26637 would help to unambiguously ascertain the nature of the candidate between either pulsar or quasar.

SRC26977

This candidate lies in a region where substantial populations of several source classes are well sampled. In this track there are quasars, GRBs, at least ten X-ray binaries, at least 16 stellar sources, two supernovae, and a pulsar. We can't definitively rule out the possibility that SRC26977 could be an AGN since there are many below the FIRST limit (e.g see discussion for SRC27078), but we also acknowledge that it could be any of the other classes. Further investigation can help to unambiguously classify the candidate.

SRC27019

Candidate, SRC27019, much like SRC26340, share similarities in their radio fluxes and optical magnitude, as shown by their overlapping in the radio-optical space. Similar to these is SRC27243 with a limit on its magnitude. These sources are fainter than the population of sources sampled by SDSS. We conclude that SRC27019 is likely in a population of fainter quasars than sampled.

SRC27078

We find this candidate to lie in the GRB track, but also where a significant population of AGNs have been observed (looking at the diagonal constant radio-optical flux ratios). We note that candidate SRC27078 is a confirmed AGN, J033504.75-274135.9 (Component number S662) as reported by Norris et al. (2006). The classification with our data is consistent with an AGN lying at the edge of the SDSS completeness limit, and very well below the FIRST limit. Considering the ratios in radio and optical fluxes where the candidate lies, we can confirm agreement with Norris et al. (2006) since a significant population of AGNs are detected in this range, particularly optically observed quasars. Other sources in this range are GRBs and X-ray binaries.

SRC27165

Candidate SRC27165 is the brightest source in our sample in terms of optical magnitudes. In this radio-optical parameter space, the candidate lies in a track where a very small sample of quasars lie. In this region, there is a cataclysmic variable, about eight X-ray binaries, at least 11 supernovae, and about 17 stellar type events. Considering that there are several quasars below the FIRST limit, SRC27165 is likely a nearby AGN given the bright and resolved galaxy at the location of the radio transient (see bottom right of Figure A.10). Spectroscopy with the Southern African Large Telescope (SALT), should be able to confirm this.

SRC27243

This candidate has the faintest optical magnitude, and consistently fainter radio fluxes. Given the limiting magnitude, we speculate that SRC27243 is likely in a population of very optically faint quasars, since it is at a similar radio flux level with SRC27078, which in contrast has a brighter optical magnitude, and is a confirmed AGN.

3.4.5 Variability Interpretation

We do not discover any strong transient candidates in the field. We instead discover several variable sources. The majority or nearly all of our identified candidates appear to be decisively well classified as some form of active galactic nuclei (AGNs). The variability of AGNs at radio frequencies is known to arise from both intrinsic and extrinsic attributes. Intrinsic variability is typically attributed to long term variability due to changing accretion dynamics or shocks due to jets at high frequencies, while extrinsic variability is due to interstellar scintillation effects at lower radio frequencies (Angelakis et al., 2012).

We have calculated the interstellar scintillation effects for this field as shown for GRB190114C at the centre (see Section 2.6 of Chapter 2). We found the field to be in the strong scintillation regime, with long lasting refractive scattering accounting for the variations. We calculated a refractive modulation index of $m_{refr} = 0.35$ indicating flux modulations at 35% rates in a timescale of approximately 5 days for the field. We conclude on these measurements that for sources we classified as possible AGNs, interstellar scintillation is the cause of variability.

3.5 Discussion

In this chapter, we took a commensal approach using the already existing MeerKAT field images of the very high energy GRB190114C to survey for potential variables or radio transients. The aim was to utilise the LOFAR Transients Pipeline, TraP, to blindly search the field and possibly discover interesting sources in the GRB background. The pipeline has been adapted for MeerKAT data with several publications already out. Initial tests jobs found that our original images used from Chapter 2 were rejected by quality control as they were over-sampled. Instead we used the 11 existing images of the field that were created with direction-dependent calibrations as outlined in MAGIC Collaboration et al. (2019b). The images were ran through the "ThunderTraP" using default parameters, such as a detection threshold of 8σ, an analysis threshold of 3σ and a search radius that is is just below half of the image size at 4060 pixels.

Analysis of our results showed significant realistic and artificial activity in the field, with numerous extended

or spurious artefacts being recorded as potential candidates. This necessitated a dedicated mechanism for filtering sources and removing all false positives. We employed a deduplication procedure that removed all sources that are five beamwidths from bright sources. These were either excessively bright sources or in very close proximity to bright sources, and thus had artificial variability which was influenced by nearby sources. After deduplication, we animated a sample of top 40 "interesting" sources, 20 with highest η values, and 20 with highest V values. We then visually categorised these sources as: point source, extended, spurious, and transient or variable. We rejected 17 sources which were not stable point sources, resulting in a sample of 23 sources. We then re-ran the TraP with the remaining 23 sources as monitors to recalculate their variability metrics. We further set another criteria to get a final selection of sources, rejecting all sources that had $\eta < 1$, accepting sources with $\eta > 2$ as candidates, and denoting sources between these η margins as "maybe". This resulted in a final sample of 12 candidate sources, 12th being GRB190114C at the image center, which we excluded for a final of 11 candidates. The candidate light curves indicated generally uncorrelated variability.

We queried broadband catalogues for counterparts in the optical bands, infrared, radio and X-rays. While we found reliable counterparts for the majority of candidates in the optical bands, only few had counterparts at radio and infrared. The radio counterparts are especially lacking due to the sensitivity limits of the most detailed surveys queried. We coupled the deep photometry data from the catalogues with the MeerKAT data to classify our sources, and found that the majority of the sample is well consistent with being AGNs. In fact one of the candidates, SRC27078, is a confirmed AGN, J033504.75-274135.9 (Norris et al., 2006). Our classification of this candidate with the radio-optical parameter space was also consistent with Norris et al. (2006). We concluded that this candidate, and others similarly classified as possible AGNs are likely variable due to interstellar scintillation effects as calculated for the field from Chapter 2.

These results are consistent with several studies that have found scintillating AGNs after investigating wide fields for transients. Examples include Thyagarajan et al. (2011) who found more than 80% of the sources in their fields being consistent with either confirmed and unconfirmed AGNs or other galaxy classes. A recent MeerKAT example is Driessen et al. (2022b) who found refractive scintillation being the most probable cause of observed long-term variability for variable candidates with light curves spanning over two years. This work is closely aligned with Chastain et al (submitted), who after surveying short GRB fields for transients and variables, also found mostly variable AGN, with variability attributed to refractive scintillation. Particularly interesting to this work is that Chastain et al (submitted) performed transient searches at different timescales; at eight seconds, 15 minutes, and 4 hours respectively, probing the different timescales for candidates. This is a planned approach at a later stage with the available data. The two studies (this work), and Chastain et al (submitted) are the only two MeerKAT studies that have surveyed known GRB fields for transients, searching both classes of long and short GRBs.

Chapter 4

Discussion and Future Outlook

In this final chapter, I give an overview of the main results of this dissertation, the methods applied to achieve these, as well as the implication of my results in each of the two undertakings of the project; i.e the GRB afterglow analysis, as well as the transients survey in the field.

Gamma ray bursts (GRBs) are on a class of their own as the most powerful explosions in the universe. Their afterglows can be studied to untangle their physics across the entire electromagnetic spectrum. The discovery of teraelectronvolt (TeV) emission from GRB190114C (MAGIC Collaboration et al., 2019a), as well as confirmation of inverse Compton scattering as the mechanism for this emission (MAGIC Collaboration et al., 2019b), was a very significant milestone towards understanding GRBs. This was one of the key feats for GRB studies since their very discovery in the late 1960s, and certainly a highlight for high energy astrophysics in 2019.

4.1 GRB190114C with MeerKAT

We observed GRB190114C within a day after the explosion, and successfully scheduled a long-term low frequency (1.28 GHz) campaign to study this GRB for nearly a year. Radio observations of long GRB afterglows at lower frequencies are still lacking. This is due to synchrotron self absorption frequency significantly reducing the flux levels or fluence compared to higher frequencies, where ample light curve sampling is usually largely realised. This in turn limits the opportunities to better constrain self-absorption effects at low frequencies, which when well established, eases efforts for estimating the full GRB calorimetry. Details of the full GRB calorimetry, as well as the inner workings of the central engine that powers the afterglows, can be well established if broadband observations include low radio frequency light curves that are well sampled at late times.

We obtained 13 epochs from our monitoring, each of which were over two hours in duration. We imaged the observations using ThunderKAT pipelines in IDIA, and accurately estimated fluxes at the confirmed location of the target, the centre in all images. We added a 10% flux uncertainty in quadrature to our flux error bars to correct for an intrinsic MeerKAT calibration error. We then plotted the light curve and fitted a smoothly broken power law.

From my analysis, I have found that the MeerKAT light curve was theoretically consistent with a forward shock propagating in a homogeneous medium up to over 100 days after the explosion. This was shown by a lingering steady and steep rise of the form $F \propto t^{0.5^{+0.2}_{-0.1}}$, which satisfies the assumptions of a classical fireball. I interpreted this as the peak frequency crossing our observing band. I found that the decay component of the light curve did not conform to standard spherical blast wave assumptions, given that the measured slope was too steep. I tested these assumptions for a homogeneous and wind medium to demonstrate that the values obtained for the electron injection energy slope, p, were atypical. Based on these, I favoured the interpretation with a jet break, while also conceding that testing other modelling solutions would also be a useful alternative.

MeerKAT observations of the field months prior to the GRB explosition were available, and we obtained an extrapolated flux estimate at the location of the GRB. I found that our modelling estimated host flux was most favourable in comparison with the pre-burst flux, since our estimate was in agreement with our final three epoch fluxes, which were at the host level. Agreement with the pre-burst flux was only possible when considering uncertainties. I also noted that the pre-burst extrapolation itself had a calibration uncertainty since the host was on the flank of the primary beam in those images, indicating that the flux is underestimated.

I performed a thorough analysis of the interstellar scintillation that was evident from the fluctuations in the light curve. I found that our observations were affected by strong scintillation, and in particular, refractive scattering. This was occurring at a rate of about 35% in flux at a timescale of nearly 5 days. From the refraction angle, I was also able to estimate the source scale of the afterglow to 5.623 kpc/arcsec, which corresponded to a physical size of $\theta_s = 3.6 \times 10^{18}$ cm. I compared this physical size to other afterglows for which constraints on the source size exit, such as for GRB030328 and GRB130427A, finding it similar in scale magnitudes but moderately larger.

In summary, our findings are consistent with a classical fireball, with a forward shock propagating into a homogeneous medium, and a break denoting the late passage of the characteristic peak frequency crossing our observing bands. Beyond the break, we posit a possible jet-break denoting lateral spreading.

4.2 MeerKAT Transients Survey in the GRB190114C field

I performed a transient survey using the deep images obtained from the extensive GRB190114C observing campaign. The aim for this was to possibly discover transient or variable sources in the background field. Commensal transient searches are becoming a common undertaking with the available ThunderKAT data, as well as data from other MeerKAT LSPs. We thus took an opportunity to re-investigate the field for any transient activity.

We used 11 alternative images available spanning 204 days created in the manner outlined in MAGIC Collaboration et al. (2019b), since the original images failed quality control with the pipeline. The default pipeline parameters were applied, i.e an 8σ detection threshold, a 3σ analysis threshold, and only surveying the field up to just less than half of the image size at 4060 pixels to minimise false positives due to primary beam calibrations.

The field showed real and artificial activity. We carried out a deduplication procedure to remove all sources that had artificial variability parameters. These were sources in very close proximity to spurious artefacts, or intrinsically very bright sources. This procedure resulted in the animation of 40 candidates, from which visual inspection filtered the sample to 23 sources. These sources were then rerun through the TraP pipeline as monitors to obtain the final light curves, and the variability metrics, $\eta > 2$ and V, calculated by TraP from those light curves. From this sample, all sources that did not meet the $\eta > 2$ criteria were essentially rejected. The final candidate sample was 11 candidate sources, excluding GRB190114C at the image center. Detecting GRB190114C as a potential candidate in the sample added some confidence to the effectiveness of the pipeline, and the results. The candidate light curves showed independent and uncorrelated evolution from source to source.

We found multi-wavelength counterparts for our candidates using archival catalogues at optical, radio, X-ray, and Infrared bands. We also obtained the deepest photometry data from the DES catalogue, which we utilised to classify the candidates and unravel their nature. We utilised an existing radio-optical parameter space by Stewart et al. (2018) to classify our candidates. We found that we have mainly discovered a series of variables, most of which are possible AGNs based on the classification scheme used. In fact, one of the candidates, SRC27078 is indeed a confirmed AGN (Norris et al., 2006), and our classification further attested to this. This also suggested that most of our candidates in the same portion of the radio-optical parameter space were also AGNs. Very few of the sources had unconvincing classifications and may be studied further in future. We concluded that refractive interstellar scintillation as studied for the field in Chapter 2 was the main cause of variability for the candidates classified as possible AGNs.

4.3 Future Outlook

The available data for GRB190114C still has ample potential for re-investigation beyond the scope of this dissertation. The GRB field data is yet to be modelled in concert with the available broadband data, particularly all the available radio and X-ray data (Gropp et al., 2019; Hamburg et al., 2019; Laskar et al., 2019; Misra et al., 2021). Current progress has combined MeerKAT, uGMRT, and Swift data for modelling (Aksulu et al. to be submitted). Combining the full available data sets provides an opportunity to estimate the full calorimetry of GRB190114C. Our early MeerKAT observations demonstrate that sensitive instruments such as MeerKAT may be excellent tools for observing long GRB afterglows at synchrotron self absorption levels, which remains largely limited for the majority of radio detected GRB afterglows. Our expansive sampling around the light curve break, as well as at late times is critical for estimating the energetics of the burst, and indirectly studying the central engine powering the afterglow. The field at large can also be re-imaged at shorter timescales, down to 8 second scans, and these snapshots then being used to search for transients such as in Chastain et al (submitted). Since this is a computationally exhaustive process given the volumes of data already available, this is a near future endeavour.

This work builds upon the existing MeerKAT transient studies investigating broad phenomena ranging from Galactic transients such as black hole candidates, cataclysmic variables, and far out into the cosmos with supernoave and numerous GRBs. This scope lays down the foundation in preparation for the upcoming Square Kilometer Array (SKA). The SKA is expected to revolutionise radio interferometry with very wide field coverage, high sensitivity, and high data volumes from individual observations. Our currently applied methods of investigation, be it imaging for targeted studies such as for GRB190114C as a subject of interest, or its field as a potential for transients and variable surveys, will largely be changed over time. The available computing infrastructure will also be likely expanded to handle the expected large volumes, and enhanced for better processing speeds. While we productively wait for the SKA, current approaches and technologies still suffice and are constantly being improved.

Appendix A

Candidate Postage Stamps

This appendix supplies the postage stamps for each of the transient or variable candidates discovered in Chapter 3 with the TraP pipeline. We created movies for these sources, which can be accessed at the the Github repository: Candidate Movies Repository Link. The radio postage stamps are supplemented with the deepest corresponding optical coverage of the sky position with the Dark Energy Survey (DR2) (Abbott et al., 2021). All the radio and optical snapshots are 60 arcsec across. The radio snapshots show the source position (dominated by the candidate) and flux density scale on the right, while the optical images indicate the source position and some background sources.

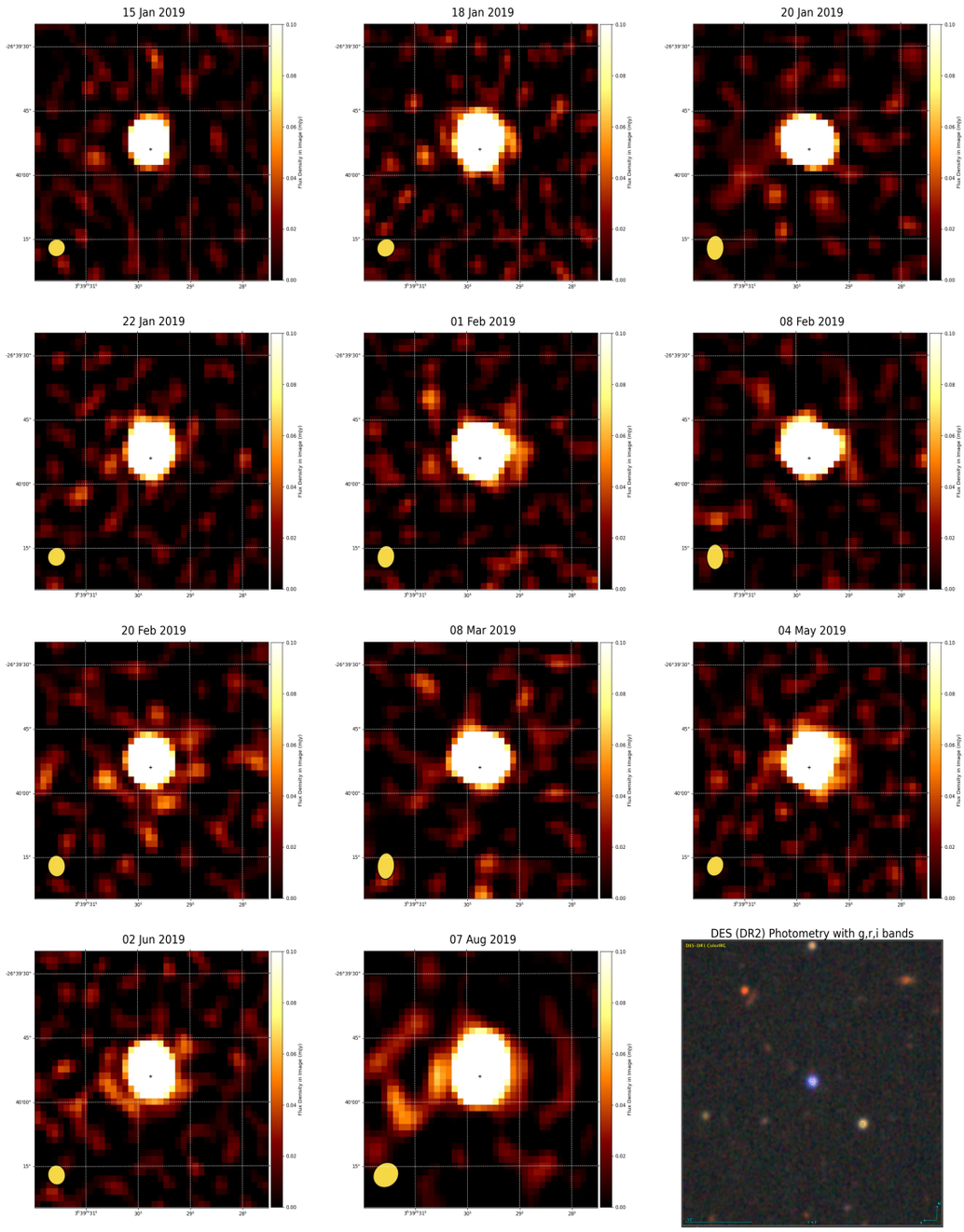

Figure A.1: Postage stamps of SRC26088. Ordered top left to right, middle left to right, bottom left to right. North is up, East is left in all the images. The snaps, both radio and optical, are 60 arcseconds across. The small black cross in the radio images indicates the MeerKAT position of the candidate, and this is shown with a pink cross at the centre of the DES (DR2) image.

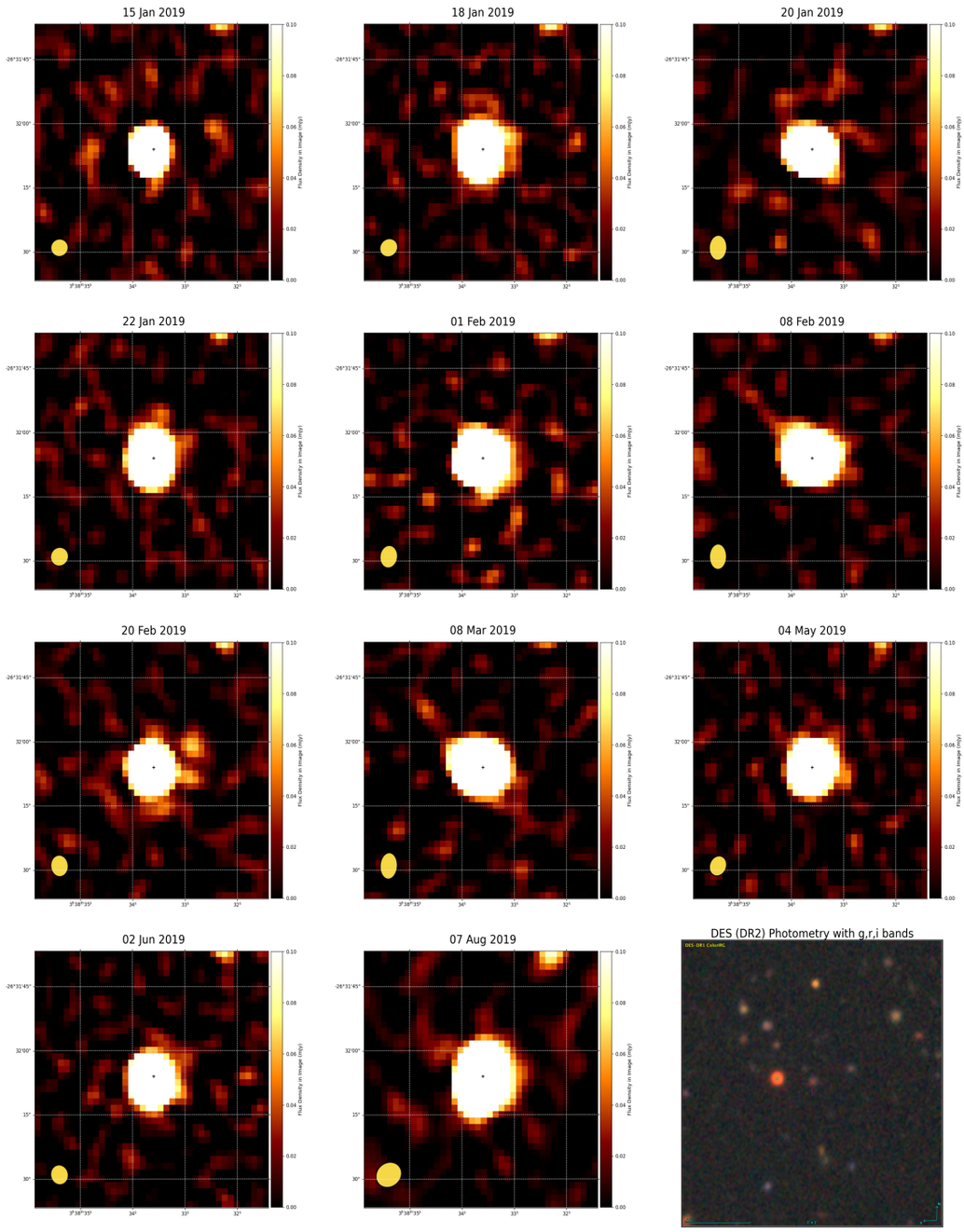

Figure A.2: Postage stamps of SRC26261. Ordered top left to right, middle left to right, bottom left to right. North is up, East is left in all the images. The snaps, both radio and optical, are 60 arcseconds across. The small black cross in the radio images indicates the MeerKAT position of the candidate, and this is shown with a pink cross at the centre of the DES (DR2) image.

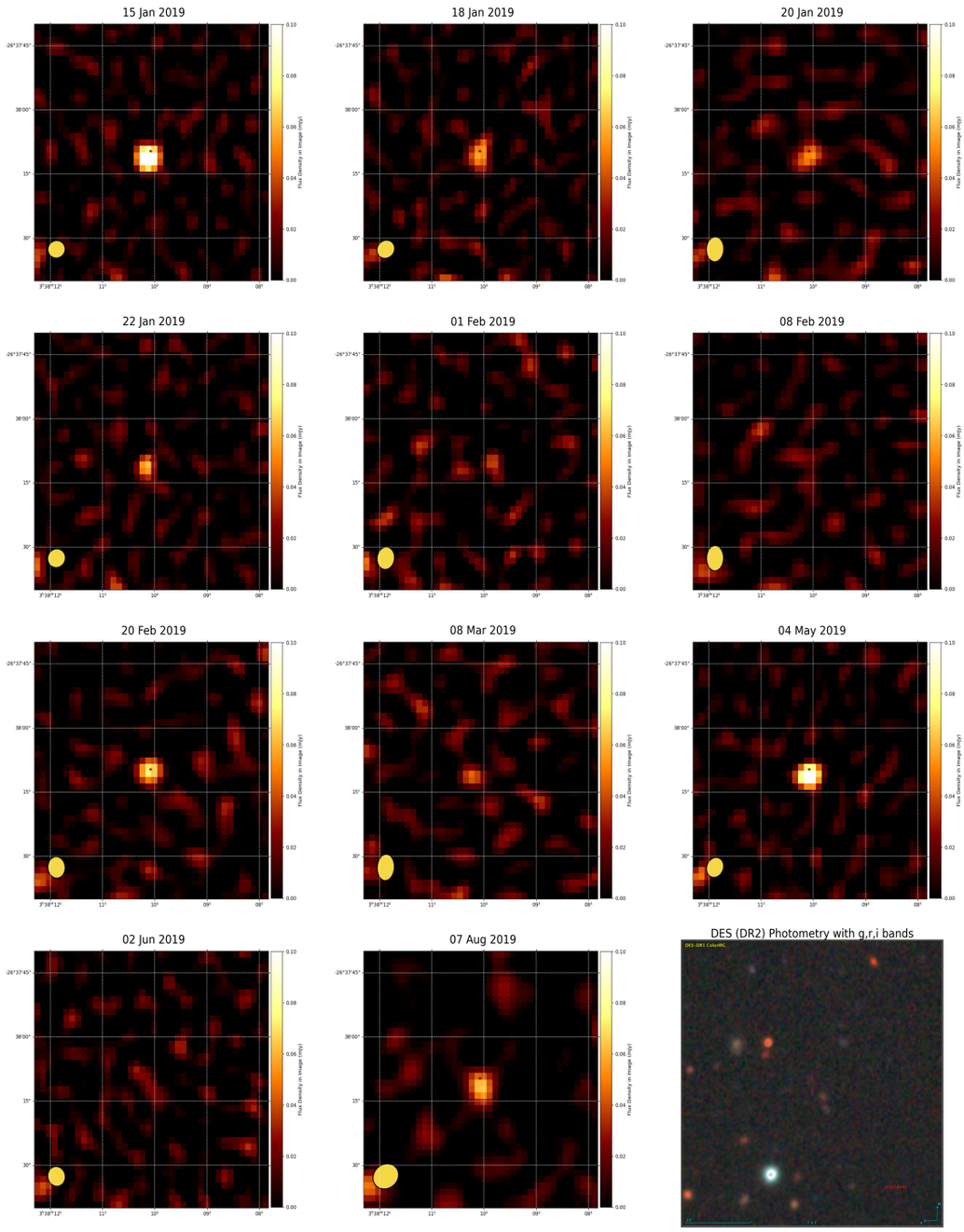

Figure A.3: Postage stamps of SRC26340. Ordered top left to right, middle left to right, bottom left to right. North is up, East is left in all the images. The snaps, both radio and optical, are 60 arcseconds across. The small black cross in the radio images indicates the MeerKAT position of the candidate, and this is shown with a pink cross at the centre of the DES (DR2) image.

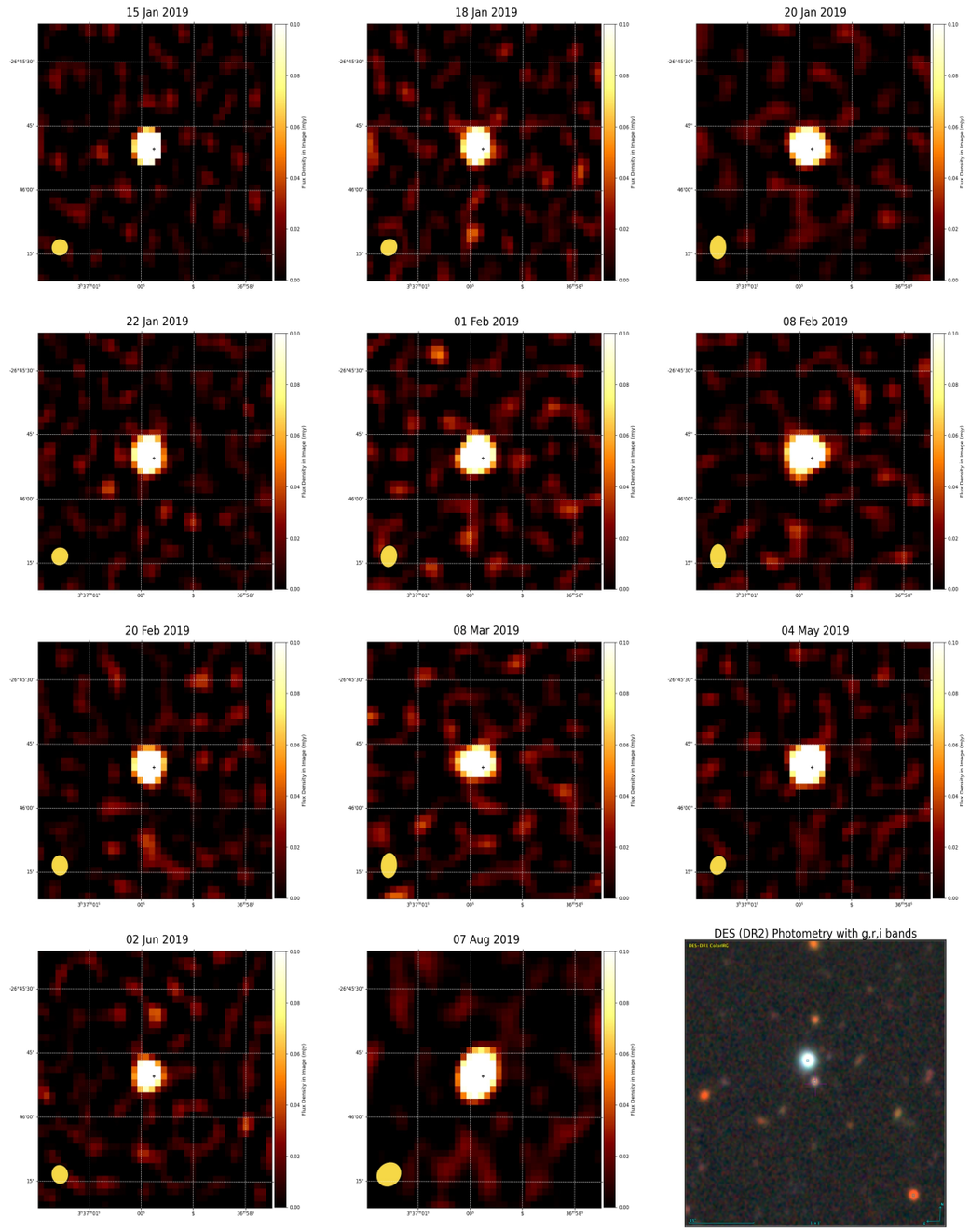

Figure A.4: Postage stamps of SRC26347. Ordered top left to right, middle left to right, bottom left to right. North is up, East is left in all the images. The snaps, both radio and optical, are 60 arcseconds across. The small black cross in the radio images indicates the MeerKAT position of the candidate, and this is shown with a pink cross at the centre of the DES (DR2) image.

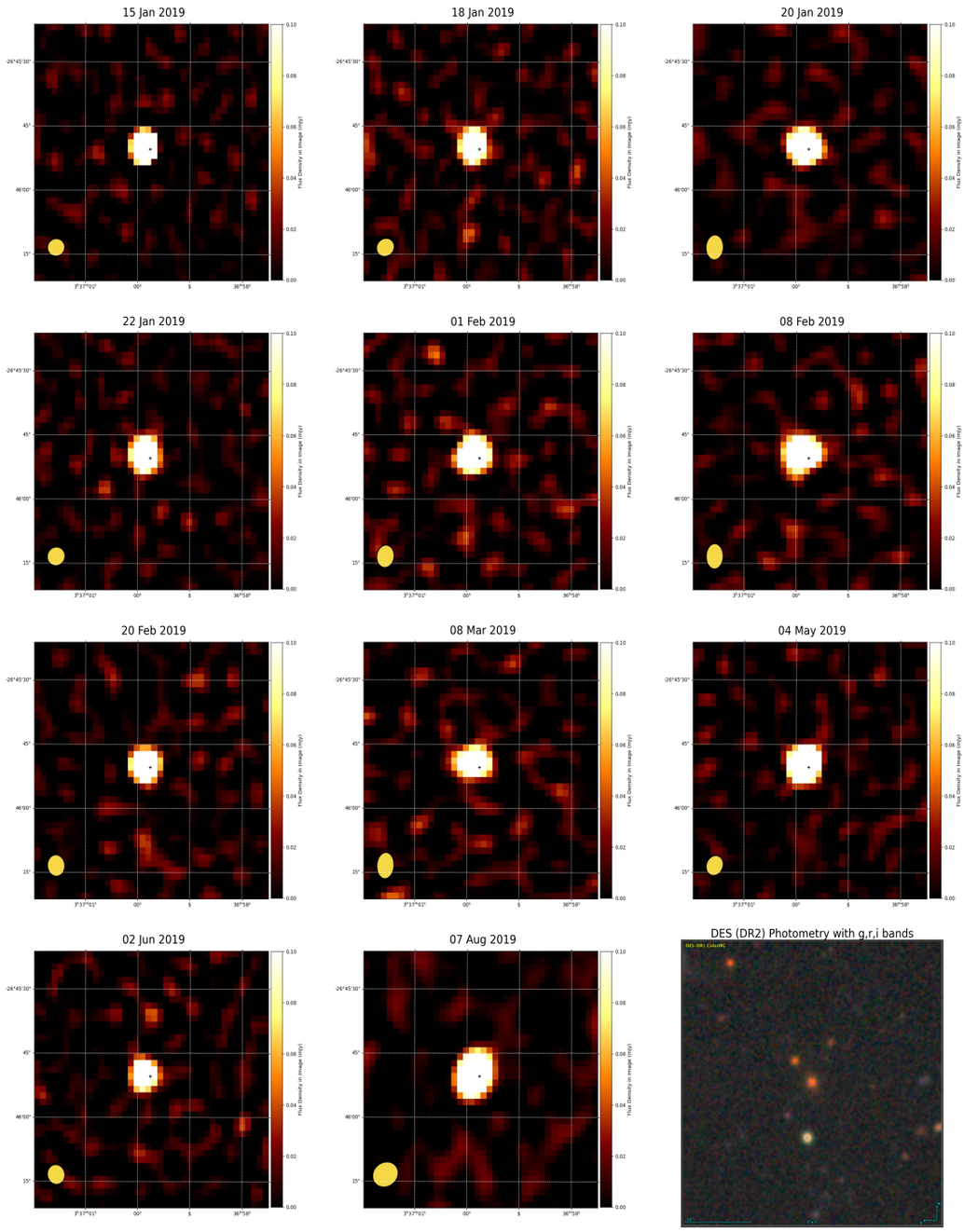

Figure A.5: Postage stamps of SRC26606. Ordered top left to right, middle left to right, bottom left to right. North is up, East is left in all the images. The snaps, both radio and optical, are 60 arcseconds across. The small black cross in the radio images indicates the MeerKAT position of the candidate, and this is shown with a pink cross at the centre of the DES (DR2) image.

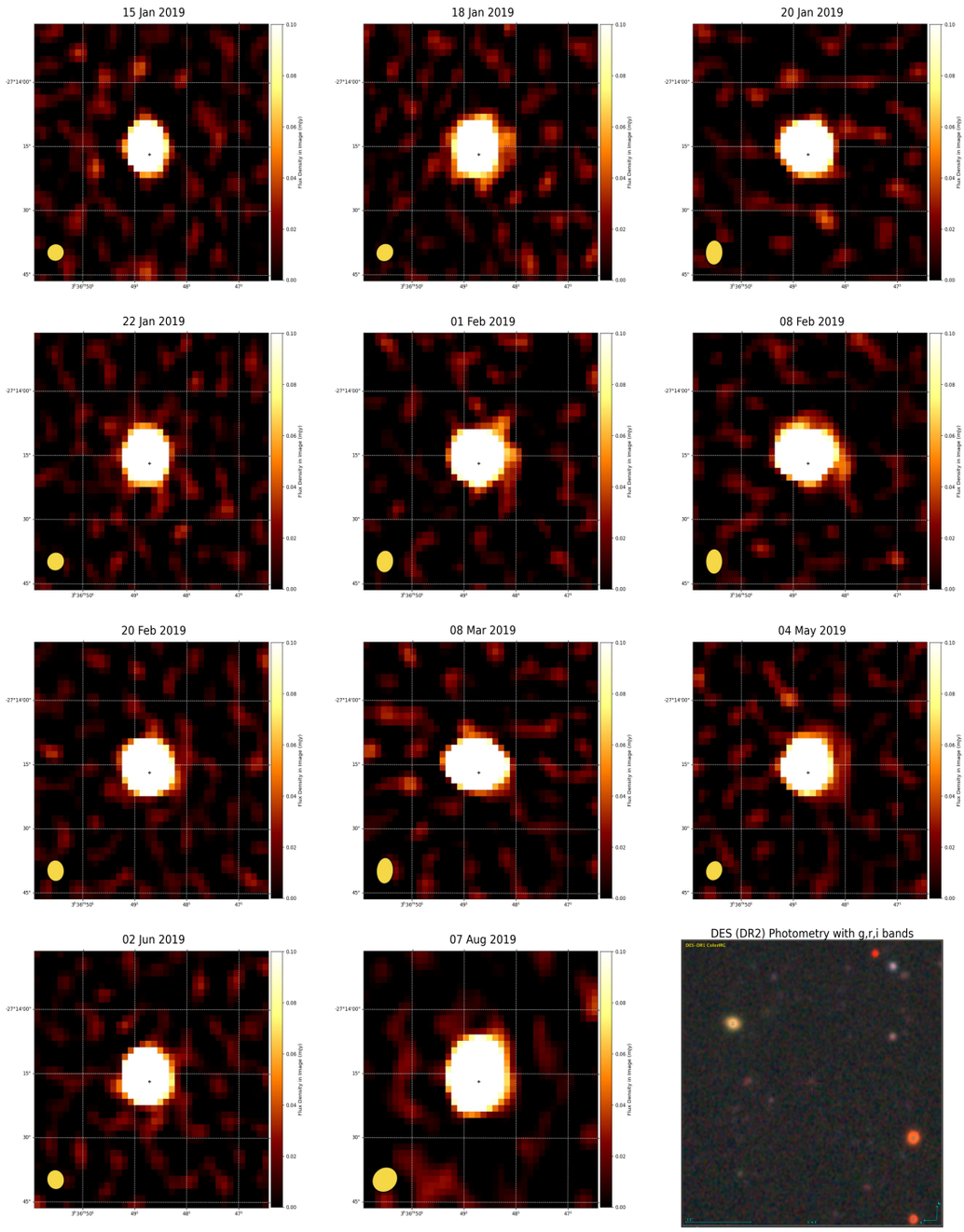

Figure A.6: Postage stamps of SRC26637. Ordered top left to right, middle left to right, bottom left to right. North is up, East is left in all the images. The snaps, both radio and optical, are 60 arcseconds across. The small black cross in the radio images indicates the MeerKAT position of the candidate, and this is shown with a pink cross at the centre of the DES (DR2) image.

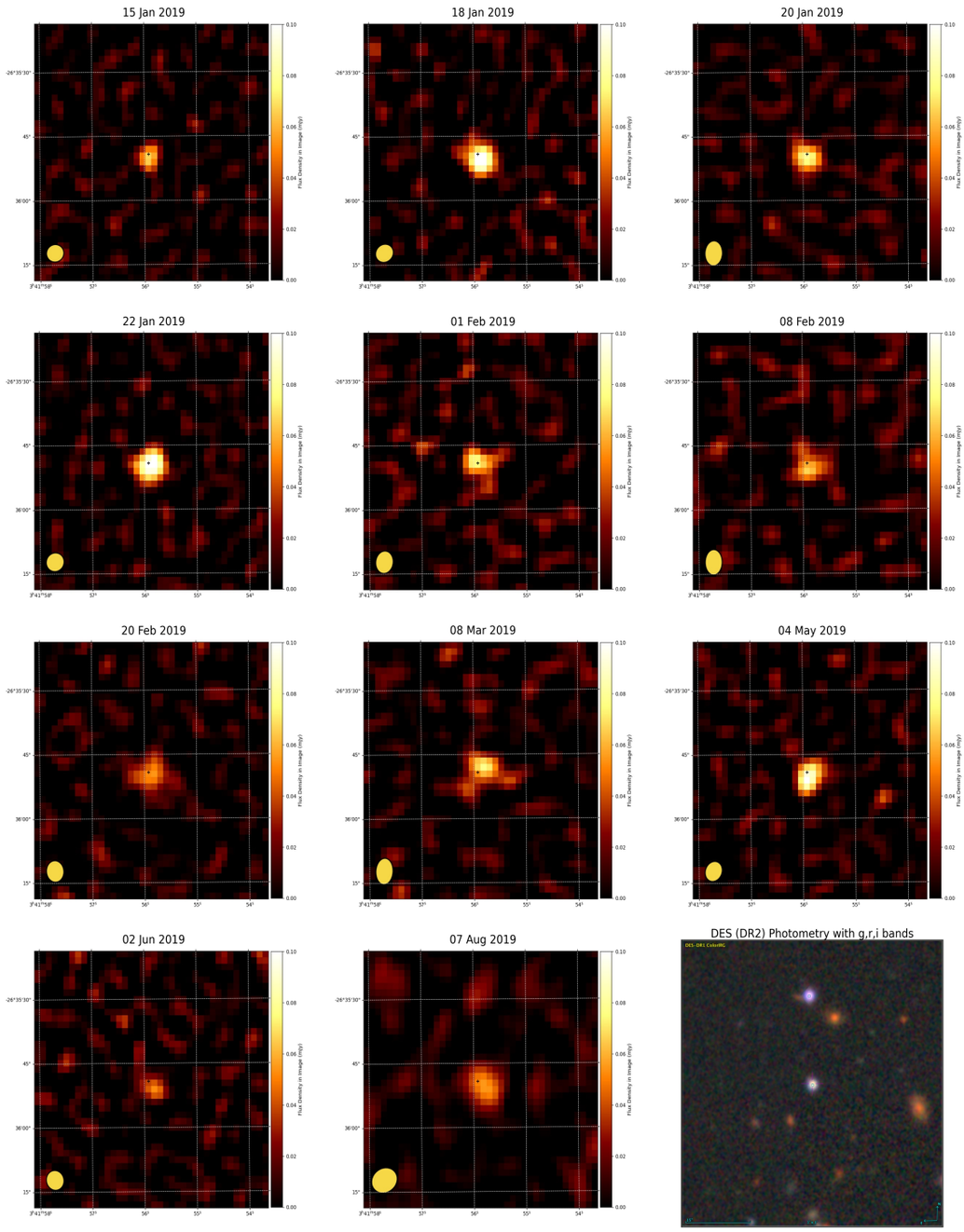

Figure A.7: Postage stamps of SRC26977. Ordered top left to right, middle left to right, bottom left to right. North is up, East is left in all the images. The snaps, both radio and optical, are 60 arcseconds across. The small black cross in the radio images indicates the MeerKAT position of the candidate, and this is shown with a pink cross at the centre of the DES (DR2) image.

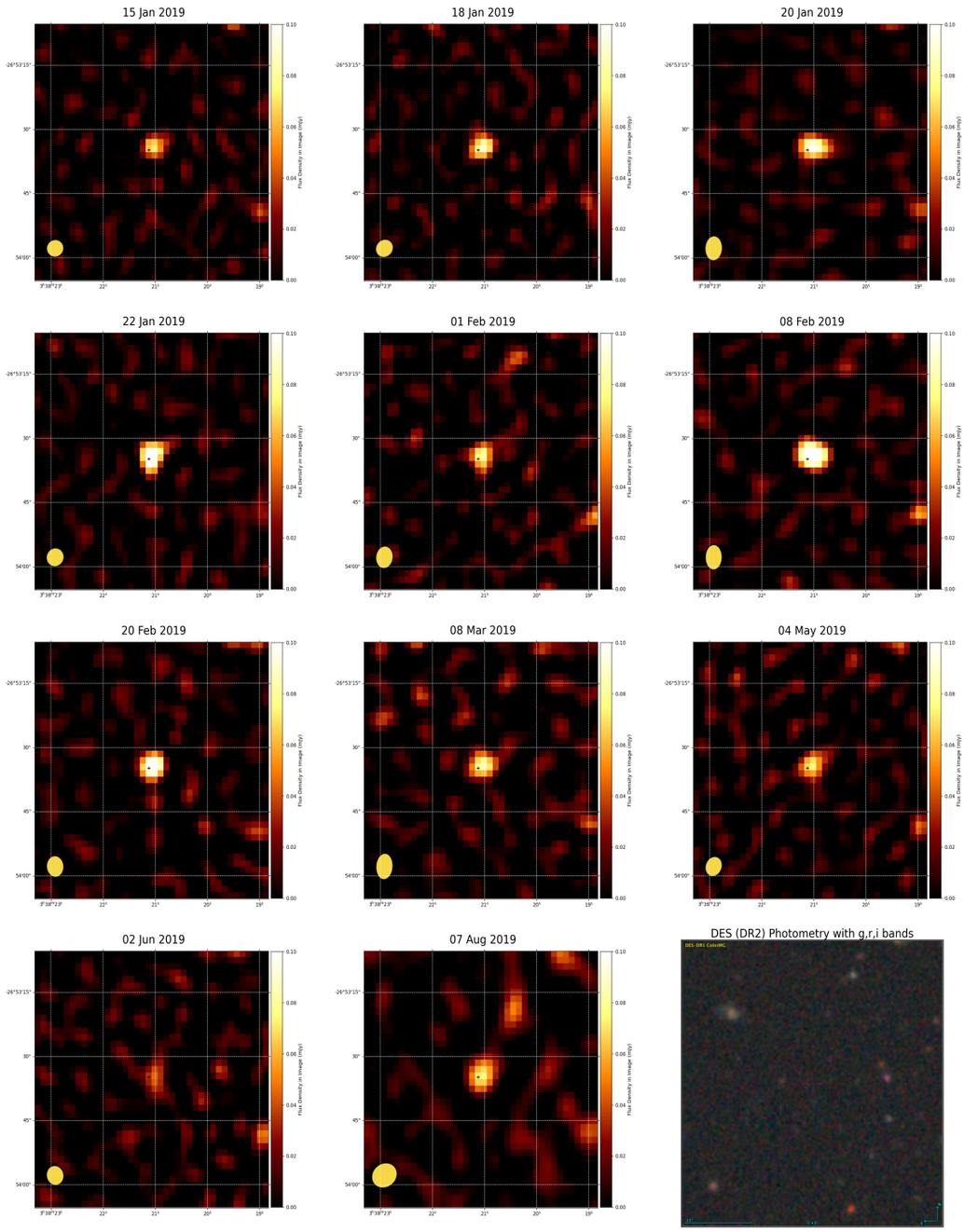

Figure A.8: Postage stamps of SRC27019. Ordered top left to right, middle left to right, bottom left to right. North is up, East is left in all the images. The snaps, both radio and optical, are 60 arcseconds across. The small black cross in the radio images indicates the MeerKAT position of the candidate, and this is shown with a pink cross at the centre of the DES (DR2) image.

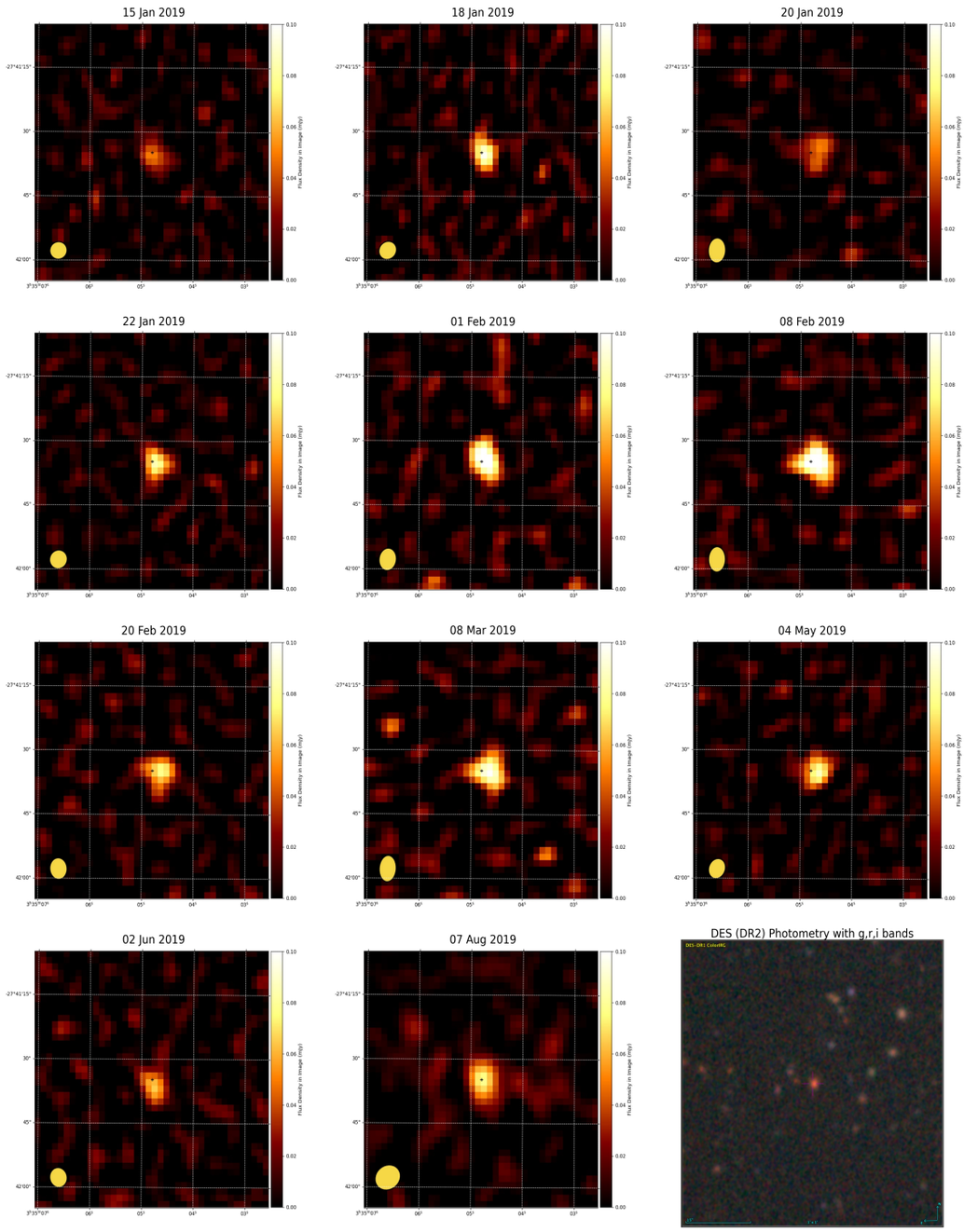

Figure A.9: Postage stamps of SRC27078. Ordered top left to right, middle left to right, bottom left to right. North is up, East is left in all the images. The snaps, both radio and optical, are 60 arcseconds across. The small black cross in the radio images indicates the MeerKAT position of the candidate, and this is shown with a pink cross at the centre of the DES (DR2) image.

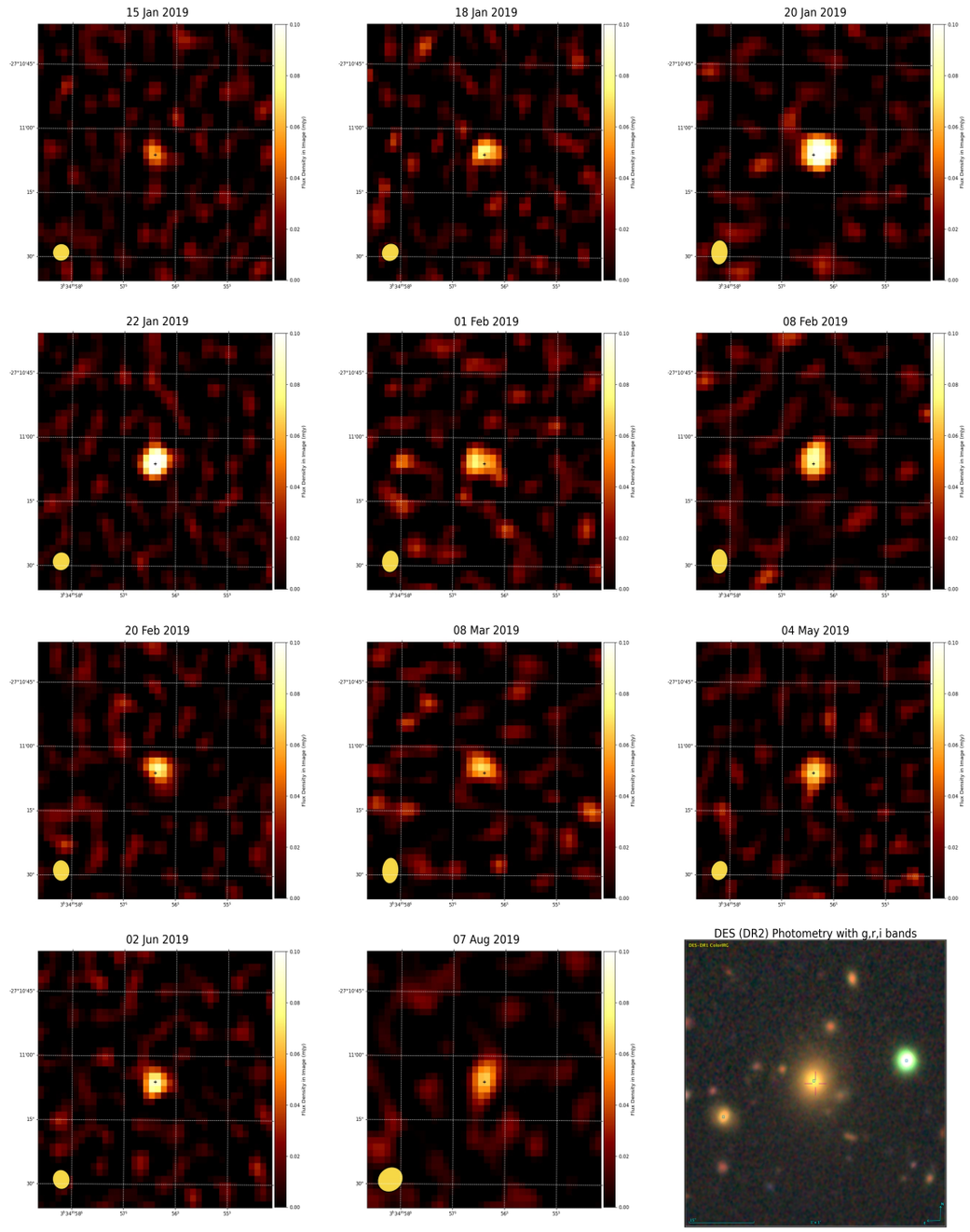

Figure A.10: Postage stamps of SRC27165. Ordered top left to right, middle left to right, bottom left to right. North is up, East is left in all the images. The snaps, both radio and optical, are 60 arcseconds across. The small black cross in the radio images indicates the MeerKAT position of the candidate, and this is shown with a pink cross at the centre of the DES (DR2) image.

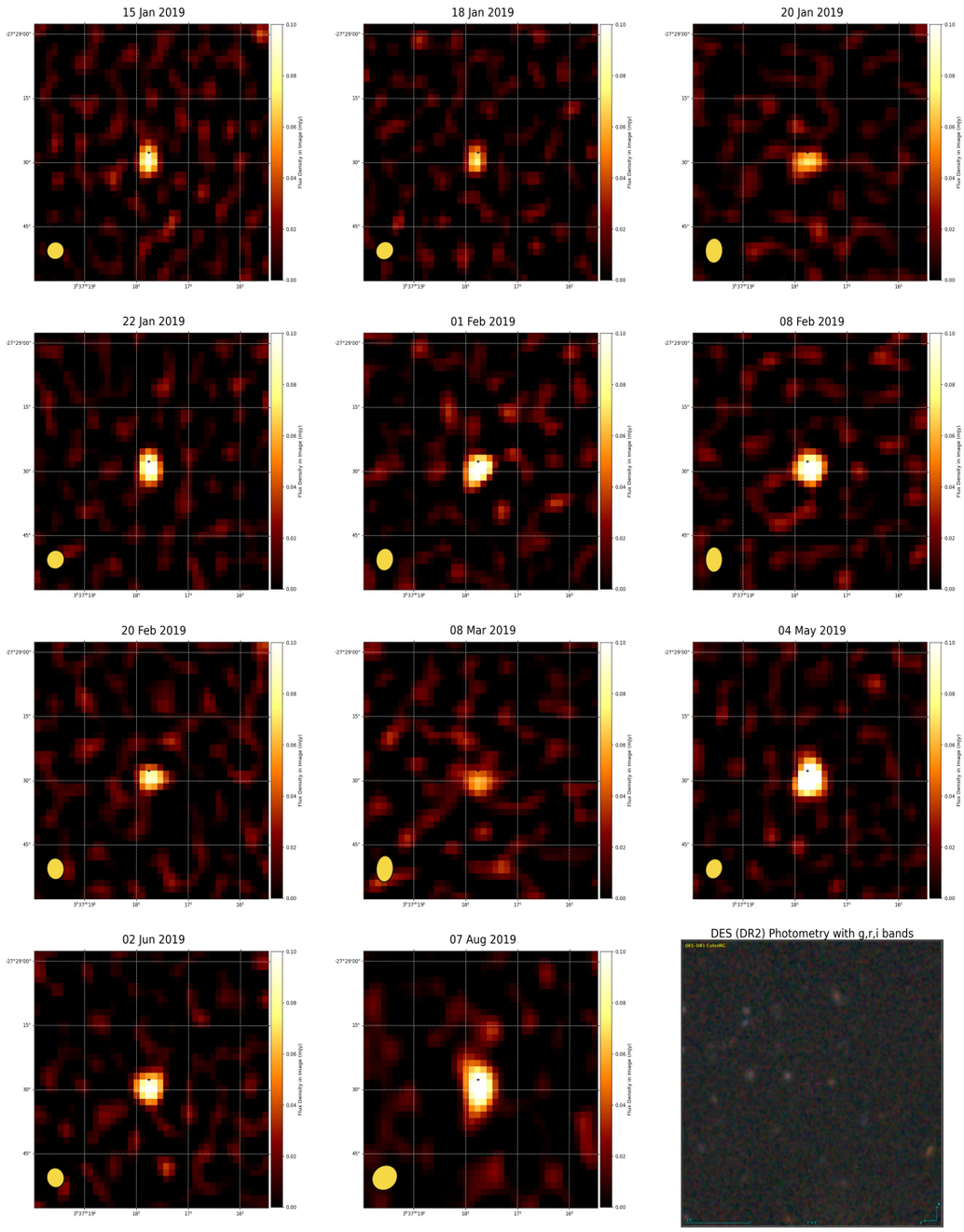

Figure A.11: Postage stamps of SRC27243. Ordered top left to right, middle left to right, bottom left to right. North is up, East is left in all the images. The snaps, both radio and optical, are 60 arcseconds across. The small black cross in the radio images indicates the MeerKAT position of the candidate, and this is shown with a pink cross at the centre of the DES (DR2) image.

Bibliography

Abbott B. P., et al., 2016, Physical Review Letters, 116, 061102

Abbott B. P., et al., 2017a, Physical Review Letters, 119, 161101

Abbott B. P., et al., 2017b, The Astrophysical Journal Letters, 848, L12

Abbott T. M. C., et al., 2021, The Astrophysical Journal Supplement Series, 255, 20

Abdalla H., et al., 2019, Nature, 575, 464

Acciari V. A., et al., 2021, The Astrophysical Journal, 908, 90

Ackermann M., et al., 2014, Science, 343, 42

Ajello M., et al., 2019, The Astrophysical Journal, 878, 52

Aleksić J., et al., 2016a, Astroparticle Physics, 72, 61

Aleksić J., et al., 2016b, Astroparticle Physics, 72, 76

Anderson G. E., et al., 2023, Monthly Notices of the Royal Astronomical Society, 523, 4992

Andersson A., et al., 2022, Monthly Notices of the Royal Astronomical Society, 513, 3482

Angelakis E., et al., 2012, in Journal of Physics Conference Series. p. 012007 (arXiv:1202.4242), doi:10.1088/1742-6596/372/1/012007

Bannister K. W., Murphy T., Gaensler B. M., Hunstead R. W., Chatterjee S., 2011, Monthly Notices of the Royal Astronomical Society, 412, 634

Bannister K. W., et al., 2019, Science, 365, 565

Berger E., et al., 2005, Nature, 438, 988

Blandford R. D., Ostriker J. P., 1978, The Astrophysical Journal Letters, 221, L29

Bloom J. S., et al., 2002, The Astrophysical Journal Letters, 572, L45

Bower G. C., Saul D., Bloom J. S., Bolatto A., Filippenko A. V., Foley R. J., Perley D., 2007, The Astrophysical Journal, 666, 346

Briggs D. S., 1995, in American Astronomical Society Meeting Abstracts. p. 112.02

Bright J. S., et al., 2020, Nature Astronomy, 4, 697

Burke B. F., Franklin K. L., 1955, Journal of Geophysical Research, 60, 213

CHIME/FRB Collaboration et al., 2019, The Astrophysical Journal Letters, 885, L24

Camilo F., et al., 2018, The Astrophysical Journal, 856, 180

Carbone D., et al., 2016, Monthly Notices of the Royal Astronomical Society, 459, 3161

Castro-Tirado A. J., et al., 2019, GRB Coordinates Network, 23708, 1

Cavallo G., Rees M. J., 1978, Monthly Notices of the Royal Astronomical Society, 183, 359

Chandra P., Cenko S. B., Frail D. A., Chevalier R. A., Macquart J.-P., Kulkarni S. R., Bock D. C. J., Bertoldi F., 2008, in Galassi M., Palmer D., Fenimore E., eds, American Institute of Physics Conference Series Vol. 1000, Gamma-ray Bursts 2007. pp 346–349, doi:10.1063/1.2943480

Cohen M. H., Cannon W., Purcell G. H., Shaffer D. B., Broderick J. J., Kellermann K. I., Jauncey D. L., 1971, The Astrophysical Journal, 170, 207

Colgate S. A., 1968, Canadian Journal of Physics Supplement, 46, 476

Condon J. J., Cotton W. D., Greisen E. W., Yin Q. F., Perley R. A., Taylor G. B., Broderick J. J., 1998, The Astronomical Journal, 115, 1693

Coppejans D. L., Körding E. G., Miller-Jones J. C. A., Rupen M. P., Knigge C., Sivakoff G. R., Groot P. J., 2015, Monthly Notices of the Royal Astronomical Society, 451, 3801

Corbel S., Coriat M., Brocksopp C., Tzioumis A. K., Fender R. P., Tomsick J. A., Buxton M. M., Bailyn C. D., 2013, Monthly Notices of the Royal Astronomical Society, 428, 2500

Cordes J. M., Lazio T. J. W., 2002, arXiv e-prints, pp astro–ph/0207156

Cordes J. M., Lazio T. J. W., McLaughlin M. A., 2004, New Astronomy Reviews, 48, 1459

Costa E., et al., 1997, Nature, 387, 783

Djorgovski S. G., et al., 1997, Nature, 387, 876

Djorgovski S. G., Kulkarni S. R., Bloom J. S., Goodrich R., Frail D. A., Piro L., Palazzi E., 1998, The Astrophysical Journal Letters, 508, L17

Driessen L. N., et al., 2020, Monthly Notices of the Royal Astronomical Society, 491, 560

Driessen L. N., Williams D. R. A., McDonald I., Stappers B. W., Buckley D. A. H., Fender R. P., Woudt P. A., 2022a, Monthly Notices of the Royal Astronomical Society, 510, 1083

Driessen L. N., et al., 2022b, Monthly Notices of the Royal Astronomical Society, 512, 5037

Eichler D., Waxman E., 2005, The Astrophysical Journal, 627, 861

Eichler D., Livio M., Piran T., Schramm D. N., 1989, Nature, 340, 126

Evans P. A., Page K. L., Beardmore A. P., Eyles-Ferris R. A. J., Osborne J. P., Campana S., Kennea J. A., Cenko S. B., 2023, Monthly Notices of the Royal Astronomical Society, 518, 174

Fender R. P., Bell M. E., 2011, Bulletin of the Astronomical Society of India, 39, 315

Fender R., Belloni T., 2012, Science, 337, 540

Fender R., Stewart A., Macquart J. P., Donnarumma I., Murphy T., Deller A., Paragi Z., Chatterjee S., 2015, in Advancing Astrophysics with the Square Kilometre Array (AASKA14). p. 51 (arXiv:1507.00729)

Fender R., et al., 2016, in MeerKAT Science: On the Pathway to the SKA. p. 13 (arXiv:1711.04132), doi:10.22323/1.277.0013

Flewelling H. A., et al., 2020, The Astrophysical Journal Supplement Series, 251, 7

Foreman-Mackey D., Hogg D. W., Lang D., Goodman J., 2013, Publications of the Astronomical Society of the Pacific, 125, 306

Fox D. B., et al., 2005, Nature, 437, 845

Frail D. A., Kulkarni S. R., Nicastro L., Feroci M., Taylor G. B., 1997, Nature, 389, 261

Frail D. A., Kulkarni S. R., Ofek E. O., Bower G. C., Nakar E., 2012, The Astrophysical Journal, 747, 70

Fukami S., et al., 2022, in 37th International Cosmic Ray Conference. p. 788, doi:10.22323/1.395.0788

Galama T. J., et al., 1998, Nature, 395, 670

Gallo E., Fender R. P., Miller-Jones J. C. A., Merloni A., Jonker P. G., Heinz S., Maccarone T. J., van der Klis M., 2006, Monthly Notices of the Royal Astronomical Society, 370, 1351

Gehrels N., et al., 2004, The Astrophysical Journal, 611, 1005

Goodman J., 1997, New Astronomy, 2, 449

Gordon Y. A., et al., 2021, The Astrophysical Journal Supplement Series, 255, 30

Granot J., 2007, in Revista Mexicana de Astronomia y Astrofisica, vol. 27. pp 140–165 (arXiv:astro-ph/0610379)

Granot J., Sari R., 2002, The Astrophysical Journal, 568, 820

Granot J., van der Horst A. J., 2014, Publications of the Astronomical Society of Australia, 31, e008

Granot J., Piran T., Sari R., 1999, The Astrophysical Journal, 527, 236

Granot J., Ramirez-Ruiz E., Loeb A., 2005, The Astrophysical Journal, 618, 413

Groot P. J., et al., 1998, The Astrophysical Journal Letters, 502, L123

Gropp J. D., et al., 2019, GRB Coordinates Network, 23688, 1

H. E. S. S. Collaboration et al., 2014, Astronomy & Astrophysics, 565, A16

H. E. S. S. Collaboration et al., 2021, Science, 372, 1081

Hamburg R., Veres P., Meegan C., Burns E., Connaughton V., Goldstein A., Kocevski D., Roberts O. J., 2019, GRB Coordinates Network, 23707, 1

Hewish A., Bell S. J., Pilkington J. D. H., Scott P. F., Collins R. A., 1968, Nature, 217, 709

Hewitt D. M., et al., 2020, Monthly Notices of the Royal Astronomical Society, 496, 2542

Heywood I., et al., 2019, Nature, 573, 235

Hjellming R. M., Wade C. M., 1971a, The Astrophysical Journal Letters, 168, L21

Hjellming R. M., Wade C. M., 1971b, Nature, 234, 138

Hjellming R. M., Gibson D. M., Owen F. N., 1975, Nature, 256, 111

Hjorth J., et al., 2003, Nature, 423, 847

Huang Y., Hu S., Chen S., Zha M., Liu C., Yao Z., Cao Z., Experiment T. L., 2022, GRB Coordinates Network, 32677, 1

Jarvis M., et al., 2016, in MeerKAT Science: On the Pathway to the SKA. p. 6 (arXiv:1709.01901)

Johnston S., et al., 2007, Publications of the Astronomical Society of Australia, 24, 174

Jonas J., MeerKAT Team 2016, in MeerKAT Science: On the Pathway to the SKA. p. 1

Katz J. I., 1994, The Astrophysical Journal Letters, 432, L107

Khangale Z. N., et al., 2020, Monthly Notices of the Royal Astronomical Society, 492, 4298

Klebesadel R. W., Strong I. B., Olson R. A., 1973, The Astrophysical Journal Letters, 182, L85

Körding E., Falcke H., Corbel S., 2006, Astronomy & Astrophysics, 456, 439

Kouveliotou C., Meegan C. A., Fishman G. J., Bhat N. P., Briggs M. S., Koshut T. M., Paciesas W. S., Pendleton G. N., 1993, The Astrophysical Journal Letters, 413, L101

Kuiack M., Huizinga F., Molenaar G., Prasad P., Rowlinson A., Wijers R. A. M. J., 2019, Monthly Notices of the Royal Astronomical Society, 482, 2502

Kulkarni S. R., et al., 1998, Nature, 395, 663

Kumar P., Panaitescu A., 2008, Monthly Notices of the Royal Astronomical Society: Letters, 391, L19

Kumar P., Zhang B., 2015, Physics Reports, 561, 1

Lacy M., et al., 2020, Publications of the Astronomical Society of the Pacific, 132, 035001

Laskar T., et al., 2019, The Astrophysical Journal Letters, 878, L26

Lesage S., et al., 2023, The Astrophysical Journal Letters, 952, L42

Levinson A., Ofek E. O., Waxman E., Gal-Yam A., 2002, The Astrophysical Journal, 576, 923

Longair M. S., 2011, High Energy Astrophysics

Lorimer D. R., Bailes M., McLaughlin M. A., Narkevic D. J., Crawford F., 2007, Science, 318, 777

MAGIC Collaboration et al., 2019a, Nature, 575, 455

MAGIC Collaboration et al., 2019b, Nature, 575, 459

Marcote B., et al., 2020, Nature, 577, 190

Mauch T., et al., 2020, The Astrophysical Journal, 888, 61

McMullin J. P., Waters B., Schiebel D., Young W., Golap K., 2007, in Shaw R. A., Hill F., Bell D. J., eds, Astronomical Society of the Pacific Conference Series Vol. 376, Astronomical Data Analysis Software and Systems XVI. p. 127

Meegan C., et al., 2009, The Astrophysical Journal, 702, 791

Mészáros P., 2003, Nature, 423, 809

Metzger M. R., Djorgovski S. G., Kulkarni S. R., Steidel C. C., Adelberger K. L., Frail D. A., Costa E., Frontera F., 1997, Nature, 387, 878

Mirabel I. F., Rodríguez L. F., 1994, Nature, 371, 46

Mirzoyan R., et al., 2019, GRB Coordinates Network, 23701, 1

Misra K., et al., 2021, Monthly Notices of the Royal Astronomical Society, 504, 5685

Mohan N., Rafferty D., 2015, PyBDSF: Python Blob Detection and Source Finder (ascl:1502.007)

Mooley K. P., et al., 2016, The Astrophysical Journal, 818, 105

Mooley K. P., et al., 2018, The Astrophysical Journal Letters, 868, L11

Murphy T., et al., 2013, Publications of the Astronomical Society of Australia, 30, e006

Murphy T., et al., 2017, Monthly Notices of the Royal Astronomical Society, 466, 1944

Narayan R., 1992, Philosophical Transactions of the Royal Society of London Series A, 341, 151

Norris R. P., et al., 2006, The Astronomical Journal, 132, 2409

Offringa A. R., van de Gronde J. J., Roerdink J. B. T. M., 2012, Astronomy & Astrophysics, 539, A95

Offringa A. R., McKinley B., Hurley-Walker et al., 2014, MNRAS, 444, 606

Onken C. A., et al., 2019, Publications of the Astronomical Society of Australia, 36, e033

Pihlström Y. M., Taylor G. B., Granot J., Doeleman S., 2007, The Astrophysical Journal, 664, 411

Piran T., 2003, Nature, 422, 268

Piran T., 2005, Rev. Mod. Phys., 76, 1143

Platts E., Weltman A., Walters A., Tendulkar S. P., Gordin J. E. B., Kandhai S., 2019, Physics Reports, 821, 1

Polisensky E., et al., 2016, The Astrophysical Journal, 832, 60

Rees M. J., Meszaros P., 1992, Monthly Notices of the Royal Astronomical Society, 258, 41

Rees M. J., Meszaros P., 1994, The Astrophysical Journal Letters, 430, L93

Resmi L., 2017, Journal of Astrophysics and Astronomy, 38, 56

Resmi L., Bhattacharya D., 2008, Monthly Notices of the Royal Astronomical Society, 388, 144

Rhodes L., et al., 2020, Monthly Notices of the Royal Astronomical Society, 496, 3326

Rickett B. J., 1986, The Astrophysical Journal, 307, 564

Rossi A., et al., 2014, Astronomy & Astrophysics, 572, A47

Rowlinson A., et al., 2019, Astronomy and Computing, 27, 111

Rowlinson A., et al., 2022, Monthly Notices of the Royal Astronomical Society, 517, 2894

Russell T. D., et al., 2019, The Astrophysical Journal, 883, 198

Sari R., Piran T., Narayan R., 1998, The Astrophysical Journal Letters, 497, L17

Sari R., Piran T., Halpern J. P., 1999, The Astrophysical Journal Letters, 519, L17

Sault R. J., Teuben P. J., Wright M. C. H., 1995, in Shaw R. A., Payne H. E., Hayes J. J. E., eds, Astronomical Society of the Pacific Conference Series Vol. 77, Astronomical Data Analysis Software and Systems IV. p. 433 (arXiv:astro-ph/0612759)

Selsing J., Fynbo J. P. U., Heintz K. E., Watson D., 2019, GRB Coordinates Network, 23695, 1

Seward F. D., Charles P. A., 2010, X-ray binaries, 2 edn. Cambridge University Press, p. 171–241, doi:10.1017/CBO9780511781513.012

Smith N., 2014, Annual Review of Astronomy & Astrophysics, 52, 487

Stanek K. Z., et al., 2003, The Astrophysical Journal Letters, 591, L17

Stark R. F., Connors P. A., 1977, Nature, 266, 429

Starling R. L. C., van der Horst A. J., Rol E., Wijers R. A. M. J., Kouveliotou C., Wiersema K., Curran P. A., Weltevrede P., 2008, The Astrophysical Journal, 672, 433

Stewart A. J., et al., 2016, Monthly Notices of the Royal Astronomical Society, 456, 2321

Stewart A. J., Muñoz-Darias T., Fender R. P., Pietka M., 2018, Monthly Notices of the Royal Astronomical Society, 479, 2481

Swinbank J. D., et al., 2015, Astronomy and Computing, 11, 25

Taylor G. B., Frail D. A., Berger E., Kulkarni S. R., 2004, The Astrophysical Journal Letters, 609, L1

Thyagarajan N., Helfand D. J., White R. L., Becker R. H., 2011, The Astrophysical Journal, 742, 49

Tingay S., et al., 2012, in Resolving The Sky - Radio Interferometry: Past, Present and Future. p. 36 (arXiv:1212.1327)

Tremou L., Heywood I., Vergani S. D., Woudt P. A., Fender R. P., Horesh A., Passmoor S., Goedhart S., 2019, GRB Coordinates Network, 23760, 1

Tremou E., et al., 2020, Monthly Notices of the Royal Astronomical Society, 493, L132

Varghese S. S., Obenberger K. S., Dowell J., Taylor G. B., 2019, The Astrophysical Journal, 874, 151

Wade C. M., Hjellming R. M., 1972, Nature, 235, 271

Walker M. A., 1998, Monthly Notices of the Royal Astronomical Society, 294, 307

Walker M. A., 2001, Monthly Notices of the Royal Astronomical Society, 321, 176

Wang X.-G., Zhang B., Liang E.-W., Lu R.-J., Lin D.-B., Li J., Li L., 2018, The Astrophysical Journal, 859, 160

Wang Z., et al., 2021, The Astrophysical Journal, 920, 45

Watts A. L., et al., 2016, Reviews of Modern Physics, 88, 021001

Wijers R. A. M. J., Galama T. J., 1999, The Astrophysical Journal, 523, 177

Woosley S. E., 1993, The Astrophysical Journal, 405, 273

Woosley S. E., Bloom J. S., 2006, Annual Review of Astronomy & Astrophysics, 44, 507

Wright E. L., 2006, Publications of the Astronomical Society of the Pacific, 118, 1711

Wright E. L., et al., 2010, The Astronomical Journal, 140, 1868

Zhang B., 2018, The Physics of Gamma-Ray Bursts, doi:10.1017/9781139226530.

de Ugarte Postigo A., et al., 2020, Astronomy & Astrophysics, 633, A68

van Paradijs J., et al., 1997, Nature, 386, 686

van der Horst A. J., 2007, PhD thesis, University of Amsterdam

van der Horst A. J., Rol E., Wijers R. A. M. J., Strom R., Kaper L., Kouveliotou C., 2005, The Astrophysical Journal, 634, 1166

van der Horst A. J., et al., 2014, Monthly Notices of the Royal Astronomical Society, 444, 3151